Centre for Clean Energy Technology & School of Chemistry

and Forensic Science

Faculty of Science

Graphene-based Nanocomposite Materials for High-performance Supercapacitors and Lithium Rechargeable Batteries

A Thesis Presented in Fulfillment of the Requirements for the

Degree of

Doctor of Philosophy

By

Bei Wang, B. Sc., M. Eng

University of Technology Sydney

2012

Certificate of Authorship/Originality

I certify that the work in this thesis has not previously been submitted for a degree nor has been submitted as part of requirements for a degree except as fully acknowledged within the text.

I also certify that the thesis has been written by me. Any help that I have received in my research work and the preparation of the thesis itself has been acknowledged. In addition, I certify that all information sources and literature used are indicated in the thesis.

Signature of Student

Production Note:
Signature removed prior to publication.

July 2012

Acknowledgement

First, I would like to express my sincere gratitude to my supervisor, Prof. Guoxiu Wang, who has been guiding and supporting me wholeheartedly through rigorous but fruitful supervision and financial funding for over five years since I started my research career in 2007. Dr. Jane Yao is also greatly acknowledged for all the administrative assistance and lab management, as well as figure processing and enhancement.

Special thanks are given to all my colleagues in the research team at the Centre for Clean Energy Technology for all the valuable discussions, kind co-operation and assistance. It is a pleasure to have worked with all of you and I really appreciate everyone's efforts in creating an intimate atmosphere for the research work.

I am also grateful for the assistance and patience of Rochelle Seneviratne, the Research and Development Officer, Faculty of Science, who always responds to my enquires and sorts out all the administrative issues. Relevant training in the research facilities from Dr. Ronald Shimmon, Dr. Linda Xiao, and all the MAU staff are much appreciated as well. Assoc. Prof. Alison Ung deserves real gratitude for her contribution to reviewing my manuscript and the priceless discussions. I would also like to acknowledge the editorial assistance from Dr. Fiona MacIver for proofreading this thesis.

Deep gratitude is to be expressed to my wife, my parents and my relatives, who have been caring and sustaining me over these years. Without your continuous support, I could not have finalized my PhD study and become a mature and responsible person. My upcoming baby fills me with joy. This thesis is also for you, my son. Thank you for bringing luck and happiness to me and to our family.

Table of Contents

List of Schemes, Tables and Figures

Schemes

Tables

Figures

Fig. 5-3 TEM images of the as-prepared Mn_3O_4/GNS nanocomposites: (a) a low magnification TEM image showing dense Mn_3O_4 nanoparticles deposited on a large area of graphene nanosheets and the SAED pattern (inset) displaying graphene (0 0 2) and Mn_3O_4 (1 0 3), (2 1 1), and (2 2 0) diffraction rings; (b) an HRTEM image illustrating the *d*-spacing of Mn_3O_4 nanoparticles, which were evaluated to be around 10 nm in size.

Fig. 5-4 AFM images of the as-prepared Mn_3O_4/GNS nanocomposites: (top) an image taken in a scan area of 500 nm by 500 nm, displaying graphene nanosheets (indicated by arrows) with embedded Mn_3O_4 nanoparticles (indicated by circles); (bottom) height profile across the examined area, as indicated by the red line, from which the particle size was determined to be 9.7 nm and 12.6 nm for particles (a) and (b), respectively.

Fig. 5-5 CV curves of dried graphene nanosheets at a 5 mV s^{-1} scan rate in (a) 1 M Na_2SO_4 and (b) 6 M KOH, and CV curves of Mn_3O_4/GNS nanocomposite powders at scan rates of 5 mV s^{-1}, 10 mV s^{-1}, 20 mV s^{-1}, and 50 mV s^{-1} in (c) 1 M Na_2SO_4 and (d) 6 M KOH.

Fig. 6-1 (a) XRD pattern and (b) Raman spectrum of the as-prepared Co_3O_4/GNS nanocomposite material.

Fig. 6-2 (a) XRD and (b) Raman spectrum of pure graphene nanosheets.

Fig. 6-3 FE-SEM images of the Co_3O_4/GNS nanocomposite obtained under GB-HR mode: (a) numerous curly graphene nanosheets observed at a low magnification, and (b) a higher magnification image, displaying the distribution of Co_3O_4 nanoparticles on graphene nanosheets. The embedded Co_3O_4 nanoparticles are ~20 nm in size.

Fig. 9-10 Cycling performances of CoS_2/GNS, GNS and CoS_2 nanoparticles at 0.5 A g^{-1} and 1 A g^{-1}, respectively in 1 M $LiClO_4$ in PC for 1500 cycles.

Abstract

Human activity and energy supplies mainly rely on the consumption of non-regenerative fossil fuels. With the gradual decrease of these carbon-based energy sources and the increase in environmental pollution, finding alternative green and sustainable energies has become critical. Therefore, innovative and renewable energy technologies must be developed to combat global warming and climate change.[1, 2] Extensive research has been performed on the development of solar cells,[3, 4] fuel cells,[5] lithium-ion batteries[6, 7] and supercapacitors[8, 9] to replace carbon-based energy.

Graphene has been considered a promising electrode material for energy storage applications due to its ultrahigh surface area (2600 m^2 g^{-1}),[10] excellent electric conductivity,[11] and one-atom thick two-dimensional sp^2 carbon arrangement.[12] However, the surface area of graphene nanosheets (GNS) is often dramatically reduced because monolayer GNS always stack to multilayer in the dry state. The stacking of GNS leads to unexposed surface area, which hinders the ion diffusion from the electrolyte to the electrode, resulting in a low electrochemical performance.

To prevent the re-stacking of GNS, and thus maintain well-exposed surface area, nanocrystals can be inserted between graphene layers to form nanocomposite materials. With the above motivation, graphene-based nanocomposite materials have been intensively studied in this thesis. All the materials examined were prepared via different synthesis techniques and well characterized. Their electrochemical properties were evaluated for supercapacitors and/or lithium rechargeable batteries. Sn/GNS is shown to have a very high reversible specific capacity of 785 mAh g^{-1}. Mn_3O_4/GNS shows a specific capacitance of 256 F g^{-1}, almost double that of pure GNS. Of the examined

materials, Co_3O_4/GNS presents the highest supercapacitance of 478 F g^{-1} and a rechargeable specific capacity of 722 mAh g^{-1}. S/GNS generates ultra-high specific capacity of up to 1580 mAh g^{-1} and excellent rate capability. SnO_2 nanoparticles supported by GNS deliver a specific capacity of 830 mAh g^{-1} with well maintained cycling stability. CoS_2/GNS yields high capacitances of 314 F g^{-1} in an aqueous electrolyte and 141 F g^{-1} in an organic electrolyte. The enhanced overall electrochemical performances of these nanocomposite materials can be attributed to the dual contributions of the decorating materials, creating enlarged interlayer spacing, and graphene itself, with its facility for flexible nanolayered structure. The results of this study of these graphene-based nanocomposite materials indicate their great potential for application to practical energy storage devices.

Chapter One

Introduction

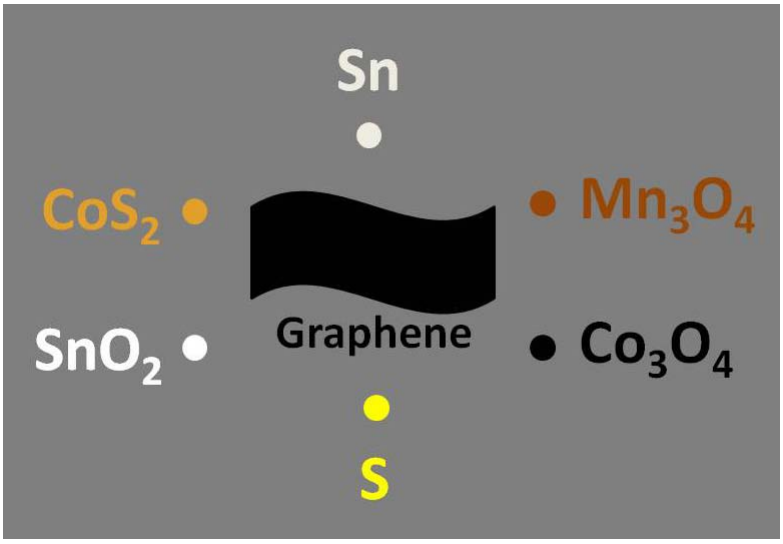

Chapter 1 — Introduction

Supercapacitors and lithium rechargeable batteries are typical energy sources that can store renewable energy with increased energy density and power density over regular capacitors and batteries. It is believed they will contribute to altering current fuel-consumption patterns and serve in the realization of electric vehicles or hybrid electric vehicles.[13] The development of these energy systems so that they have improved electric performance and are commercially viable, requires highly electrochemically active electrode materials that are low cost and environment friendly.

Graphene and its related materials offer lots of superior properties in materials science and are considered to meet all the critical requirements for a practical electrode material due to their unique 2D nanostructure. Therefore, worldwide research has been invested in the modification, decoration and doping of 2D carbon-ringed graphene nanosheets to further enhance the electrochemical performance of the electrode materials. In the work reported here, a few graphene-based nanocomposites have been systematically studied. The synthetic methods, along with the characterizations and the electrochemical properties in supercapacitors and lithium rechargeable batteries are detailed in each chapter.

Chapter 2 explores the history and development of graphene, deals with the synthetic methods for graphene and the general properties of graphene. The applications of graphene and graphene-based materials in energy storage devices are intensively reviewed and the fundamentals of supercapacitors and lithium-ion batteries are also discussed.

Chapter 3 introduces experimental specifications that are related to the entire project. Various materials preparation methods are firstly introduced, followed by the physical characterization techniques, including X-ray diffractometry, Scanning Electron Microscopy, Transmission Electron Microscopy, Atomic Force Microscopy, Raman Spectroscopy, and Thermogravimetric Analysis. Electrode preparation, cell assembly and electrochemical testing techniques are also detailed.

In Chapter 4, a general strategy is demonstrated for achieving optimum electrochemical performance by constructing a 3D nanocomposite architecture with the combination of nanosized Sn particles and GNS. The Sn nanoparticles act as spacers to effectively separate GNS. FE-SEM and TEM analysis revealed the homogeneous distribution of Sn nanoparticles (2–5 nm) in a graphene nanosheet matrix. CV measurement is used to prove the highly reversible nature of the reaction between Li^+ and the Sn/GNS nanocomposite. The 3D nanoarchitecture gives the Sn/GNS nanocomposite electrode an enhanced electrochemical performance. As discussed in Chapter 4, this strategy can be extended to prepare other anode and cathode materials for advanced energy storage and conversion devices.

Chapter 5 deals with Mn_3O_4/GNS nanocomposites synthesized by mixing a graphene suspension in ethylene glycol with MnO_2 organosol, followed by subsequent ultrasonication processing and heat treatment. The as-prepared product consists of nanosized Mn_3O_4 particles homogeneously distributed on graphene nanosheets, which has been confirmed by FE-SEM and TEM analysis. AFM analysis further identified the distribution of dense Mn_3O_4 nanoparticles on graphene nanosheets. When used as electrode materials in supercapacitors, Mn_3O_4/GNS nanocomposites exhibited a high specific capacitance of 175 F g^{-1} in 1 M Na_2SO_4 electrolyte and 256 F g^{-1} in 6 M KOH

electrolyte, respectively. As discussed in Chapter 5, the enhanced supercapacitance of Mn_3O_4/GNS nanocomposites could be ascribed to electrochemical contributions of Mn_3O_4 nanoparticles, functional groups attached to graphene nanosheets, and significantly increased specific surface area.

Chapter 6 focuses on Co_3O_4/GNS nanocomposite material, prepared by an in-situ solution-based method under reflux conditions. In the reaction progress, Co^{2+} salts were converted to Co_3O_4 nanoparticles that were simultaneously inserted into the graphene layers upon the reduction of graphite oxide to graphene. The prepared material consists of uniform Co_3O_4 nanoparticles (15–25 nm), which are well dispersed on the surfaces of graphene nanosheets. This has been confirmed through observations by FE-SEM, TEM and AFM. The prepared composite material exhibits an initial reversible lithium storage capacity of 722 mAh g^{-1} in lithium-ion cells and a specific supercapacitance of 478 F g^{-1} in 2 M KOH electrolyte for supercapacitors. These values were higher than those previously reported for pure graphene nanosheets and Co_3O_4 nanoparticles. Co_3O_4/GNS nanocomposite material demonstrated an excellent electrochemical performance as an anode material for reversible lithium storage in lithium ion cells and as an electrode material in supercapacitors.

Chapter 7 presents S/GNS nanocomposite material, which has been prepared by incorporating sulfur into the graphene frameworks through a melting process. FE-SEM analysis shows a homogeneous distribution of sulfur in the graphene nanosheet matrix. The S/GNS nanocomposite exhibits a super-high lithium-storage capacity of 1580 mAh g^{-1} and a satisfactory cycling performance in lithium-sulfur cells. The enhancement of the reversible capacity and cycle life could be attributed to the flexible graphene nanosheet matrix, which acts as a conducting medium and a physical buffer to cushion

the volume change of sulfur during the lithiation and delithiation process. As discussed in Chapter 7, graphene-based nanocomposites can significantly improve the electrochemical performance of lithium-sulfur batteries.

Chapter 8 reports SnO_2 nanoparticles dispersed on graphene nanosheets through a solvothermal approach using ethylene glycol as the solvent. The uniform distribution of SnO_2 nanoparticles on graphene nanosheets has been confirmed by FE-SEM and TEM. The particle size of SnO_2 was determined to be around 5 nm. The as-synthesized SnO_2/GNS nanocomposite exhibited an enhanced electrochemical performance in lithium-ion batteries, compared with bare graphene nanosheets and bare SnO_2 nanoparticles. The SnO_2/GNS nanocomposite electrode delivered a reversible lithium storage capacity of 830 mAh g^{-1} and a stable cyclability up to 100 cycles. As discussed in Chapter 8, the excellent electrochemical properties of this graphene-supported nanocomposite could be attributed to the insertion of nanoparticles between graphene nanolayers and the optimized distribution of nanoparticles on graphene nanosheets.

In Chapter 9, CoS_2/GNS nanocomposite prepared by a facile solvothermal method is described. FE-SEM and TEM analysis has confirmed that CoS_2 nanoparticles with sizes of 5–15 nm are densely anchored on graphene nanosheets. The as-prepared nanocomposite was electrochemically tested as an electrode material for supercapacitors. The CoS_2/GNS nanocomposite exhibited specific capacitances of 314 F g^{-1} in the aqueous electrolyte and 141 F g^{-1} in the organic electrolyte at a current rate of 0.5 A g^{-1} with excellent cycling stabilities. As discussed in Chapter 9, the electrochemical performance of the nanocomposite is a significant improvement over that of bare graphene nanosheets and CoS_2 nanoparticles. This could be credited to the 3D nanoarchitecture, in which CoS_2 nanoparticles were sandwiched between graphene

nanosheets, and the additional electrochemical contribution of the decorating CoS_2 nanoparticles.

A general summary is given in Chapter 10, containing an overview of the examinations of the selected nanocomposite materials in this thesis and an outlook to future development of graphene-related research in the energy field.

Chapter Two

Literature Review

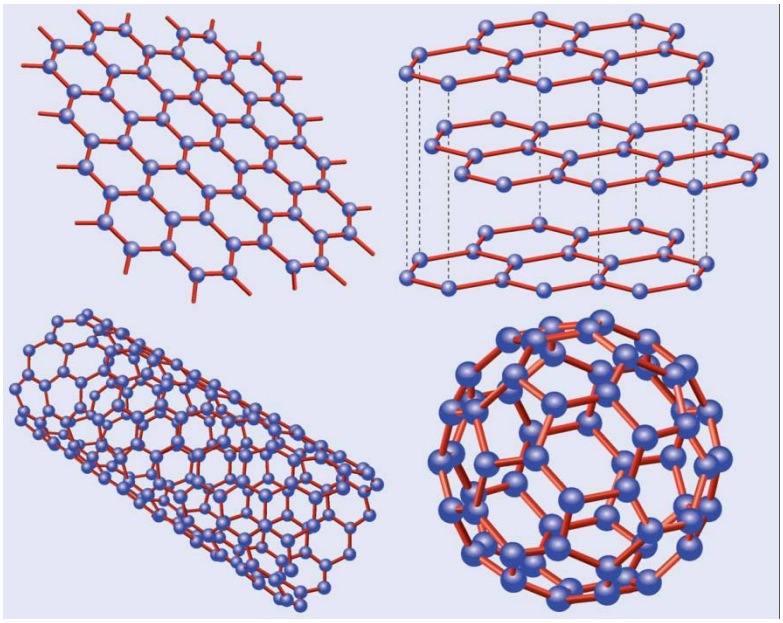

Chapter 2 — Literature Review

The Nobel Prize in Physics 2010 was awarded jointly to Andre Geim and Konstantin Novoselov *"for groundbreaking experiments regarding the two-dimensional material graphene"*. Graphene has drawn a broad spectrum of interests worldwide, since the first graphene material was extracted from graphite via a micromechanical cleavage method by Andre Geim, Konstantin Novoselov and their co-workers in 2004.[14] This chapter reviews the brief history and development of graphene, deals with its general properties and synthesis methods, and provides a few examples of graphene and graphene-based nanocomposite applications to energy storage devices, especially supercapacitors and lithium-ion batteries. The fundamentals of supercapacitors and lithium-ion batteries are also presented in detail.

2.1 History and Development of Graphene

Graphene is the name given to a single layer of carbon atoms in a closely packed honeycomb two-dimensional (2D) lattice, which is a basic building block for all other graphitic materials of various dimensionalities. **Scheme 2-1** shows schematic sketches of mother graphene and the other carbon allotropes.[15] Graphene, as shown on the top left, consists of a 2D hexagonal lattice of highly ordered carbon atoms. The carbon atoms are covalently bonded to three others, leaving one valence electron unoccupied. The vacancy of the free electron makes graphene conduct electricity. Other forms of carbon allotropes all derive from graphene: graphite which can be considered as a stack of graphene layers (top right); carbon nanotubes, which are rolled sheets of graphene

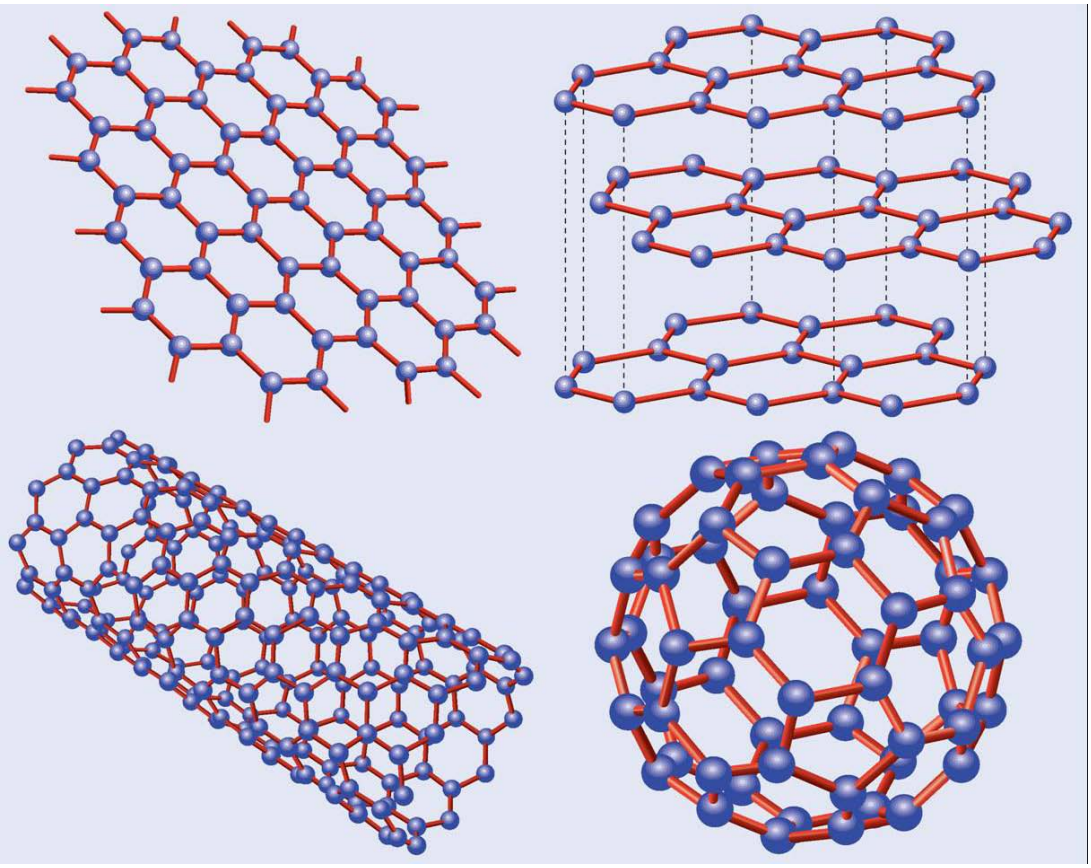

Scheme 2-1 Graphene and other carbon allotropes: graphene (top left), graphite (top right), carbon nanotube (bottom left), buckminsterfullerene (C_{60}, bottom right).[15]

(bottom left); and buckminsterfullerene (C_{60}), which consists of graphene balled into a sphere through introduction of some pentagons and haxagons into the lattice (bottom right). Since the discovery of this carbon building block by K.S. Novoselov and A.K. Geim in 2004,[14] graphene has attracted numerous investigations into its unique physical, chemical, and mechanical properties, and a new research area for materials science and condensed-matter physics has opened up, aiming for wide-ranging and diverse technological applications of graphitic materials.[16-20] Owing to the high quality of the sp^2 conjugated bond in the carbon lattice, electrons were found to move ballistically in a graphene layer without scattering with mobility exceeding 15000 $m^2 V^{-1} s^{-1}$ at ambient temperature. Furthermore, the charge carriers in graphene

crystals mimic relativistic particles with zero rest mass, and these particles were described as massless Dirac fermions.[16, 21] These characteristics drive the dreams of developing graphene based electronics. Although this has not yet been realized, there are real possibilities for a bright future.

2.2 Preparation of Graphene

"Graphene is a rapidly rising star on the horizon of materials science and condensed-matter physics." As A.K. Geim and K.S. Novoselov stated in their famous review article – The Rise of Graphene.[12] Graphene has shown great potential in various applications and therefore the preparation of high-quality 2D graphene crystals is the first and most crucial step, not only for fundamental research but also for device applications.

The preparation of monolayer graphite can be dated back to as early as 1975, when mono- and multi-layered graphite were produced by B. Lang et al. via a thermal decomposition approach on single crystal platinum substrates.[22] Decades later, H. Shioyama, reported the cleavage of graphite to graphene in 2001.[23] However, the discovery by K.S. Novoselov et al. in 2004 was recognized as the first to show reproducible graphene product and lead to further development of new synthesis routes for graphene nanosheets.[14] The major synthesis routes of graphene are categorized and briefly reviewed below.

2.2.1 Exfoliation and Cleavage

As per K.S. Novoselov et al.'s report,[14] 5 μm deep mesas (of area 0.4 to 4 mm^2) were

made initially by dry etching highly oriented pyrolytic graphite (HOPG) sheets (1 mm thick) in oxygen plasma. The mesas were then stuck to a photoresist under baking conditions. Subsequently, scotch tape was used to peel off layers from the graphite sheet. Thin flakes fell off the photoresist and transferred to a silicone substrate. These flakes were then identified to be single- to few-layer graphene sheets. Obtaining graphene using this process was found to be very reliable and easy. Later, further investigations involving some modifications of the original exfoliation were undertaken to optimize the quality of graphene. The graphene flakes obtained under controlled exfoliation were few-to-single graphene atomic layers, with remarkable large and flat layers and very few folds and pleats.[24] Then, large area (mm sized), few-layer graphene was achieved by exfoliating graphite from borosilicate glass (or potentially any insulating substrate).[25] New exfoliation approaches in liquid phase were also performed, such as in hydrazine hydrate,[26, 27] *N*-methyl-2-pyrrolidone,[28] and sodium dodecylbenzene sulfonate.[29]

2.2.2 Chemical Method

Micromechanical cleavage of bulk graphite can only produce graphene flakes in limited quantities. Furthermore, the entire process is hard to control. In response to the above problems of micromechanical cleavage, ultrathin epitaxial graphene was grown on single-crystal silicon carbide by vacuum graphitization. This approach allows the fabrication of a patterned graphene structure, which is desirable for electronic applications.[30-32] Recently, polystyrene-graphene based composite materials have demonstrated extraordinary room temperature electrical conductivity, leading to the development of a new class of composite materials with enhanced properties and

functionalities.[10] Graphene oxide papers exhibit high mechanical stiffness and strength, resulting from a unique interlocking-tile arrangement of the nanosized graphene oxide sheets.[33] Therefore, graphene has great potential to be massively used as an engineering material with the demand exceeding one million tons annually.[34] Micromechanical cleavage and ultrahigh vacuum graphization certainly cannot meet such a high demand in the future.

A soft chemical synthesis route for production of large-sized graphene nanoplatelets can lead to high-quality graphene nanosheets.[35] In a typical synthesis process, natural graphite powders were oxidized to graphite oxide using a modified Hummers method.[36] One gram graphite powder and 0.5 g $NaNO_3$ were poured into 70 ml concentrated H_2SO_4 (under an ice bath). Then 3 g $KMnO_4$ was gradually added. The mixture was stirred for 2 h and then diluted with de-ionized (DI) water. After that, 5% H_2O_2 was added into the solution until the color of the mixture changed to brilliant yellow. The as-obtained graphite oxide was re-dispersed in DI water and then exfoliated to generate graphene oxide nanosheets (GONS) by ultrasonication using a Brandson Digital Sonifier (S450D, 40% amplitude). The brown graphene oxide nanosheet dispersion was poured into a round-bottomed flask, to which hydrazine monohydrate (as reducing agent) was added. The mixed solution was then refluxed at 100 °C for 2 h, over which time the colour of the solution gradually changed to dark black as the graphene nanosheet dispersion was formed. The dispersion was further centrifuged for 15 min at 3000 rpm to remove a small amount of precipitate. The supernatant of the graphene nanosheet dispersion was directly dried in a vacuum oven to obtain the bulk of the graphene nanosheet powder.

2.2.3 Electrolytic Exfoliation

Highly efficient synthesis of graphene by electrolytic exfoliation from graphite has been reported,[37] which can be easily scaled up for large-scale production. The as-prepared graphene nanosheets are stable in aqueous solution, ready to be isolated as monolayer or multilayer graphene sheets. The capability to produce graphene in large quantity paves the way for versatile practical applications of graphene.

High purity graphite rods (6 mm, 99.999%) were used as electrodes. Poly(sodium-4-styrenesulfonate) (PSS, Mw = 70000) was dissolved in DI water to form the electrolyte (0.001 M). In a typical synthesis, two graphite rods were placed in an electrolysis cell filled with the electrolyte. A constant potential of 5 V (DC voltage) was applied to the two electrodes (CHI660C, Electrochemical Workstation). After 20 min electrolysis, black product gradually appeared at the positive electrode (anode). The exfoliation continued for 4 h. Then the product (a dispersion) was taken from the electrolysis cell. The dispersion was centrifuged at low speed (1000 rpm) to remove large agglomerates. The top of the dispersion was then decanted. This graphene–PSS suspension is very stable. After 6 months storage, there is no precipitation. To obtain dry graphene powders, the dispersion was washed with DI water and ethanol, and then dried in a vacuum oven at 80 °C. The yield of graphene was estimated by weighting the dried graphene powders and the dried sediment. The electrolytic exfoliation method results in graphene being produced at a yield of about 15 wt%. Graphene paper was also made by vacuum filtration through an anodized aluminum oxide (AAO) membrane (47 mm, 200 nm pore size).

2.2.4 Other Methods

So far, many methods have been developed to produce graphene. These include chemical vapor deposition (CVD) growth of graphene either on nickel layers, with graphene nanaosheets being prepared with quite low sheet resistance and 80% optical transparency,[38] or, substrate-free by passing liquid ethanol droplets into a microwave plasma reactor.[39] A solvothermal synthesis combined with pyrolysis has also been proposed to synthesize gram-scaled fused arrays of graphene nanosheets by mild sonication with common reagents of ethanol and sodium.[40]

2.3 Graphene and Graphene-based Materials for Energy Storage Applications

As discussed earlier, graphene nanosheets have very promising electronic properties and the developed synthesis methods have made utilization of graphene viable. So far, the use of graphene has covered a broad range of areas. Examples are given as follows. Graphene has been used to detect step-like changes in resistance when a gas molecule attaches to or detaches from graphene's surface, due to the fact that graphene is an exceptionally low-noise material electronically.[20] A major contribution of quantum confinement could be made for electron transport in quantum dot devices carved entirely from graphene, especially for quantum dots smaller than 100 nm.[41] It might be possible to explore graphene field-effect transistors with shorter channel lengths and higher speeds to avoid the adverse short-channel effects, which restrict the performance of existing devices.[42] Nano-graphene oxide has been used for live cell imaging and loading doxorubicin, a widely used cancer drug, with antibody for selective killing of

cancer cells in vitro.[43] Moreover, graphene has attracted worldwide attention for energy storage and conversion. Its potential applications in supercapacitors,[44] lithium-ion batteries,[35] lithium-sulfur batteries,[45, 46] and the latest developed lithium-air batteries,[47, 48] have also been intensively investigated.

However, graphene produced from chemical methods are often stacked to multiple layers in the dry state and form irreversible precipitate agglomerates. This will result in almost no difference in the electrochemical behaviour compared to bulk graphite platelets, as the compressed graphene nanosheets have very low surface area. So the major challenge remains to create graphene with ultrahigh surface area, which advances the practical electronic applications, by minimizing the stack degree of graphene nanosheets or ideally preventing the stack when graphene is in the dry state. This can be achieved by inserting spacer materials between graphene nanosheets. **Scheme 2-2** shows a schematic illustration of nanoparticles functioning as spacers to prevent the stacking of graphene.[49]

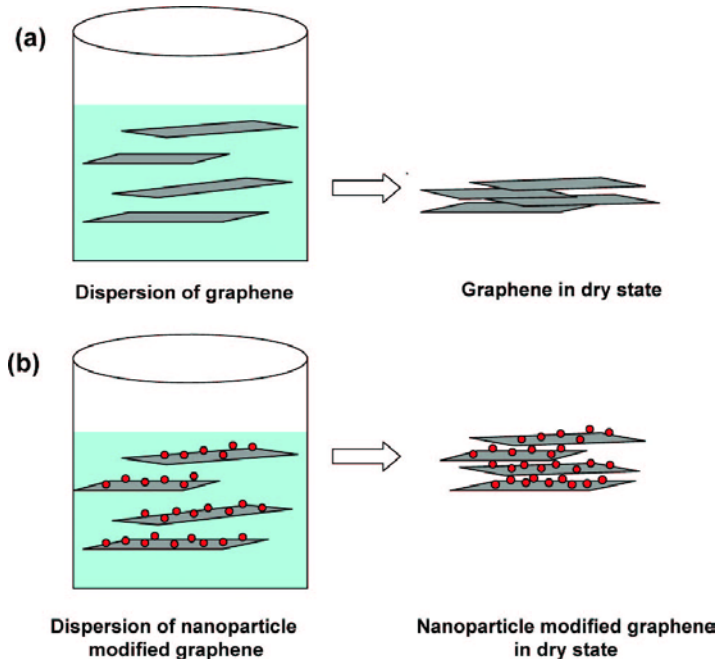

Scheme 2-2 Schematic illustrations of (a) dried graphene and (b) graphene with modified nanoparticles.[49]

Generally, the spacers could be any nanosized materials to separate graphene nanosheets and make both sides of the nanosheets accessible. However, considering the routes to introduce nanomaterials to the interlayers of graphene and the specific electronic applications, highly electrochemical active embedded nanomaterials are preferred. In fact, graphene can also be considered as conductive and buffer matrix to improve the performance of the electrochemically active materials. Therefore, this thesis focuses on investigating electrochemically active materials for decorating graphene nanosheets to enhance the overall electrochemical performance of the nanocomposite materials.

In the following sections, the fundamentals of supercapacitor and lithium-ion batteries as energy storage devices are reviewed individually and the related electrode materials, including graphene and graphene-based nanocomposites, are briefly introduced for an overview of the up-to-date development of graphene-based nanocomposites.

2.3.1 Supercapacitors

2.3.1.1 History and Development

Supercapacitors are also known as ultracapacitors, electrochemical capacitors or hybrid capacitors, and are a type of capacitor with higher energy densities (5 Wh kg^{-1}) than the conventional capacitors. Unlike common capacitors, supercapacitors consist of special electrodes and a designated electrolyte to store energy in a very small package by ion adsorption (electrochemical double layer capacitance) or fast surface redox reactions (pseudocapacitance). Although supercapacitors have lower energy densities compared to popular lithium-ion batteries, they are capable of ultrafast charge/discharge processes

and therefore lead to quite high power densities (10 kW kg^{-1}).[50] As a consequence, they can be used as backup energy sources and to replace or combine with batteries for specific energy applications.

Supercapacitors were first brought into public view in 1957 when General Electric found out that this kind of capacitor could restore quite high capacitance by a double layer mechanism based on high surface area carbon and this discovery was filed as a patent by Becker.[51] Later in 1966, Stand Oil Company, Cleveland (SOIHO) invented the first supercapacitor device which stored energy at the double layer interface.[52] Five years later, in 1971, NEC (Japan) developed the first supercapacitor device with an aqueous-electrolyte capacitor under SOIHO's license,[8] a device which is considered to be the first commercialized supercapacitor product. A recent example of a reported use of supercapacitors was in the emergency doors on an Airbus A380, proving the supercapacitor's reliability and high performance for large-scale applications.[53] The US Department of Energy assigns equal importance to both supercapacitors and batteries, which again emphasizes the important role of supercapacitors for practical implementations of future energy storage systems.[54] Scientific research into supercapacitors has been carried out since the 1990s and much improvement has been obtained so far.

2.3.1.2 Energy Storage Mechanism

Double Layer Capacitance

The energy storage mechanisms of supercapacitors can be grouped to two categories. One is called electrochemical double layer mechanism. The other is known as pseudocapacitive behaviour. The electrochemical double layer capacitors (EDLCs) store

energy by reversible ion adsorption from the electrolyte onto the active materials of the electrodes with electrochemical stabilities and high specific surface area (SSA). The model of energy storage could be defined by the following equation:

$$E = \frac{1}{2} CV^2 \quad \textbf{(Eq. 2-1)}$$

where E presents the entire energy delivered, C is the specific capacitance, and V is the potential window. The specific capacitance obtained with aqueous alkaline or acid electrolytes is often larger than in organic electrolytes. However, organic electrolytes can sustain a larger operating voltage range (1–3 V), and thus provide higher energy according to the above equation.

Based on the charge storage mechanism, there are no faradic reactions involved in EDLCs. Only the electrostatic surface charge plays an important role in storing the energy. This mechanism allows fast energy uptake and delivery to achieve a better power performance. Unlike the electrodes used in lithium-ion batteries, the supercapacitor electrodes can theoretically survive millions of cycles compared to a few thousand cycles for batteries. This is due to the electrostatic charge storage mechanism eliminating volume expansion associated with charge/discharge processes in batteries, and leading to a more durable service life. One the other hand, the electrolyte used in EDLCs is not involved in the charge storage, offering a wide range of options for the selection of compatible electrolytes with high power performances. However, charge storage arising from ion desorption will limit the energy density and current research mainly focuses on improving the energy performance. The materials suitable for EDLCs are required to be highly conductive and have large SSA. Various forms of carbon, e.g. activated carbon, carbon nanotubes, and nanofibres, are considered to be best for

EDLCs. Their electrochemical properties will be reviewed intensively in the following sections of this chapter.

Pseudocapacitance

Supercapacitors defined as having pseudocapacitive behaviour differ from the electrochemical double layer mechanism supercapacitors because they take advantage of redox reactions at the surface of electrode materials to accumulate specific capacitance. This is similar to how a battery behaves. Pseudocapacitive behaviour of supercapacitors is caused by oxidation state changes of the metal cations during the intimate interactions of ions in the electrolyte with the surface of the active material particles.[53] Ruthenium oxide, RuO_2, has been the focus of research attention for the past few decades as it has three distinct oxidation states below 1.2 V and provides very high specific capacitance in acidic solutions.[50] However, the high cost and low potential window render RuO_2 useless in practical terms. Many less expensive transition metal oxides, e.g. MnO_2, Co_3O_4, Fe_2O_3 and NiO, have been investigated as replacements for RuO_2 but they never reach as high specific capacitance as RuO_2 does. Metal hydroxides[55, 56] nitrides[57, 58] and sulfides[59-62] are also pseudocapacitive materials, which deliver pseudocapacitance by surface redox reactions. Conducting polymers have also been tested as supercapacitor electrode materials with pseudocapacitive behaviours, and they store charge by bulk processes through doping and undoping. Electrodes with pseudocapacitance are less dependent on the surface area and often deliver higher specific capacitance than regular carbon-based materials using double layer charge storage mechanism. Although surface reactions offer higher

capacitance and better electrochemical performance, they also cause failure of electrode stability during cycling.

2.3.1.3 Electrode Materials

Based on the electric storage mechanisms and the nature of the electrode materials, there are three main categories of electro-active materials used in research to fabricate supercapacitor electrodes. They are: (i) carbon-based materials; (ii) metal oxides/hydroxides/nitrides/sulfides, and (iii) conducting polymers.

Carbon-based Materials

Carbon materials are cheap, light and abundant in nature. They are also sufficiently electrochemically stable to be EDLC electrodes. Activated carbon materials have been reported as derived from natural carbon-rich organic precursors (coconut shells, wood, pitch or coal) or synthetic polymers. These precursors were heat treated in an inert atmosphere under selected conditions to introduce high surface area and pore volume.[53] The generated double layer capacitance could reach 100–120 F g^{-1} in organic electrolytes, and increase to 150–300 F g^{-1} in aqueous electrolyte at a lower cell voltage because of the limitation by water decomposition. However, there was no linear relationship between the specific surface area and the capacitance.[63-65] Some studies showed that pores smaller than 0.5 nm were not accessible to hydrated ions. The solvated ions present when an organic electrolyte is used are larger than 1 nm and are unable to access pores smaller than 1 nm. Thus, a pore size distribution of 2–5 nm was identified to be able to improve energy density and power capability.[53] However, only

moderate improvement on capacitance has been achieved with specific capacitance of 100–120 F g^{-1} in organic electrolyte and 150–200 F g^{-1} in aqueous electrolyte.[66, 67]

The developed theory of pore size and volume on activated carbons led to interest in application of templated mesoporous carbon, with pore size in the range of 2–50 nm according to the International Union of Pure and Applied Chemistry (IUPAC), to EDLC electrodes and to provide full access to the adsorbed ions.[68, 69] Three types of pores: micropores, structural mesopores and complementary mesopores were tailored in template mesoporous carbons with very high SSA of up to 1730 m^2 g^{-1}. Specific capacitances of 200 F g^{-1} for low current density (1 mA cm^{-2}) and 110 F g^{-1} for high current density (150 mA cm^{-2}) could be found and an energy density of 3 Wh kg^{-1} at a power density of 300 W kg^{-1} was achieved. Highly self-ordered mesoporous carbons (CMK-3) prepared from hexagonal self-ordered mesoporous SiO_2 (SBA-15) have also been explored for supercapacitor applications and the exhibited double-layer capacitance was 60–90 F g^{-1} at low current rates.[70] The electrochemical performance was further enhanced by CO_2 activation to increase the SSA and volume of both mesopores and micropores, and the obtained specific capacitance reached up to 223 F g^{-1} in 6 M KOH electrolyte, due to a very high SSA of 2749 m^2 g^{-1}, a large pore volume of 2.09 cm^3 g^{-1} and well-balanced micro/mesoporosity.[71]

Metal Oxides/Hydroxides/Nitrides/Sulfides

RuO_2 is a well studied material and its charge storage can be described as fast reversible electron transfer combined with an electro-adsorption of protons on the surface of RuO_2 particles, according to the following equation (where $0 \leq x \leq 2$). The specific capacitance of amorphous RuO_2 can reach up to 720 F g^{-1}.[72]

$$RuO_2 + xH^+ + xe^- \leftrightarrow RuO_{2-x}(OH)_2 \quad (\textbf{Eq. 2-2}\ [53])$$

Other transition metal oxide materials, including MnO_2, Co_3O_4, NiO, etc., attract great attention in regard to their preparation and electrochemical performance for supercapacitors. For example, various nanostructured MnO_2 materials yielded specific capacitances ranging from 72–168 F g^{-1} in 1 M Na_2SO_4 solution.[73] Mesoporous Co_3O_4 nanostructure with tunable morphology achieved a specific capacitance of 85 F g^{-1} at a high current density of 20 mA cm^{-2} and maintained a good cycling retention of 93% in 3 M KOH.[74] Hierarchical porous NiO with superstructures was capable of delivering a very high specific capacitance of 710 F g^{-1} at 1 A g^{-1} and also maintained ~98% of its capacitance for 2000 cycles, showing great potential to replace RuO_2 as the electrode material for supercapacitors.[75]

On the other hand, nanolayered α-$Co(OH)_2$ was reported to achieve a specific capacitance of 860 F g^{-1} for a 0.8 mg cm^{-2} deposition on a stainless steel substrate in 1 M KOH electrolyte.[55] VN nanocrystals were able to maintain a high specific capacitance of ~400 F g^{-1} at a scan rate of 50 mV s^{-1} for up to 1000 cycles, due to the fast and reversible surface redox reactions.[57] CoS nanowires, prepared via a hydrothermal process, yielded a competitive capacitance of 508 F g^{-1}.[60] The employment of hydroxides, nitrides and sulfides as electrode materials broadens the scope of the development of high-performance supercapacitors.

Conducting Polymers

Polyaniline, polypyrrole, polythiophene and their derivatives are typical electrode materials among many kinds of conducting polymers for supercapacitors.[76-78] A

polyaniline based supercapacitor was reported, which reached a specific capacitance of 150 F g^{-1}. The energy density and power density of the device were 5 Wh kg^{-1} and 1200 W kg^{-1}, respectively.[79] Polypyrrole electrodes were also investigated, exhibiting a very high specific capacitance of 480±50 F g^{-1} in 1 M KCl with a very stable cycle life. The excellent performance was due to the highly porous nanostructure.[80] The only drawback with the conducting polymer electrodes is their poor cycling stability, reducing the initial electrode performance.[8] Therefore, recent research on conducting polymers is directed towards hybrid supercapacitor systems following doping with metal oxides or other carbon materials for enhanced electrochemical performances.

Graphene and Graphene-based Materials

Technically, graphene is one of the carbon based materials with high SSA to deliver double layer capacitance. The unique 2D sp^2 carbon arrangement makes graphene nanosheets accessible by active ions on both sides and also leads to the possibility of further modification on the vacancy sites to maintain a well exposed surface area for electric storage. Chemically-modified graphene was firstly reported in 2008 with surface functionalities, yielding specific capacitances of 135 F g^{-1} and 99 F g^{-1} in aqueous and organic electrolytes, respectively.[44] Graphene synthesized by hydrazine reduction also maintained well-separated graphene nanosheets, with a maximum specific capacitance of 205 F g^{-1}.[81] Later, graphene nanosheets with mesopores were prepared to achieve a stable specific capacitance of 150 F g^{-1} for 500 cycles.[82] Morphology controlled graphene nanosheets have also been obtained with a curved single layer and mesopores.[83] This graphene-base supercapacitor achieved an ultrahigh energy density. The latest breakthrough is the successful synthesis of

chemically activated graphene nanosheets, which had a specific surface area of 3100 $m^2 g^{-1}$ and delivered a specific capacitance of 166 F g^{-1} at various current rates in an organic electrolyte.[84] Recently, nitrogen doped graphene has also been introduced for high-performance supercapacitors.[85] All these modifications indeed improve the electrochemical properties of graphene.

Another effective technique for preparing graphene-based supercapacitors is to prevent the re-stacking of graphene nanosheets by inserting nanocrystals between graphene layers to form composite materials. Many graphene-based nanocomposites have been reported, including decorations with $Ni(OH)_2$ nanoplates,[86] $Co(OH)_2$,[87] RuO_2,[88] SnO_2,[89] Co_3O_4,[90] and various MnO_2 nanostructures.[91-98] All of these graphene-based nanocomposite materials yielded significantly enhanced specific capacitance over the modified graphene materials as presented above by taking advantage of the high specific surface area of graphene and the extra electrochemical contributions from the embedded nanosized materials.

2.3.2 Lithium-Ion Batteries

2.3.2.1 History and Development

Lithium-ion batteries are a family of rechargeable batteries in which lithium ions move from anode to cathode on discharging and also reversibly diffuse from cathode to anode on charging. Unlike primary lithium batteries, where a lithium metal is used, lithium-ion batteries are made of lithium intercalated materials as the electrodes. As a dominant power source, lithium-ion batteries are widely used to support portable electronic

devices, such as mobile phones, laptops, digital cameras, etc, and are believed to be a green choice to combat global warming and reduce the emission of CO_2 globally.

The first lithium-ion battery was commercialized by SONY and Asahi Kasei in 1991, and, after a few decades' research, this renewable energy device has been well developed. The first-generation lithium-ion batteries used electro-active powders as electrode materials, which were in the micrometre size. As lithium ions have an intrinsic diffusivity of 10^{-8} cm^2 s^{-1} in the solid state, the intercalation and deintercalation is quite limited, affecting charge/discharge rates and resulting in a low power density.[99] Nanosized electrode materials are believed to significantly impact the performance of a lithium battery because they offer reduced dimensions and shorter lithium diffusion paths for intercalation/deintercalation towards a high power density. Additionally, nanomaterials allow reactions to take place that cannot occur at the micrometre scale and also enhance electron transportation.[9] The large surface area of the nanomaterials provides a high contact area with the electrolyte for lithium-ion flux across the interface. Furthermore, the chemical potentials of the electrode can be modified,[100] and the strain caused by lithium intercalation can be better accommodated,[101] if nanosized materials are used.

All these benefits result in the employment of nanomaterials as the electrode materials for enhanced performance in lithium rechargeable batteries, which are known as secondary generation lithium batteries.

2.3.2.2 Energy Storage Mechanism

The first-generation lithium rechargeable battery is a lithium-ion battery, which, however, does not contain lithium metal. It is a device consisting of a graphite negative electrode (anode) and a layered $LiCoO_2$ positive electrode (cathode) with a non-aqueous electrolyte. **Scheme 2-3** shows a scheme to illustrate the energy storage involved in this rechargeable unit.

Generally, on charging, lithium ions are deintercalated from the layered $LiCoO_2$ at the cathode, diffuse through the electrolyte to the anode, and are intercalated to graphite between the layers. On discharging, the process reverses with lithium-ions transporting from the anode to the cathode. The secondary generation lithium rechargeable batteries have the same energy storage mechanism, but with nanomaterials as the electrode materials, as discussed in the previous subsection, for improved power density and higher charge/discharge rates.

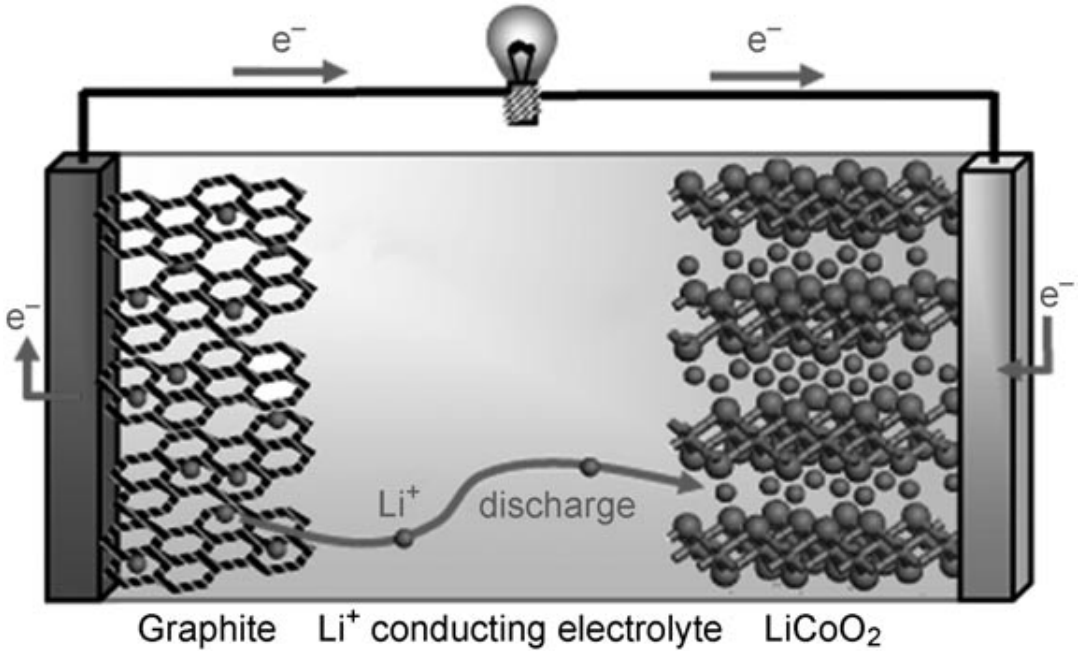

Scheme 2-3 Schematic illustration of the charge/discharge mechanism of a lithium-ion battery.[99]

2.3.2.3 Electrode Materials

Anode Materials

Micrometre sized graphite powders have been the most used anode material in laboratory for rechargeable lithium batteries for many years and are also an important counterpart in the commercial products.[102, 103] To further increase the lithium intercalation/deintercalation rate and thus the power of the battery, nanosized graphite is being investigated as a replacement. When lithium ions are inserted into graphite layers at a potential of less than 0.1 V (*vs.* Li/Li^+), the electrolyte begins to reduce, accompanied by the formation of a passivating (solid electrolyte interface, SEI) layer on the graphite surface.[104-106] The formation of the SEI layer protects graphite electrodes from exfoliation. However, the cover of the SEI layer on such high surface-area graphite often results in the consumption of excessive charge, which is irreversible and causes energy loss from the cell. An associated safety concern has also been raised due to the deposition of highly reactive lithium ions on the graphite surface because of the SEI layer.[99]

An alternative candidate, $Li_4Ti_5O_{12}$, has been selected as lithium intercalation host to replace graphite with combined benefits of inherent protection against lithium deposition, low cost and low toxicity.[99] The lithium intercalation of $Li_4Ti_5O_{12}$ takes place at a relatively higher potential, 1.5 V *vs.* Li/Li^+, ensuring safer operation and alleviating the lithium deposition. However, the capacity of $Li_4Ti_5O_{12}$ (150 mAh g^{-1}) is lower than graphite (372 mAh g^{-1}), leading to a reduced energy density.

The intercalation/deintercalation of lithium-ions is restricted to only one, or at most two, lithium atoms per host. Considering the high activity of lithium, a few transition metal oxides have been reported to react with lithium, termed as conversion, to provide high

capacity for hundreds of cycles. These reactions are highly reversible and occur according to the general formula in the following, where M represents a certain metal:

$$MO + 2\ Li^+ + 2e^- \leftrightarrow Li_2O + M^0 \quad (\textbf{Eq. 2-3}\ [107])$$

These low cost transition metal oxides include the 3d metals with different oxidation states, such as Cu_2O (one), NiO (two), Fe_2O_3 (three), RuO_2 (four), etc. For instance, cubic shaped Cu_2O particles have been shown to sustain their morphology upon cycling, showing an excellent cyclability at a 0.2 C rate with a capacity retention of 390 mAh g^{-1}.[108] Vertically aligned NiO nanowalls exhibited a capacity of 638 mAh g^{-1} at a high current rate of 1.25 C with excellent cycling stability.[109] Templated synthesized α-Fe_2O_3 nanotube arrays delivered a highest specific capacity of 1415 mAh g^{-1} with a retained capacity of 510 mAh g^{-1} (much higher than that of graphite) after 100 cycles.[110] RuO_2 electrodes were reported to generate a high specific capacity of 1130 mAh g^{-1} with a nearly 100% coulombic efficiency at the first cycle, showing that almost all the inserted lithium-ions could be extracted.[111] It can be seen that all of these metal oxides show higher specific capacities and many advances over graphite. The developed conversion reaction has also reached to include a broad range of other materials as high-performance anode materials including sulfides, nitrides, fluorides, and phosphides.[112-117] Current research has been boosted to explore various nanomaterials as a replacement for graphite anodes.

On the other hand, metal alloys, Li_xM_y such as $Li_{4.4}Sn$ and $Li_{4.4}Si$, are also promising candidates as anode materials to store high capacity of lithium, which exceeds the capacity of conventional graphite. The insertion and extraction of lithium come from a proccess called alloying-dealloying. However, to accommodate such high volume of lithium, these metal alloy anodes have to experience severe volume expansion and

contraction, resulting in the failure of the electrodes. To address this issue and retain a stable cycle life, nanosized metal alloys are used to replace bulk materials to render the phase transitions and reduce the cracking of the electrodes. In Chapter 4 and Chapter 8, investigations on Sn and SnO_2 incorporated with graphene as anode materials are reported.

Cathode Materials

Similar to $LiCoO_2$, lithium intercalation compounds are very attractive materials for use in cathodes of lithium rechargeable batteries, and include, for example, $LiMn_2O_2$, $LiMnO_2$, $LiNi_{0.5}Mn_{1.5}O_4$, $LiFeSiO_4$ and Li_2FeSiO_4. Among them, nanoparticulate $LiFePO_4$ has been intensively studied and has received special attention.[118] As a potential cathode material, it offers multiple advantages, such as low cost and high thermal and chemical stability. Additionally, $LiFePO_4$ has a relatively lower voltage against Li/Li^+ (3.4 V) compared to other cathode materials, leading to higher electrochemical stability and lower reactivity to the electrolyte. The intercalation mechanism of $LiFePO_4$ is shown below in **Scheme 2-4**.

First, on charging, lithium is extracted from $LiFePO_4$ resulting in the formation of a $FePO_4$ shell on the surface of the particles. On continuous charging, the boundary of the shell and the $LiFePO_4$ core move through the particle. At a fully charged state, as lithium insertion commences, the $LiFePO_4$ shell gradually forms and then becomes fully discharged $LiFePO_4$ particles.[119] $LiFePO_4$ has been proved to behave quite well with capacities close to its theoretical value.[120] However, the conductivity of the lithium intercalation compounds is extremely low. Coating with conducting carbon is often performed to improve the conductivity of these materials. $LiFePO_4$/C has been prepared

via different methods and has achieved very good rate capability and excellent stability.[13, 121]

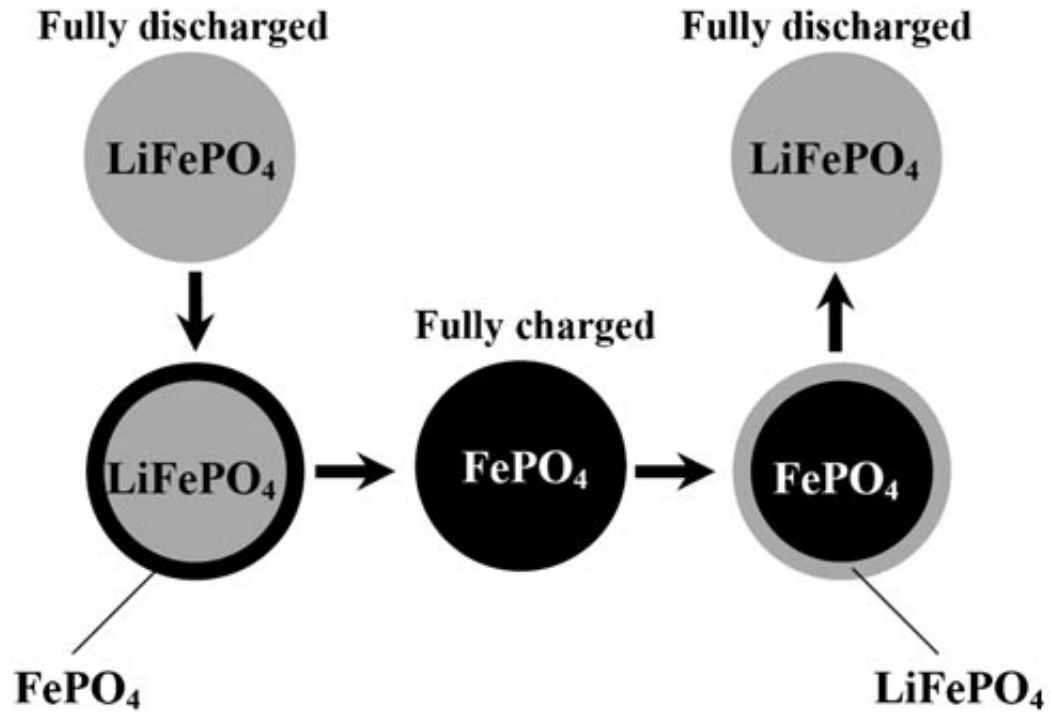

Scheme 2-4 Schematic representation of the processes during charge/discharge of $LiFePO_4$.[99, 119]

Apart from the above mentioned compounds, there are also other materials that could be used as cathode materials. V_2O_5 is a low cost lithium intercalation host, which has a theoretical capacity of 437 mAh g^{-1}. But its high toxicity renders it useless, practically. Elemental sulfur is a cheap product with a very high theoretical capacity of 1675 mAh g^{-1} compared with other potential cathode materials. Considering its great potential, researchers all over the world have explored lithium-sulfur batteries as an alternative to lithium-ion batteries. The advantages and disadvantages associated with sulfur as a cathode material are discussed in detail in Chapter 9.

Graphene and Graphene-based Materials

It is well recognized that the maximum specific lithium insertion capacity for graphite (3D network of graphene) is 372 mAh g^{-1}, which corresponds to the formation of LiC_6 – a first stage graphite intercalation compound (GIC). During the intercalation process, lithium transfers its 2s electrons to the carbon host and is situated between the carbon sheets. High capacity carbon materials have also been reported. This can be mainly ascribed to (i) lithium insertion within the "cavities" in carbon,[122] (ii) lithium absorption on both sides of the carbon sheet,[123] and (iii) lithium binding on the so called "covalent" sites.[124] Owing to its large surface-to-volume ratio and highly conductive nature, graphene may deliver a high lithium storage capacity in lithium-ion batteries. Based on first principle calculations, lithium can be stably stored on both sides of graphene nanosheets, inducing a theoretical capacity of 744 mAh g^{-1}, which is two times that of graphite.[125]

In reports of the employment of graphene as an anode material, graphene has been shown to be capable of delivering large reversible lithium storage (540 mAh g^{-1} in the first cycle) with a retained capacity of 460 mAh g^{-1} in the 100th cycle; a much better performance than a graphite anode.[35] As discussed earlier, graphene nanosheets always naturally stack into multiple layers and this results in limited accessibility of the sheets to lithium, causing the real capacity to be much lower than the theoretical value. Graphene-based nanocomposites with jammed nanocrystals are therefore synthesized to prevent the re-stacking of graphene nanosheets.

The metal oxide/graphene nanocomposites such as SnO_2/GNS have been prepared by reassembling graphene monolayers in the presence of SnO_2 nanoparticles[126] and by in-situ chemical reduction.[127] The SnO_2/GNS nanocomposites from both methods

have been shown to have better lithium storage capacities than bare graphene nanosheets and excellent cycling stability. A super-paramagnetic composite such as Fe_3O_4/GNS was produced via a chemical deposition. This product was shown to have promising applications for lithium-ion batteries.[128] In the case of CuO/GNS, the material was prepared from CuO and graphene upon reduction using hydrazine vapor.[129] The formation of TiO_2/GNS composite was reported to have been facilitated by SO_4^{2-} surfactants, which acted as the stabilizer of the graphene monolayers in situ.[130] The prepared TiO_2/GNS composite exhibited more than double the specific capacity of pure TiO_2 phase at high charge rate.

2.4 Summary

An overview of graphene from its history, properties, and preparation to its application is briefly stated in this chapter. Graphene, since its discovery in 2004, has raised worldwide research interest. The synthesis of high-quality and large-scale graphene nanosheets has been developing well and there have been remarkable outcomes regarding applications of graphene nanosheets in energy storage devices, especially supercapacitors and lithium-ion batteries. Graphene represents a promising low-cost carbon material for a broad range of practical applications and its potential in electronics will be further developed in the near future.

Chapter Three

Materials Characterization and Electrochemical Techniques

Chapter 3 — Materials Characterization and Electrochemical Techniques

To fulfill the research tasks, experimental work was performed in the laboratory, followed by characterizations of the obtained materials and evaluation of their electrochemical properties. In the following part of this chapter, experimental technicalities are presented, including the materials and chemicals used in the research project, typical materials synthesis methods, basic materials characterization techniques, electrode fabrication and cell assembly details, and electrochemical testing specifications.

3.1 Materials and Chemicals

A list of the names of materials and chemicals used in the research project, along with their formula, purity and supplier, is shown below in **Table 3-1**.

Table 3-1 Materials and chemicals used in the research project.

Materials and Chemicals	Formula	Purity	Supplier
1,2-Dimethoxyethane (DME, anhydrous)	$CH_3OCH_2CH_2OCH_3$	99.5%	Sigma-Aldrich
1,3-Dioxolane (DOX, anhydrous)	$C_3H_6O_2$	99.8%	Sigma-Aldrich
Carbon black	C	99%	Lexel
Citric acid	$HOC(COOH)(CH_2COOH)_2$	99.5%	Sigma-Aldrich
Cobalt(II) chloride hexahydrate	$CoCl_2 \cdot 6H_2O$	98%	Sigma-Aldrich

Cobalt(II, III) oxide (<50 nm)	Co_3O_4	99.5%	Aldrich
Ethanol	CH_3CH_2OH	99.5%	Sigma-Aldrich
Ethylene glycol (EG, anhydrous)	$HOCH_2CH_2OH$	99.8%	Sigma-Aldrich
Graphite (natural flakes)	C	75%	Aldrich
Hydrazine hydrate	$NH_2NH_2 \cdot xH_2O$	50–60%	Sigma-Aldrich
Hydrochloric acid	HCl	37%	Sigma-Aldrich
Hydrogen peroxide solution	H_2O_2	30–32%	Sigma-Aldrich
L-cysteine	$HSCH_2CH(NH_2)CO_2H$	98%	Sigma
Lithium bis(trifluoromethane sulfon)imide (LiTFSI)	$CF_3SO_2NLiSO_2CF_3$	99.95%	Aldrich
Lithium foil	Li	99.999%	Hohsen Corporation Japan
Lithium perchlorate	$LiClO_4$	99.99%	Aldrich
Lithium-ion battery electrolyte (LB-303)	1 M $LiPF_6$ in ethylene carbonate (EC) and dimethyl carbonate (DMC) (1:1 w/w)	–	Guotai-Huarong New Chemical Materials Co.Ltd, China
N-Methyl-2-pyrrolidinone (NMP, anhydrous)	C_5H_9NO	99.5%	Sigma-Aldrich
Poly(vinylidene difluoride) (PVdF)	$(CH_2CF_2)_n$	–	Aldrich
Potassium hydroxide	KOH	90%	Sigma-Aldrich
Potassium permanganate	$KMnO_4$	99%	Sigma-Aldrich
Propylene carbonate (PC, anhydrous)	$C_4H_6O_3$	99.7%	Sigma-Aldrich

Sodium borohydride	$NaBH_4$	99.99%	Aldrich
Sodium nitrate	$NaNO_3$	99%	Sigma-Aldrich
Sodium sulfate (anhydrous)	Na_2SO_4	99%	Sigma-Aldrich
Sulfur	S	99.5%	Sigma-Aldrich
Sulfuric acid	H_2SO_4	95–98%	Sigma-Aldrich
Tetrabutylammonium borohydride ($TBABH_4$)	$(CH_3CH_2CH_2CH_2)_4N(BH_4)$	98%	Aldrich
Tetraoctylammonium bromide (TOAB)	$[CH_3(CH_2)_7]_4N(Br)$	98%	Aldrich
Tin	Sn	99%	Aldrich
Tin(II) chloride dihydrate	$SnCl_2 \cdot 2H_2O$	98%	Sigma-Aldrich
Toluene (anhydrous)	$C_6H_5CH_3$	99.8%	Sigma-Aldrich

3.2 Materials Synthesis

There have been a number of literature reports of synthesis techniques to produce graphene related nanocomposite materials. Below are some of the chemical methods used in this research project to successfully obtain the specified materials.

3.2.1 In-situ Reduction

The term “in-situ” means “in position” literally and represents “in the reaction mixture” in this thesis, when it is related to chemical reactions. In-situ reductions are carried out

with mixed reagents in a flask under reflux conditions in a water or oil bath. By heat treatment, the starting materials are reduced simultaneously to the final product; this technique is often used to prepare graphene-based nanocomposite materials with simultaneous reductions of GONS to GNS and metal cations to metal atoms. The metal atoms could then be oxidized again in air to metal oxides. Successful attempts at using in-situ reduction for preparing Sn/GNS and Co_3O_4/GNS are reported in Chapter 4 and Chapter 6 in this thesis.

3.2.2 Co-precipitation

Graphene nanosheets are often stacked in the dry state and are highly hydrophobic. The idea of co-precipitation is to prepare an aqueous or organo- solution, suspension or gel of the desired nanomaterial to mix with graphene organo-suspension thoroughly, resulting in well distributed nanocrystals between well-separated graphene layers in the mixture suspension, which is then simultaneously precipitated to form agglomerations as the final product. As a result, the nanocrystals will be jammed onto graphene nanosheets. Mn_3O_4/GNS has been prepared via this route and the experimental details are presented in Chapter 5.

3.2.3 Hydrothermal and Solvothermal

Synthesis using a “hydrothermal” or a “solvothermal” method is often performed in an apparatus called an autoclave to produce large-quantity, well crystallized, morphology controlled nanocrystals. The crystal is grown in hot solvent under high pressure, depending on the solubility of the precursors. A gradient of temperature is maintained at opposite ends

of the growth chamber, so that the hotter end dissolves the nutrient and the cooler end facilitates growth of the crystal seeds. A controlled calcination always follows to execute a transformation of the grown crystals to a designated phase or to further increase the crystallinity of the product. Hydrothermal synthesis uses DI water as the solvent, while solvothermal preparation involves organic solvents or a mixture of different organic or organic/aqueous solvents.

SnO_2/GNS and CoS_2/GNS have been prepared via the solvothermal technique as presented in Chapter 7 and Chapter 9 respectively. The size of the decorated nanoparticles was very well controlled and the distribution of the nanoparticles is further improved.

3.2.4 Simple Incorporation

A sulfur imbibing process that takes advantage of the low melting point of sulfur can be used to prepare sulfur incorporated graphene nanosheets. Sulfur is mixed with graphene prior to a low temperature heat treatment. The sublimed sulfur can easily diffuse into the interlayer space of graphene nanosheets and accommodate itself there when it is cooled off. This simple incorporation can be done in a conventional oven at a mild temperature. The entire experimental details of the synthesis of S/GNS are given in Chapter 8.

3.3 Materials Characterization

The following materials characterization techniques were implemented in the research project to identify the phases, present the textural features, and determine the compositions of the as-prepared materials.

3.3.1 X-ray Diffractometry

X-ray diffractometry is a non-destructive analytical characterization method to determine the crystal phase and structure. An X-ray diffractometer generates an X-ray beam hitting a sample as a function of incident and scattered angle, polarization, and wavelength or energy. A certain sample has a particular atom arrangement within the unit cell and this will lead to particular relative intensities of the recorded diffraction peaks upon X-ray hitting. Therefore, the unit cell size and geometry may be resolved from the angular positions of the X-ray diffraction results. The resultant diffraction lines with obvious peaks together are called an XRD pattern; it can provide information on crystal structure, chemical composition, and physical properties of materials and thin films. The basic use of XRD in this research project was to determine the actual phase of the as-prepared product by comparing the obtained XRD pattern to known standard diffraction lines in the Joint Committee on Powder Diffraction Standards (JCPDS) database. **Fig. 3-1** shows an X-ray diffractometer (Siemens D5000) located at the Microstructural Analysis Unit (MAU), University of Technology Sydney (UTS) able to analyze up to 50 samples with a single loading.

Fig. 3-1 An X-ray diffractometer (Siemens D5000 model). (Image captured from the Science Faculty Resource Manage System, UTS)

3.3.2 Scanning Electron Microscopy and Transmission Electron Microscopy

Electron diffraction is a characterization technique used to study matter by firing a beam of accelerated electrons to a sample to obtain the interference pattern. Electron diffraction is usually performed in a scanning electron microscope (SEM) and a transmission electron microscope (TEM) to study the crystal structure of solids and examine their specific morphology.

An SEM images a sample by scanning it in a raster scan pattern with the excited electron beam. The atoms that make up the sample produce signals during each scan to deliver information about the sample's surface topography, composition, and other properties such as electrical conductivity. A Field Emission SEM (FE-SEM) is equipped with a field emission cathode in the electron gun to provide enhanced resolution and to minimize the charge issues and sample damage. **Fig. 3-2** displays a typical FE-SEM facility (Zeiss Supra 55VP).

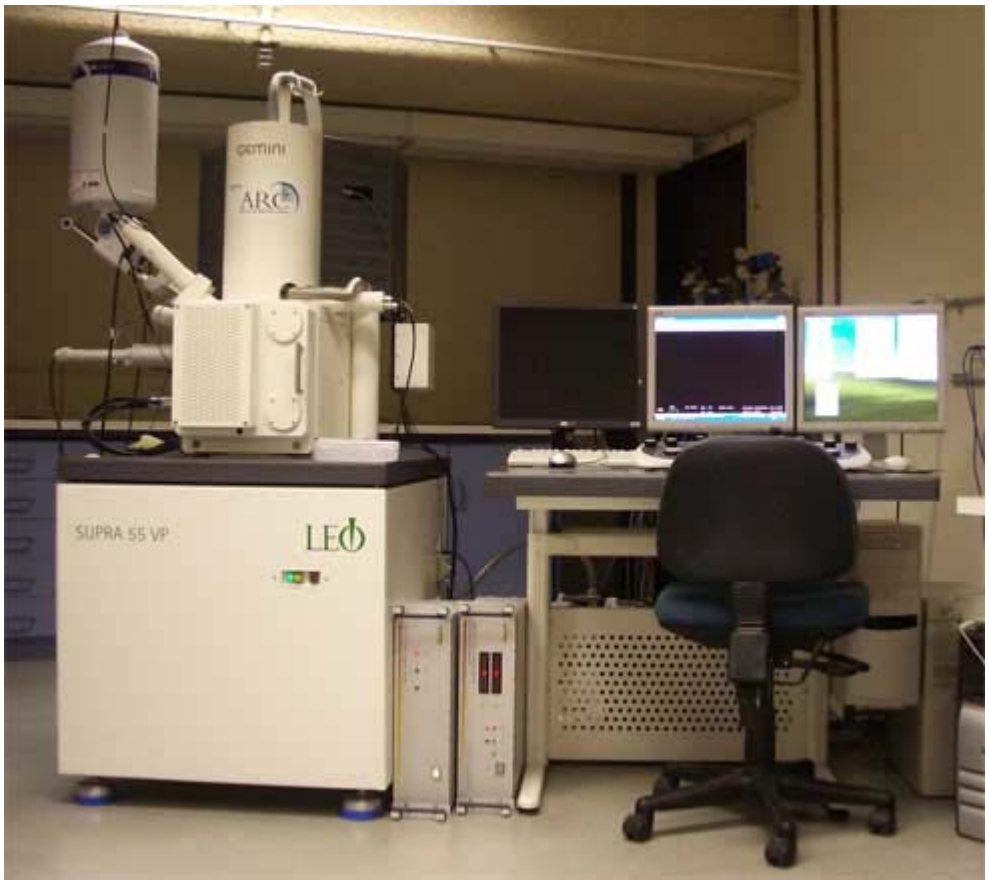

Fig. 3-2 An FE-SEM facility (Zeiss Supra 55VP). (Image captured from the Science Faculty Resource Manage System, UTS)

The beam of electrons in a TEM, on the other hand, is transmitted through an ultra thin sample on a copper grid, interacting with the sample as the electrons pass through to generate images. TEMs are capable of imaging at a very high resolution to reveal information at nanometre scale, such as lattice planes, *d*-spacing, etc., so they have better resolution than SEMs. Generally, SEMs (FE-SEMs) are used for preliminary analysis while TEMs are on duty for in-depth investigations of lattice parameters and very fine nanostructures. **Fig. 3-3**, as shown below, presents a commercial TEM setup (JEOL 2011 model).

Fig. 3-3 A commercial TEM setup (JEOL 2011 model).[131]

3.3.3 Atomic Force Microscopy

Atomic force microscopy is a very powerful high-resolution scanning probe microscopy, which was developed to overcome the drawback associated with Scanning Tunneling

Microscopy; Scanning Tunneling Microscopy only deals with conducting and semiconducting samples. Atomic Force Microscope (AFM) can examine almost any type of sample including ceramics, composites, polymers, as well as bio-samples in air or solutions with demonstrated nanoscaled resolution. AFM uses electric potentials to detect surface features by conducting cantilevers, which are equipped with high-resolution silicon tips to engage with the sample surface, moving along it in different modes and returning signals as electric potentials. In the research investigation reported in this thesis, AFM is used with a Tapping Mode to further confirm the existence of graphene and graphene-based nanocomposites. Graphene and the sandwiched nanocrystals can be easily identified and the sheet thickness and particle sizes can be evaluated by the relevant height differences upon scanning. **Fig. 3-4** illustrates one of the most advanced AFM (MFP-3D-SA model) manufactured by Asylum Research.

Fig. 3-4 A MFP-3D-SA AFM facility manufactured by Asylum Research.[132]

3.3.4 Raman Spectroscopy

Raman spectroscopy is a non-destructive spectroscopic technique used to study vibrational, rotational, and other low-frequency modes in a molecular system. The laser light in the Raman Microscope focuses on the test sample and interacts with its vibrations or excitations at a molecular level, generating shifted laser photons, which are immediately recorded on a Raman spectrum. The resolution of the Raman spectra can be enhanced by accumulated scans with a longer exposed time.

In the study of graphene and graphene-related materials, carbon atoms are only bonded into a sp^2 arrangement forming C-C single bonds, which infrared spectroscopy is unable to detect. This makes Raman Spectroscopy really helpful in determining ordered and disordered crystal graphitic structures as supporting evidence for the formation of graphene nanosheets and, also, to distinguish graphene from pristine graphite and graphene oxide. **Fig. 3-5** shows a Renishaw inVia Raman Microscope.

Fig. 3-5 A Renishaw inVia Raman Microscope. (Image captured from the Science Faculty Resource Manage System, UTS)

3.3.5 Brunauer-Emmett-Teller Surface Area and Barrett-Joyner-Halenda Pore Size and Volume Analysis

Brunauer-Emmett-Teller (BET) and Barrett-Joyner-Halenda (BJH) are analysis theories for determining surface area, pore size and pore volume of the desired materials. The abbreviated terms of BET and BJH are named from the initials of the family names of those developers. BET analysis examines the external area and pore area of the materials to determine the total specific surface area in m^2 g^{-1} by nitrogen multilayer adsorption isotherms. BJH analysis can also be employed to determine pore area and specific pore volume using nitrogen adsorption and desorption techniques to characterize pore size distribution of the sample. Both BET surface area and BJH pore size distribution can be derived from the nitrogen adsorption and desorption isotherms obtained from a surface area analyzer as shown in **Fig. 3-6**.

Fig. 3-6 A TriStar II Surface Area Analyzer.[133]

3.3.6 Thermogravimetric Analysis

Thermogravimetric Analysis (TGA) is a type of measurement to determine the weight changes of samples associated with changes in temperature. This analysis accurately detects the weight of a sample as temperature elevates, drawing a continuous line to identify weight loss processes in relation to the chemical reactions occurring. TGA can be carried out in air or noble gases for different applications. In the case of graphene-based nanocomposite materials, TGA is often conducted in air as a quantitative method to determine the composition of graphene and the embedded nanoparticles. **Fig. 3-7** shows a typical TGA instrument of TA Instruments.

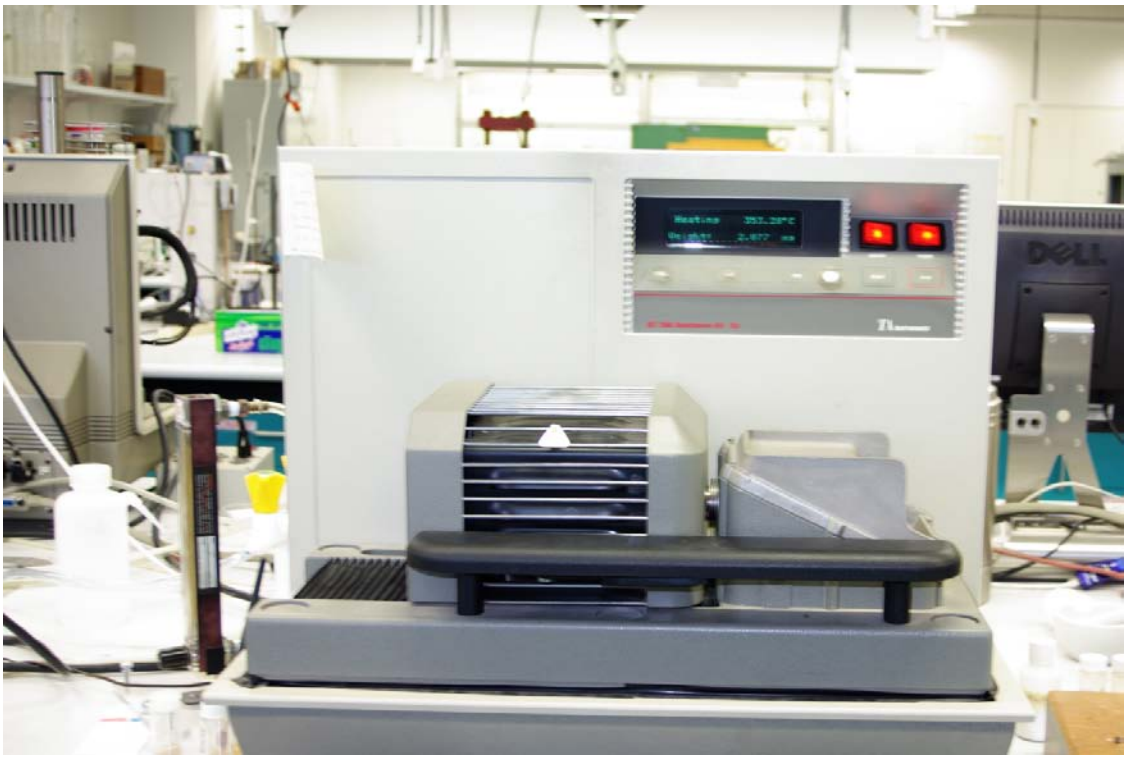

Fig. 3-7 A TGA/DTA Analyzer (SDT 2960 model, TA Instruments). (Image captured from the Science Faculty Resource Manage System, UTS)

3.4 Electrode Fabrication and Cell Assembly

3.4.1 Electrode Fabrication

The active materials (e.g. graphene-based nanocomposite materials in this study), carbon black and PVdF powders are pre-weighed before mixing them together. The weight ratio of carbon black often varies, in relation to the conductivity of the active materials. The three ingredients are ground thoroughly in a mortar followed by the addition of a small volume of NMP to form a slurry upon continuously grinding.

For supercapacitors, the slurry is usually pasted on platinum foils for a three-electrode test cell with an aqueous electrolyte. Alternative substrates could be titanium and stainless steel plates. When an organic electrolyte is used, the slurry is usually pasted onto nickel foams, which will be assembled like a battery cell in the glove box. For lithium-ion batteries, the mixture is pasted on aluminum foils for cathode materials and copper foils for anode materials. The fabricated electrodes are immediately taken to an oven and dried under vacuum at around 100 °C overnight.

3.4.2 Cell Assembly

To assemble CR2032 type coin cells, the dried electrodes are weighed individually to identify the actual weight of active mixture pasted on the substrates. The weighed electrodes are pressed between two dies under a pressure of approximately 200 kg cm^{-2} on a press machine and then transferred into an argon-filled glove box, where the oxygen and moisture levels are always controlled below 0.1 ppm. The glove box maintains an argon atmosphere at all times to avoid oxidation and the severe reactions

of lithium metal caused by moisture and oxygen, and ensures a safe operational environment. A typical glove box manufactured by MBraun, Germany is illustrated below in **Fig. 3-8**.

Fig. 3-8 A Unilab glove box, manufactured by MBraun, Germany.

For typical lithium-ion cells, the assembly is performed in the order of a battery shell, a working electrode with pasted mixture facing up, a few drops of the electrolyte, a polytetrafluoroethylene (PTFE) membrane separator, a few drops of the electrolyte, a lithium foil, a stainless steel gasket, a spring and a battery cover. This whole unit is then sealed completely by being crimped with a hand-operated crimping tool. The assembly

of a supercapacitor cell in a two-electrode configuration is very similar to that of a lithium cell, except that the two working electrodes face each other and a glassy fibre separator is sandwiched between the working electrodes. The details of the fabrication of a supercapacitor cell are discussed in Chapter 9. The assembled cells are then removed from the glove box and left for at least 12 h to allow the electrolyte to completely soak the electrode prior to any electrochemical measurements.

For a supercapacitor test cell using a three-electrode configuration with an aqueous electrolyte, the dried electrodes are subject to similar weighing and press processes. Then, the test cell is fabricated with a working electrode facing a counter electrode (platinum foil) and a reference electrode (saturated calomel electrode, SCE), which is placed close to the working electrode. The three-electrode cell is also left for one or two hours before any electrochemical testing.

3.5 Electrochemical Testing

The assembled test cells were electrochemically tested for a systematic study of the electrochemical properties of the active materials. These electrochemical measurements often included Cyclic Voltammetry, galvanostatic charge/discharge and Electrochemical Impedance Spectroscopy, which will be discussed below. The overall electrochemical performance can be further evaluated from all these results.

3.5.1 Cyclic Voltommetry

Cyclic Voltammetry (CV) is a type of potentiodynamic electrochemical measurement, recording a relationship of current *vs.* voltage when the potential at the working

electrode is ramped linearly versus time (at a certain scan rate) to a set potential and reversed back to the original potential at the same sweep rate. CV is generally used to examine the electrochemical properties of an analyte in solution upon a single or a few scans. In the examining voltage range, an analyte can be reduced or oxidized on a forward scan as the scan proceeds, and then re-oxidized or re-reduced on the return scan, as a sign of highly reversible redox couples.

For supercapacitors and lithium rechargeable batteries, the tests of CV reveal the specific reactions, which can be determined from the redox peak potentials, and further confirm the energy storage mechanism involved. CV curves can be also used to compute the specific capacitance of the active material using the relationship shown below. The area under the current–potential curve can be estimated by integration, and then the area is divided by the sweep rate (v, V s^{-1}), the mass of active material of the electrode (m, g), and the potential window ((V_a-V_b), V), giving a specific capacitance (C) in F g^{-1}:

$$C = \frac{1}{mv(Va-Vb)} \int_{Va}^{Vb} I(V)\, dV \quad \textbf{(Eq. 3-1)}$$

In the research project reported in this thesis, all CV tests were conducted on an electrochemistry workstation. **Fig. 3-9** shows an electrochemistry workstation device (CHI660D model) serving in the lab of the Centre for Clean Energy Technology, UTS.

Fig. 3-9 An electrochemistry workstation (CHI660D model).

3.5.2 Galvanostatic Charge/Discharge

Galvanostatic charge/discharge tests are electrochemical tests in which constant current is applied through an electrolytic test cell. For three-electrode supercapacitor test cells, the galvanostatic charge/discharge performance is examined by a chromapermmtery technique on an electrochemistry workstation with an aqueous electrolyte in open circumstances. For a two-electrode configuration (both supercapacitor and lithium battery with an organic electrolyte) in a closely sealed coin cell, a battery tester is often used. Galvanostatic charge/discharge tests exhibit electrochemical information on charge/discharge profiles, Columbic efficiency, and long-term cycling properties. A set

of typical battery testers (Neware) with multiple channels is shown below in **Fig. 3-10**. Coin cells can be tested at the same time in different channels.

Fig. 3-10 A set of Neware battery testers.

3.5.3 Electrochemical Impedance Spectroscopy

Electrochemical Impedance Spectroscopy (EIS), also called Alternating Current (AC) Impedance, was employed to characterize the dynamics of an electrochemical process in terms of an electrochemical cell's response to an applied potential at different

frequencies. The use of EIS in batteries and supercapacitors often provides an estimation of the internal resistance (electrolyte resistance and charge-transfer resistance) at an open circuit potential or under other conditions. The use of EIS tests to accompany other electrochemical results leads to a better understanding of the internal electrochemical processes.

Chapter Four

Sn/Graphene Nanocomposite with 3D Architecture for Enhanced Reversible Lithium Storage in Lithium-Ion Batteries

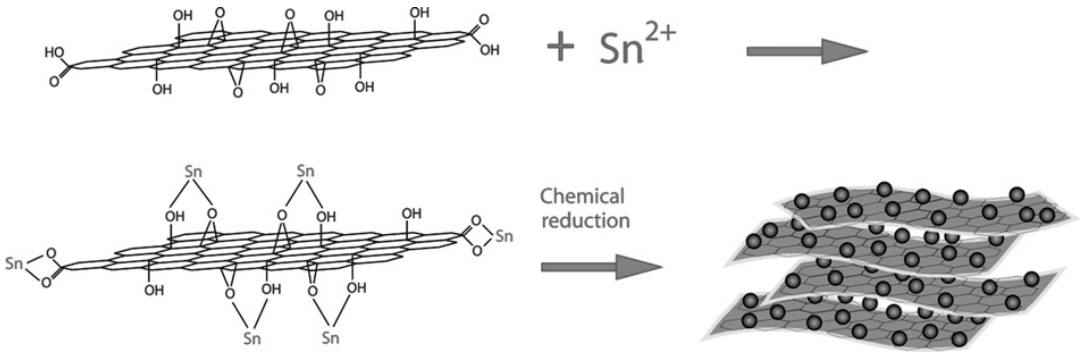

Chapter 4 — Sn/Graphene Nanocomposite with 3D Architecture for Enhanced Reversible Lithium Storage in Lithium-Ion Batteries

4.1 Introduction

Sn and Sn based compounds have been extensively investigated as high capacity anode materials for lithium-ion batteries.[134] The reaction between lithium and Sn can be described as:

$$4.4\ Li^{+} + Sn + 4.4e^{-} \leftrightarrow Li_{4.4}Sn \quad (\textbf{Eq. 4-1})$$

The above reaction is reversible with a theoretical capacity of 994 mAh g^{-1}, based on the mass of Sn, which is 2.67 times that of graphite. However, Sn atoms tend to aggregate during repeated cycling, inducing rapid loss of capacity of the electrode. Since graphene nanosheets are flexible and naturally corrugated, the deposition of nanosized Sn particles on graphene will form a 3D nanocomposite architecture, which not only can effectively prevent the re-stacking of graphene nanosheets, but also circumvent the aggregation of Sn atoms on cycling. Such a nanocomposite could deliver an enhanced electrochemical performance as an anode material in lithium-ion batteries.

The synthesis of Sn/GNS nanocomposite and its electrochemical performance as an anode material in lithium-ion batteries is reported in this chapter. A general strategy is demonstrated here, to achieve optimum electrochemical performance by constructing a nanocomposite architecture from the combination of nanosized Sn particles and graphene nanosheets.

4.2 Experimental

4.2.1 Material Synthesis

Graphene oxide nanosheets (GONS) were synthesized from natural graphite powders by a modified Hummer's method.[36] In a typical synthesis of Sn/GNS nanocomposites, 40 mg GONS was dispersed in DI water by ultrasonication. The dispersion was then mixed with 40 ml aqueous solution of $SnCl_2 \cdot 2H_2O$ (20 mg) and citric acid (20 mg). The mixture was transferred into a 250 ml round-bottomed flask. The flask was purged with high purity argon as a protecting gas. Fifty ml $NaBH_4$ (200 mg) aqueous solution was gradually added to the mixture to reduce Sn^{2+} to Sn and GONS to GNS. The mixture was stirred at 0 °C (ice bath) for 3 h. The resultant black solid products were separated by filtration, washed with DI water, and dried in vacuum at 40 °C. To improve the crystallinity of Sn in GNS, the product was annealed at 200 °C for 15 h in argon atmosphere. Bare graphene nanosheet powders were also prepared using the same process. The weight content of Sn in Sn/GNS nanocomposite was quantitatively analyzed by chemical analysis. The composite was dispersed in diluted hydrochloric acid, through which Sn was dissolved. Then, the dispersion was filtered, washed by DI water, and finally dried in vacuum oven. The filtered material contained only graphene nanosheets. By weighing the dried material, the content of Sn was determined to be 35 wt%.

4.2.2 Materials Characterization

The structure and morphology of the Sn/GNS nanocomposite was analyzed by XRD (Philips 1730 X-ray diffractometer), FE-SEM (JEOL 7001F), and TEM (JEOL 2011

TEM facility). AFM images of graphene nanosheets were taken in tapping mode using a SPM Dimension 3100 from Veeco. Room temperature Raman spectra of the nanocomposite were collected on a Jobin Yvon HR800 confocal Raman system with 632.8 nm diode laser excitation on an 1800-line grating.

4.2.3 Electrochemical Testing

Sn/GNS powders were mixed with a binder (PVdF) at a weight ratio of 90:10 in NMP solvent to form a slurry. Then, the resultant slurry was pasted uniformly on copper foil substrates with a blade. These prepared electrode sheets were dried at 100 °C in a vacuum oven for 12 h and pressed under a pressure of approximately 200 kg cm^{-2}. CR2032 type coin cells were assembled in a glove box for electrochemical characterization. The electrolyte was 1 M $LiPF_6$ in a 1:1 mixture of ethylene carbonate and dimethyl carbonate. Li metal foil was used as the counter and reference electrode. The cells were galvanostatically charged and discharged at a current density of 55 mA g^{-1} within the range 0.01 V to 3.0 V. CV curves were measured at 0.1 mV s^{-1} within the range of 0.01–3.0 V using an electrochemistry working station (CHI660C).

4.3 Results and Discussion

Fig. 4-1(a) shows an XRD pattern of the as-synthesized Sn/GNS nanocomposite. The diffraction peaks of crystalline Sn nanoparticles are clearly distinguishable. All strong diffraction lines can be indexed to the tetragonal Sn phase, indicating the strongly crystalline nature of the Sn nanoparticles. The intensity of the diffraction line from the

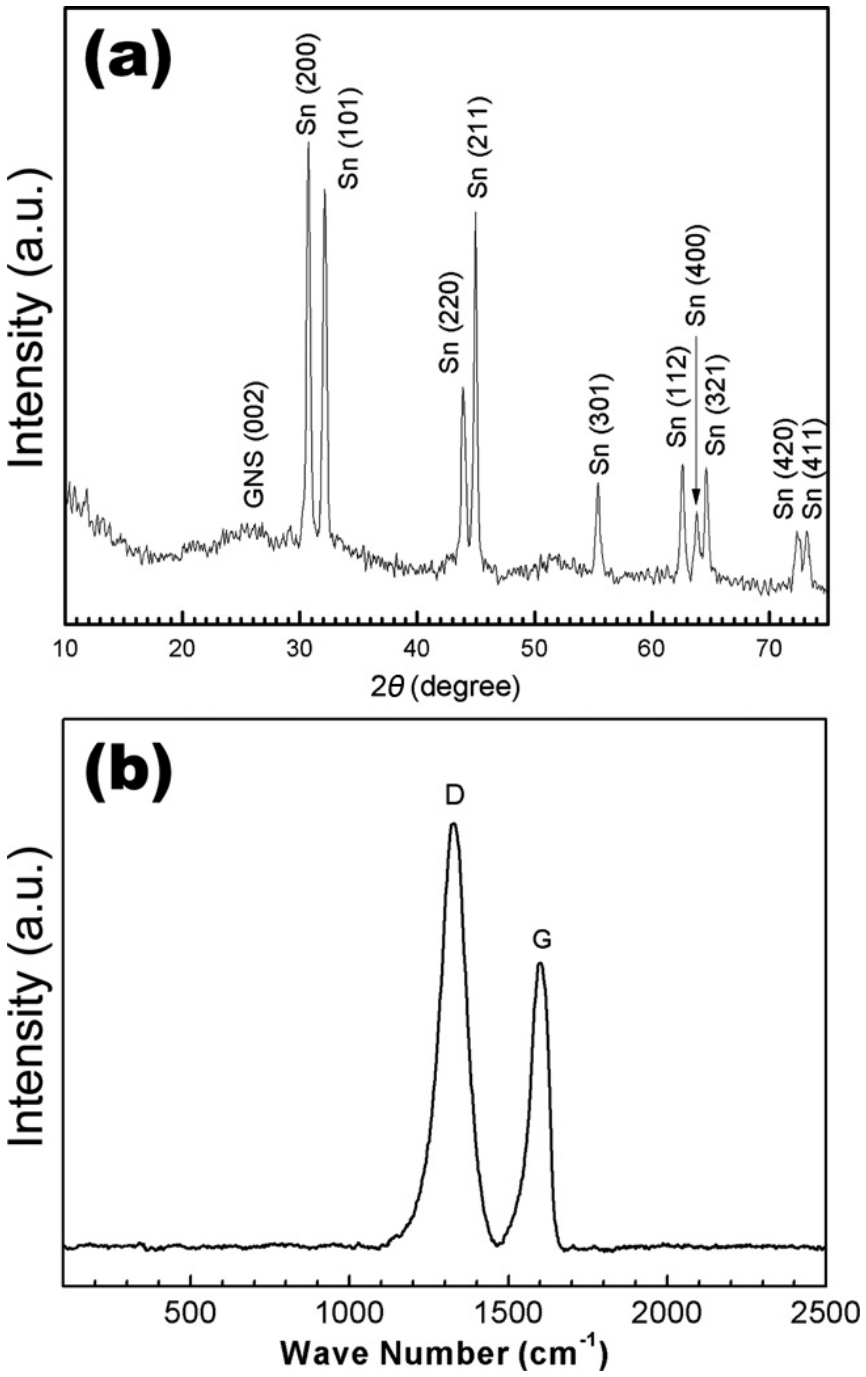

Fig. 4-1 (a) XRD pattern of Sn/GNS nanocomposite. (b) Raman spectrum of Sn/GNS nanocomposite.

graphene nanosheets is relatively weak. Raman spectroscopy further confirmed the crystalline structure of Sn/GNS nanocomposite (as shown in **Fig. 4-1(b)**), in which the Raman peaks of D line and G line of graphene can be easily distinguished. The G line is

assigned to the E_{2g} phonon of sp^2 carbon atoms, while the D line is a breathing mode of κ-point phonons of A_{1g} symmetry.[135, 136] The broadening of D and G bands and the strong D line are indicative of the smaller in-plane sp^2 domains and partially ordered graphitic crystal structure of graphene nanosheets.[27] No other Raman peak appeared in the spectrum, indicating Sn nanoparticles surrounded by graphene nanosheets were not oxidized because SnO_2 usually shows strong Raman peaks.

The morphology of the Sn/GNS nanocomposite was observed by FE-SEM. **Fig. 4-2** shows a FE-SEM image of the Sn/GNS nanocomposite. In general, graphene nanosheets were crumpled to a curly and wavy shape, resembling flower petals. Tiny Sn nanoparticles are homogeneously distributed on the curly graphene nanosheets. The

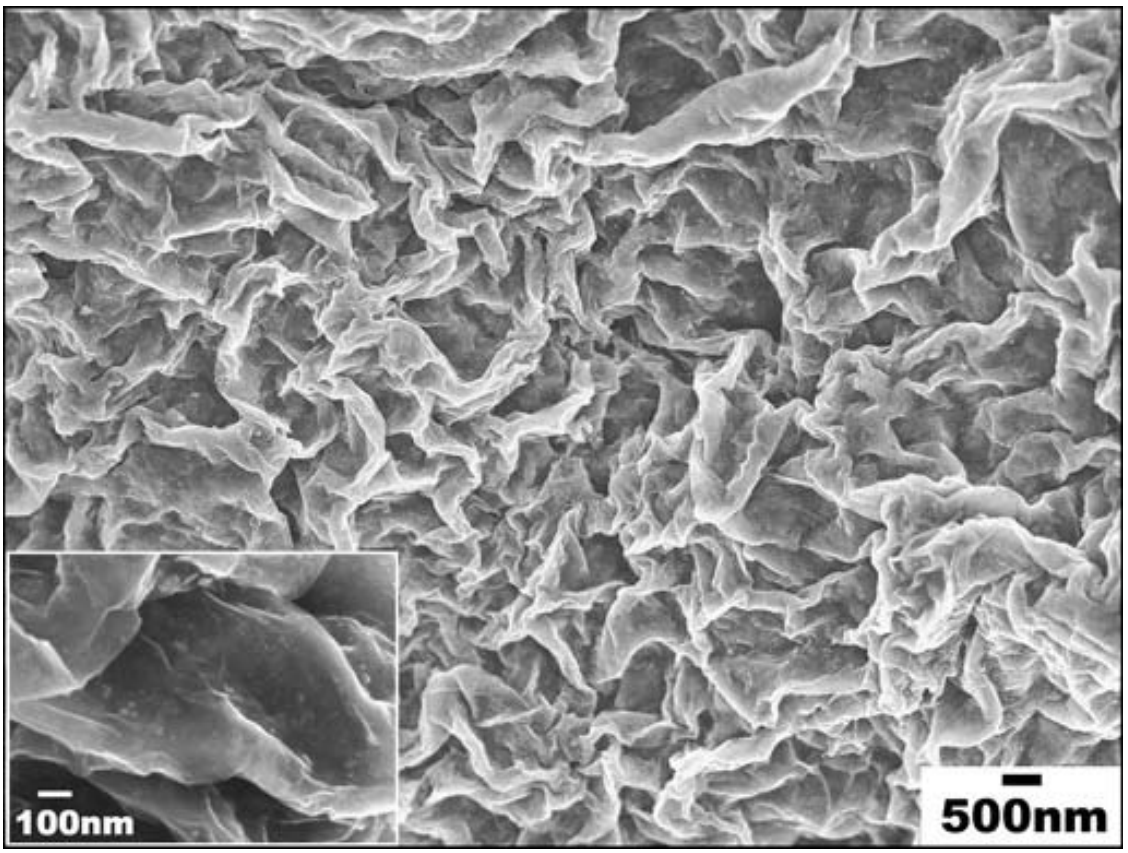

Fig. 4-2 FE-SEM image of Sn/GNS nanocomposite. The inset is the high magnification FE-SEM image, in which Sn nanoparticles are clearly visible.

inset in **Fig. 4-2** shows a high magnification view of the Sn/GNS, in which Sn nanoparticles are clearly visible. Due to the corrugated nature of the graphene nanosheets, substantial voids exist between individual nanosheets. The deposited Sn nanoparticles could act as a spacer to prevent the re-stacking of individual graphene nanosheets. During the synthesis process, an aqueous solution of graphene oxide nanosheets was first prepared as the precursor for the deposition of Sn nanoparticles. It is well known that graphene oxide nanosheets contain carboxylic acid groups on the edge sites and epoxyl and hydroxyl moieties on the basal plane.[137] When Sn^{2+} ions were added into the graphene oxide nanosheet solution, the Sn^{2+} ions were attached to those functional groups.[138] On chemical reduction, graphene oxide nanosheets were converted to graphene nanosheets, and the anchored Sn^{2+} ions were reduced to Sn. The synthesis process here is different from previously reported techniques for the preparation of SnO_2/GNS[126] and TiO_2 nanocomposites,[139] in which nanoparticles were mechanically mixed with graphene nanosheets. By contrast, the process in this chapter involves, in the first step, attaching Sn^{2+} cations onto graphene oxide nanosheets that were homogeneously dispersed in water. Therefore, the mixing of Sn^{2+} and graphene oxide nanosheets can be considered as occurring at the molecular level (graphene oxide nanosheets can be considered macromolecules). In the second step, graphene oxide nanosheets and Sn^{2+} cations were reduced to graphene nanosheets and Sn nanoparticles respectively. This process ensures the in-situ formation of Sn nanoparticles and graphene nanosheets simultaneously, with the advantage that any serious stacking of graphene nanosheets is prevented. **Scheme 4-1** is a schematic diagram of the formation process of the 3D Sn/GNS nanocomposite.[138] FE-SEM observation clearly confirmed the successful deposition of the Sn nanoparticles on graphene nanosheets.

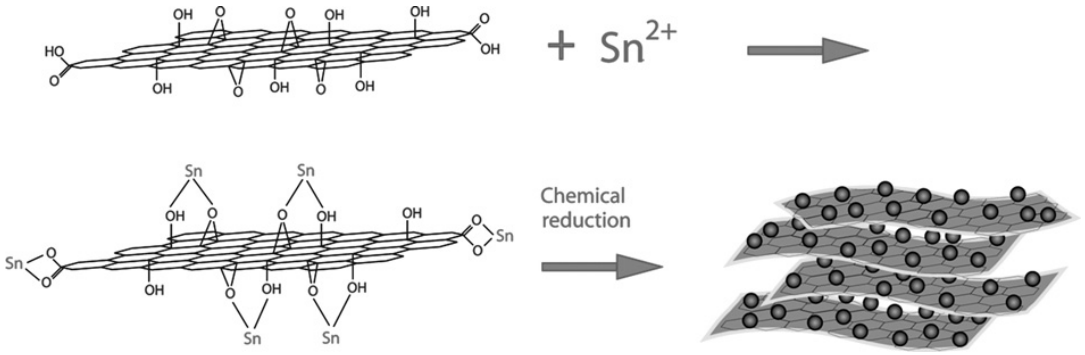

Scheme 4-1 Schematic diagram of the synthesis of the Sn/GNS nanocomposite with a 3D architecture.

The crystalline structure of the Sn/GNS nanocomposite was further analyzed by TEM and high resolution TEM (HRTEM). **Fig. 4-3(a)** shows a low magnification TEM image of the Sn/GNS nanocomposite. Sn nanoparticles are distributed uniformly on a 2D graphene nanosheet substrate. The inset in **Fig. 4-3(a)** is the corresponding selected area electron diffraction (SAED) pattern. All diffraction rings can be indexed to tetragonal Sn phase. A high magnification TEM image of Sn/GNS is shown in **Fig. 4-3(b)**, which even more clearly demonstrates the homogeneous distribution of the Sn nanoparticles. The average particle size of Sn is about 2–5 nm (more than 200 counts). **Fig. 4-3(c)** presents an HRTEM image of the Sn/GNS nanocomposite. Black spherical Sn nanoparticles are surrounded by flexible and curly graphene nanosheets (distinguishable as linear strips). A lattice resolved HRTEM image of the Sn nanoparticles and graphene nanosheets is presented in **Fig. 4-3(d)**. The stacking of graphene nanosheets is about 2–4 layers with a (0 0 2) interplanar distance of 0.38 nm, which is significantly larger than that in pristine graphite (0.34 nm). The inset in **Fig. 4-3(d)** shows a lattice image of Sn nanoparticles, in which the (2 0 0) crystal planes

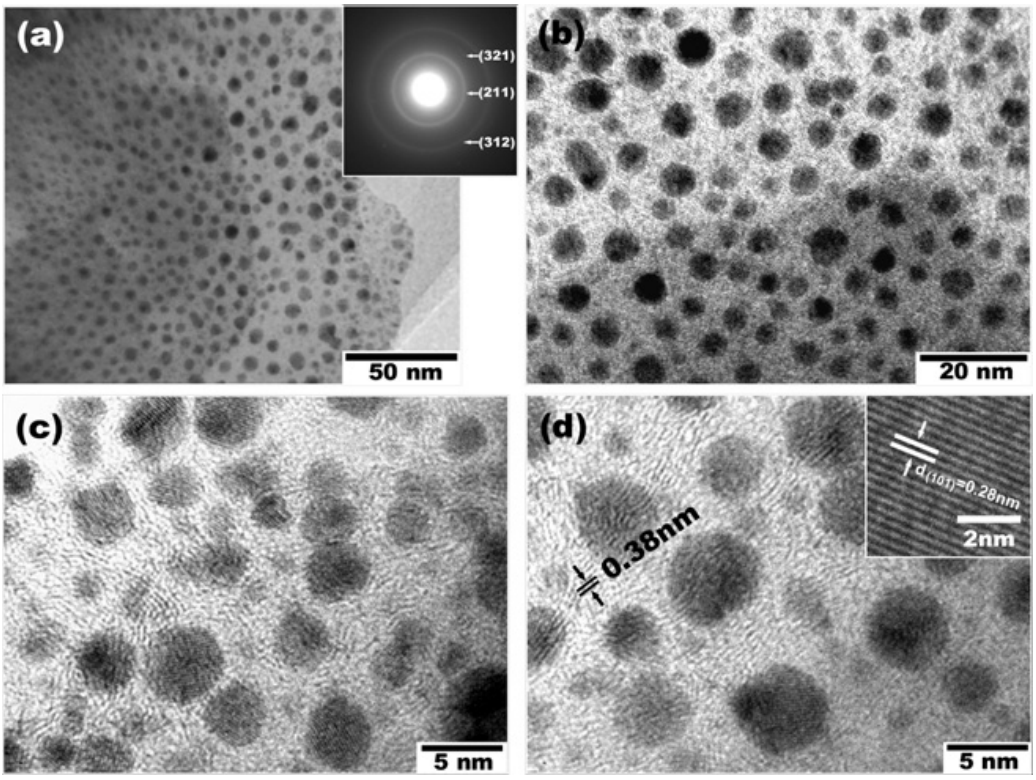

Fig. 4-3 (a) Low magnification TEM image of the Sn/GNS nanocomposite, showing the homogeneous distribution of the Sn nanoparticles on the graphene nanosheets. The inset is the SAED pattern. (b) High magnified TEM image of the Sn/GNS nanocomposite, from which the average particle size of Sn can be measured. (c) HRTEM image of the Sn/GNS nanocomposite, showing that the Sn nanoparticles are surrounded by wavy strips of graphene nanosheets. (d) Lattice resolved HRTEM image of Sn/GNS. The inset contains the lattice image of a Sn nanoparticle.

of the Sn tetragonal structure can be identified with an interplanar distance of 0.291 nm. Thus, FE-SEM, TEM and HRTEM analysis clearly elucidate the 3D architecture of the Sn/GNS nanocomposite.

Fig. 4-4 shows a zoomed AFM image of graphene sheets anchored with Sn nanoparticles. The line scan profile is shown at the bottom in **Fig. 4-4**. The peak marked in the profile corresponds to the height of Sn nanoparticle on graphene sheet (about 3 nm). The stacking of graphene sheets is clearly visible. The line scan transects across the edge of two stacked graphene flakes, from which the height of the top graphene sheet was measured to be about 1.6 nm. The results of AFM observation are consistent

with that of TEM analysis.

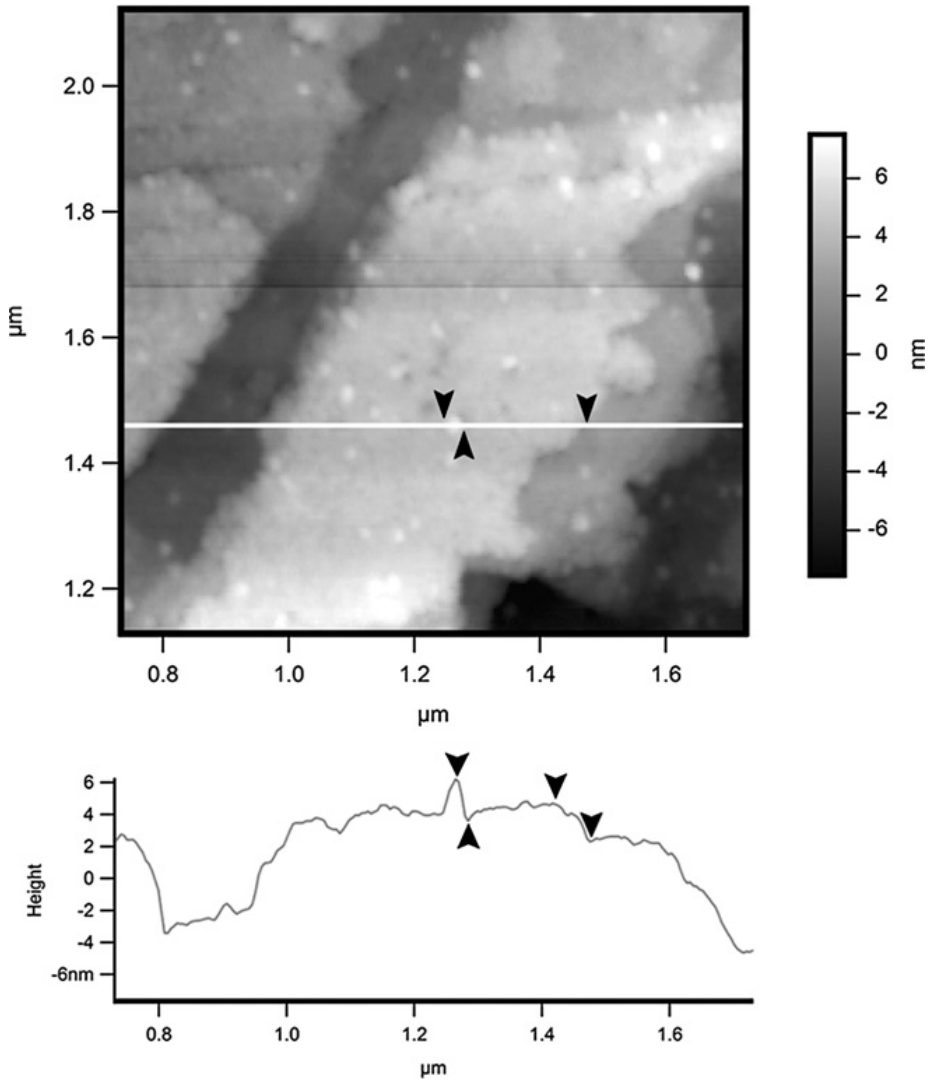

Fig. 4-4 AFM image of Sn nanoparticles anchored on graphene nanosheets. The line scan shows the peaks arising from Sn nanoparticles and the height of graphene at the edge of two pieces of stacked graphene sheets.

The electrochemical reactivity of the Sn/GNS nanocomposite as an anode material in lithium-ion cells was initially examined by CV. **Fig. 4-5(a)** presents the CV curves of a nanocomposite electrode in the 2nd, 5th, and 10th scanning cycles. The major lithium insertion potential is close to 0.1 V *vs.* Li/Li^+ reference electrode. Whereas, the potential for lithium extraction occur at 0.2 V, 0.55 V, 0.67, 0.76 V, and 0.82 V respectively,

which is associated with lithium extraction from graphene in the first step, and from Li_xSn alloys in the subsequent steps.[140] In addition, there is a small oxidation hump at

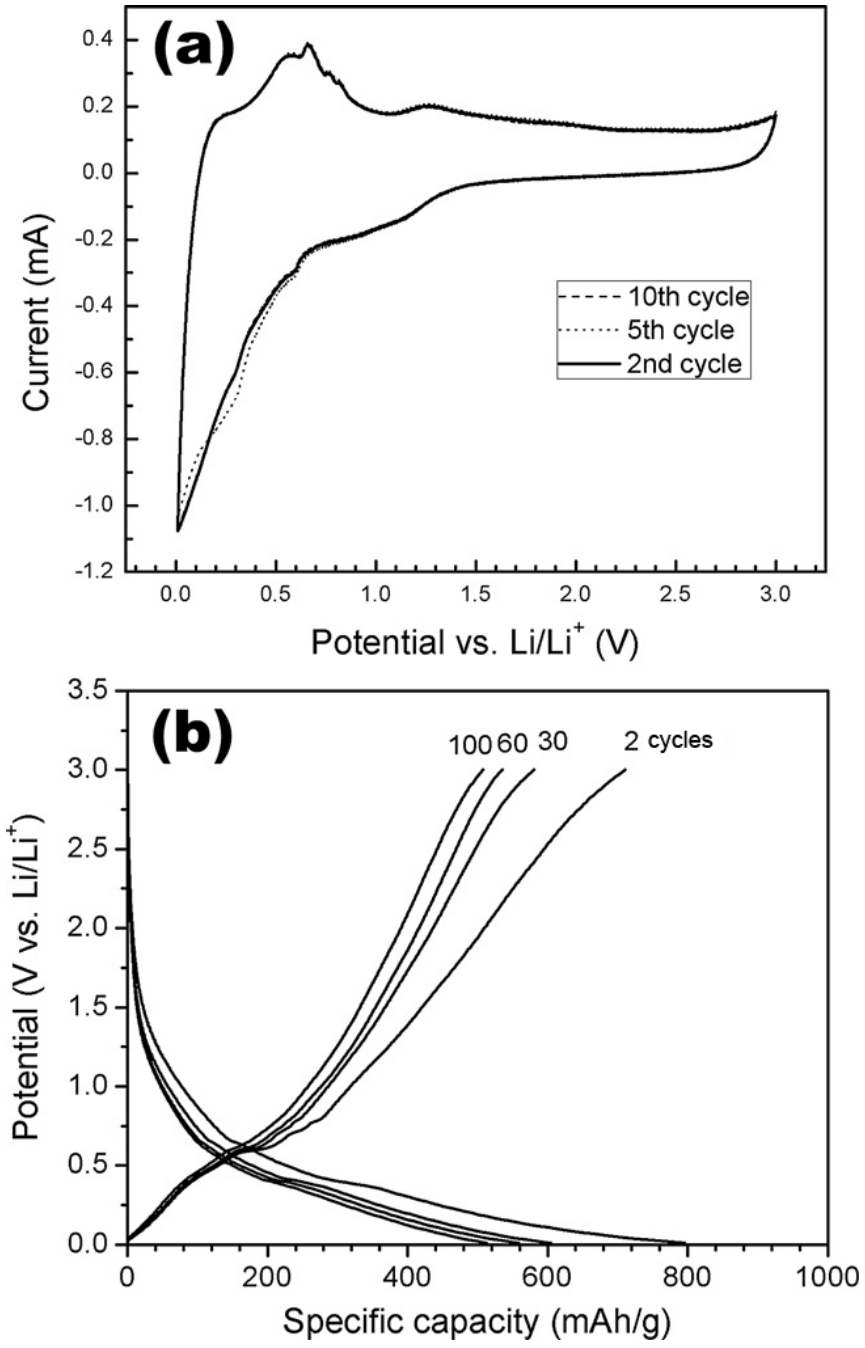

Fig. 4-5 (a) Cyclic voltammograms of the Sn/GNS electrode. (b) Charge/discharge profiles of Sn/GNS electrode in lithium-ion cells.

1.2 V, which could be related to a reversible lithium reaction with trace SnO_2 on the surface layer of Sn nanoparticles.[141] The CV measurement confirmed the reversible electrochemical reaction between lithium ions and Sn/GNS nanocomposite in lithium-ion cells. The specific capacity and cyclability of Sn/GNS nanocomposite electrodes were determined via constant current charge and discharge cycling at a current density of 55 mA g^{-1}. **Fig. 4-5(b)** shows the charge and discharge profiles in the 2nd, 30th, 60th, and 100th cycles respectively.

The lithium insertion capacity (discharge) of Sn/GNS nanocomposite electrode *vs.* cycle number is shown in **Fig. 4-6**. In the first cycle, the Sn/GNS electrode delivered a discharge capacity of 1250 mAh g^{-1} and a reversible charging capacity of 810 mAh g^{-1}. The irreversible capacity could be mainly ascribed to the formation of the solid electrolyte interphase (SEI) layers on the surface of the electrode. From the second cycle, the reversibility of the electrode was gradually improved on cycling, with an average columbic efficiency of 96.5%, up to 100 cycles. The electrode maintained a capacity of 508 mAh g^{-1} after 100 cycles. As a comparison, the cycling data of a bare graphene electrode and a microcrystalline Sn powder electrode are also presented in **Fig. 4-6**. The bare graphene electrode delivered a lithium storage capacity of 255 mAh g^{-1} after 100 cycles, which is comparable to the previously reported Sn-hollow carbon spheres and nanostructured Sn–C composites.[142, 143] The cycling performance of the bare Sn electrode is very poor. After 10 cycles, the bare Sn electrode failed. Thus, the Sn/GNS nanocomposite exhibited an optimized electrochemical performance compared to bare graphene and bare Sn powders.

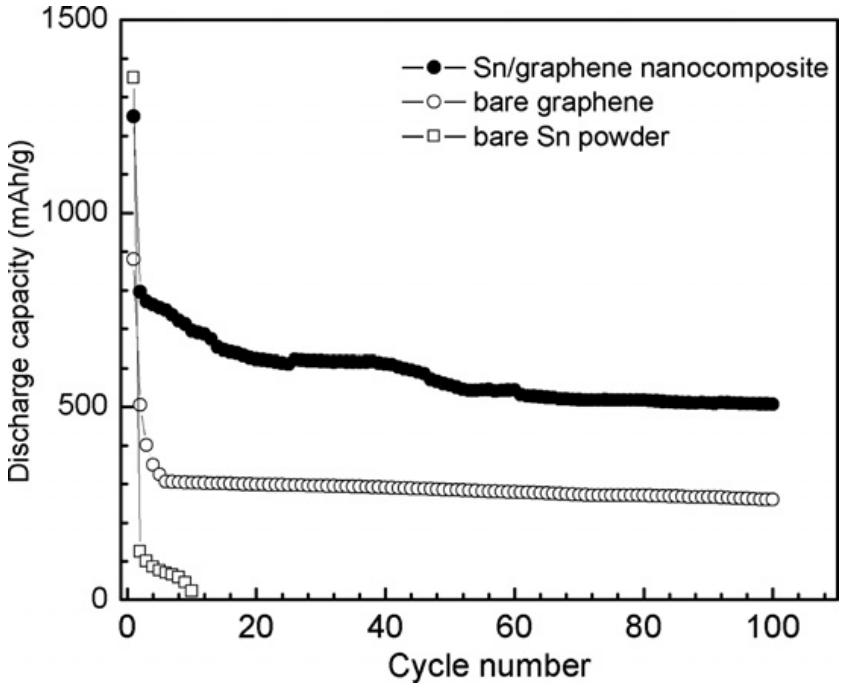

Fig. 4-6 Reversible lithium storage capacity vs. cycle number for Sn/GNS nanocomposite electrode, bare graphene electrode, and bare Sn electrode.

If all graphene nanosheets are strictly monolayer, the maximum lithium storage capacity of graphene is 744 mAh g^{-1}, corresponding to the formation of Li_3C. The Sn/GNS nanocomposite contains 35 wt% Sn. Therefore, the theoretical capacity of Sn/GNS nanocomposite can be calculated as:

$$\text{Total capacity} = C_{graphene} \times 65\% + C_{Sn} \times 35\% = 744 \times 0.65 + 994 \times 0.35 = 831.5 \text{ mAh } g^{-1} \quad \textbf{(Eq. 4-2)}$$

Although graphene nanosheets in the nanocomposite are not entirely monolayer (2–4 stacked layers, as observed by HRTEM and AFM), a reversible lithium storage capacity of 795 mAh g^{-1} has been achieved in the second cycle, which is comparable to the theoretical capacity. In addition, the voids existing in graphene nanosheets can effectively buffer the volume expansion of Sn (359%) when reacting with lithium. Consequently, cracking and pulverization of the electrode can be avoided, resulting in

an enhanced cycling stability. Further, graphene nanosheets provide a highly conductive matrix for electrons during the electrochemical reaction. Together, the small particle size of Sn (2–5 nm) and the cushioning effect of the graphene nanosheets facilitate maintenance of the integrity of the Sn/GNS electrode during long-term cycling.[126]

4.4 Conclusions

A synthetic approach has been designed to prepare a Sn/GNS nanocomposite with 3D architecture. FE-SEM, TEM, and AFM analysis revealed the homogeneous distribution of Sn nanoparticles (2–5 nm) on the graphene nanosheet matrix. CV measurements have proved the highly reversible nature of the reaction between Li^+ and the Sn/GNS nanocomposite. The 3D nano-architecture gives the Sn/GNS nanocomposite electrode high reversible lithium storage capacity (795 mAh g^{-1} in the second cycle and 508 mAh g^{-1} in the 100th cycle), which represents a much-improved performance compared to bare graphene electrodes and bare Sn electrodes. This enhanced electrochemical performance could be further improved by tuning the composition and structures of the nanocomposite.

Chapter Five

Mn_3O_4 Nanoparticles Embedded into Graphene Nanosheets: Preparation, Characterization, and Electrochemical Properties for Supercapacitors

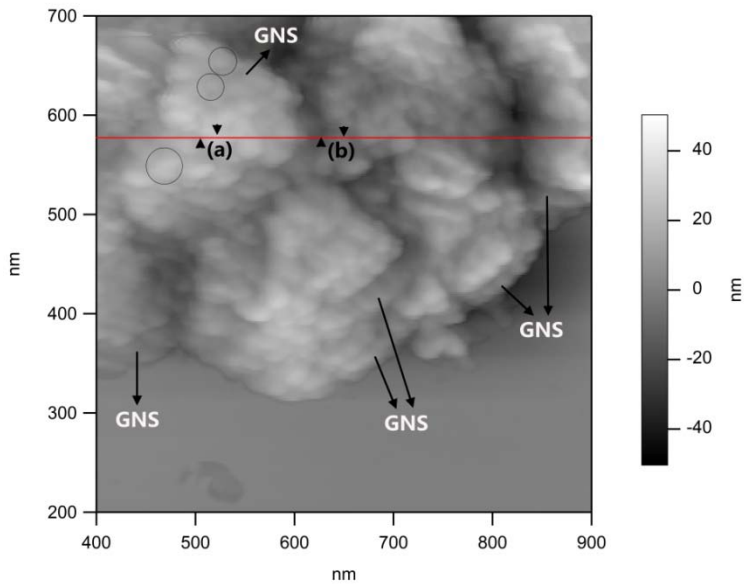

Chapter 5 — Mn_3O_4 Nanoparticles Embedded into Graphene Nanosheets: Preparation, Characterization, and Electrochemical Properties for Supercapacitors

5.1 Introduction

Mn_3O_4, of all the transition metal oxides, has attracted particular research interest, as it can be used in catalysis,[144-146] electrochromic applications,[147] and is also electrochemically active with a high-power nature when used in supercapacitors.[148] So far, Mn_3O_4/GNS has not been studied much. Therefore, Mn_3O_4 nanoparticles were chosen, in this project, to enhance the supercapacitance of graphene nanosheets. Mn_3O_4/GNS nanocomposite consists of graphene nanosheets jammed with Mn_3O_4 nanoparticles. The advantages of such composite materials can be found in two aspects. Firstly, compared to standard porous carbons or carbon nanotubes, graphene nanosheets have larger specific surface area, better electrochemical properties, a better organized 2D nanostructure, and a more flexible carbon matrix, which makes graphene applicable to multiple functions. Furthermore, there is no need to create pores, instead, metal oxide nanoparticles are introduced to stabilize graphene from aggregation and increase the accessible surface area. Secondly, transition metal oxide nanoparticles can effectively increase the supercapacitance due to their contribution to pseudocapacitance. The synthesis and supercapacitance of Mn_3O_4/GNS nanocomposites based on the preparation of MnO_2 organosol is reported in this chapter. The MnO_2 organosol is stable for a few months, and graphene was reassembled with surrounding MnO_2 particles. The product was then sintered to obtain crystallized Mn_3O_4 particles.

5.2 Experimental

5.2.1 Material Synthesis

The synthesis of graphene was derived from the modified Hummers method reported in a previous study,[35] in which GONS was first prepared and then reduced to yield graphene nanosheets by the use of hydrazine hydrate. The dried graphene was then re-dispersed in ethylene glycol by ultrasonication for 2 h with an ultrasonic probe to form a suspension at a concentration of 1 mg ml^{-1}. The preparation of MnO_2 organosol was performed as per the Jana et al. method.[149] Briefly, 79 mg of $KMnO_4$ was initially dissolved in 50 ml of DI water, and 50 ml of toluene was introduced into the above solution. Two separated phases were formed: the aqueous phase was purple and lay at the bottom, while the organic phase was left colorless on the top. Then, 300 mg of tetraoctylammonium bromide (TOAB) was added to the organic phase. After vigorous shaking, the organic phase turned purple as MnO_4^- ions were shifted to the upper layer. At this stage, the aqueous phase was removed, and 50 mg of tetrabutylammonium borohydride ($TBABH_4$) was added to the organic phase. Upon vigorous stirring, the color of the organic solution gradually became brown, indicating the evolution of MnO_2 particles. Ten ml of the brown organosol was taken and mixed with 35 ml of graphene suspension (1 mg ml^{-1}) in ethylene glycol. The mixture was ultrasonicated for 1 h, and 10 ml of DI water was then introduced. This mixture underwent ultrasonication again for 1 h. The resulting precipitate was isolated by filtration with a filter membrane (pore size: 0.22 μm) and washed with copious DI water and ethanol. After being dried under vacuum at 60 °C for 12 h, the product was further sintered at 450 °C under argon atmosphere for 5 h.

The mechanism behind the preparation of MnO_2 organosol is detailed in Ref.[149]. TOAB acts as a phase-transfer agent, causing MnO_4^- to move from the aqueous phase to the organic layer due to the formation of ion pairs $[TOA]^+[MnO_4]^-$. After the stable MnO_2 organosol was obtained, the graphene suspension was mixed with the toluene layer upon ultrasonication. DI water was introduced into the mixture of graphene suspension and MnO_2 organosol to ensure the sufficient precipitation of MnO_2 nanoparticles and graphene nanosheets. The capped MnO_2 particles precipitated gradually with graphene in the aqueous layer as the charge balance was destroyed and $[TOA]^+$ ions were no longer adsorbed on the surface of the MnO_2 nanoparticles to stabilize them by surface charges. The precipitate consisted of graphene nanosheets and MnO_2 nanoparticles capped by $[TOA]^+$ ions. On encountering heat treatment, MnO_2 was decomposed to Mn_3O_4, and TOAB was removed from the product by thermal decomposition. As a consequence, Mn_3O_4 nanoparticles were embedded into the graphene layers.

5.2.2 Material Characterization

A XRD pattern of the as-synthesized material was obtained using a GBC MMA X-ray diffractometer with Cu Kα radiation. FE-SEM images were captured with a JEOL JSM-7500FA FESEM instrument and the sample loaded on a carbon tape. TEM was utilized to provide crystal analysis via a JEOL 2011 TEM facility. AFM images were collected under tapping mode with a MFP-3D Stand Alone (MFP-3D-SA) AFM manufactured by Asylum Research with SuperSharpSilicon – Non-Contact/Tapping mode – High Resonance Frequency – Reflex Coating (SSS-NCHR) AFM tips for enhanced resolution. The specific surface areas of both pure graphene and Mn_3O_4/GNS

nanocomposites were determined by the gas adsorption technique using a Quanta Chrome Nova 1000 Gas Sorption Analyzer based on the BET method. To further confirm the presence of functional groups attached to graphene nanosheets, elemental analysis was performed on a Perkin Elmer 2400 Elemental Analyzer via the combustion of graphene samples (graphene nanosheets vacuum dried at 60 °C and sintered at 450 °C under argon atmosphere).

5.2.3 Electrochemical Testing

The electrochemical properties of the as-prepared material were examined by the CV technique on an electrochemistry workstation (CHI660C). Beaker-type three-electrode cells were assembled with a working electrode, a counter electrode (platinum foil), and a reference electrode (saturated calomel electrode, SCE) immersed in 1 M Na_2SO_4 and 6 M KOH electrolytes, respectively. The working electrode was prepared by mixing 90.2 wt% of Mn_3O_4/GNS powders and 9.8 wt% of PVdF in the presence of NMP, and this slurry was pasted on platinum foils and then heat treated at 120 °C under vacuum overnight. CV measurement was performed over the potential range of −0.2 to 0.8 V in 1 M Na_2SO_4 and −0.5 to 0.5 V in 6 M KOH, at the scan rates of 5 mV s^{-1}, 10 mV s^{-1}, 20 mV s^{-1}, and 50 mV s^{-1}, respectively. As a comparison, the electrochemical performance of pure graphene nanosheets was also investigated under the same conditions.

5.3 Results and Discussion

As shown in **Fig. 5-1(a)**, the XRD pattern of the dried precipitate exhibited only broad graphene peaks without any other well-defined diffraction lines of manganese oxide. nanoparticles because of a TOAB capping effect.[149] However, after heat treatment,

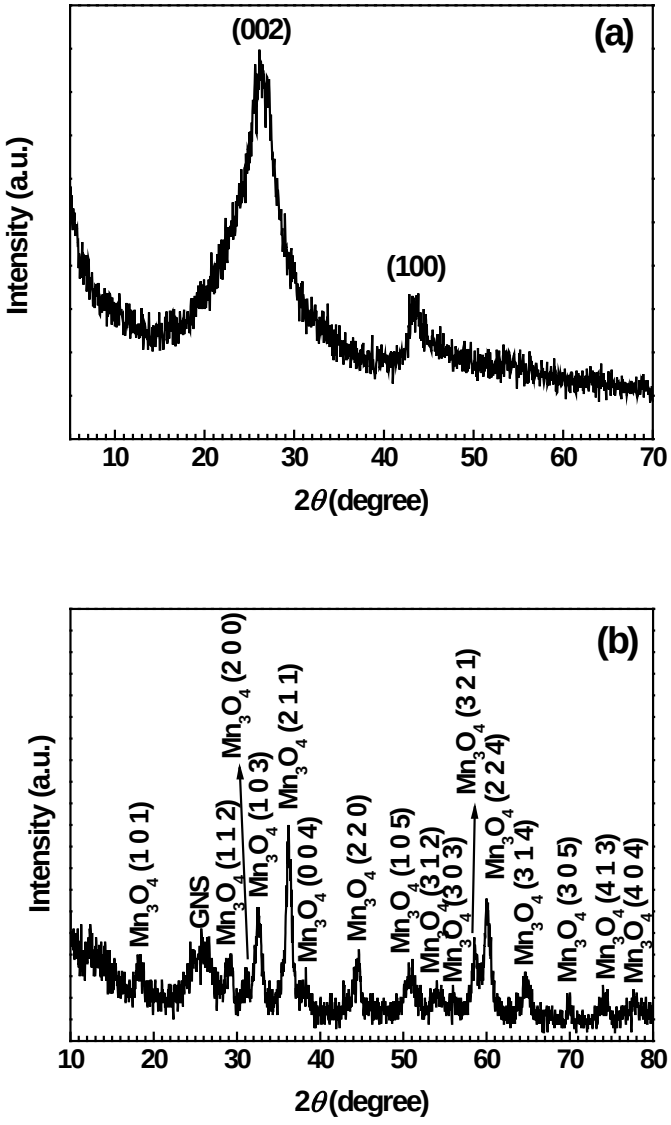

Fig. 5-1 X-ray diffraction patterns (a) vacuum dried graphene nanosheets, and (b) Mn_3O_4/GNS nanocomposites showing the diffraction lines of Hausmannite Mn_3O_4 and graphene nanosheets.

the as-synthesized product displayed typical Hausmannite Mn_3O_4 diffraction lines (**Fig. 5-1(b)**), in agreement with JCPDS card 80-0382. The peak found at around 26° (2θ) was indexed to the graphitic planes (0 0 2) of GNS. **Fig. 5-2** illustrates the morphology of the as-prepared nanocomposites from FE-SEM observations. **Fig. 5-2(a)**

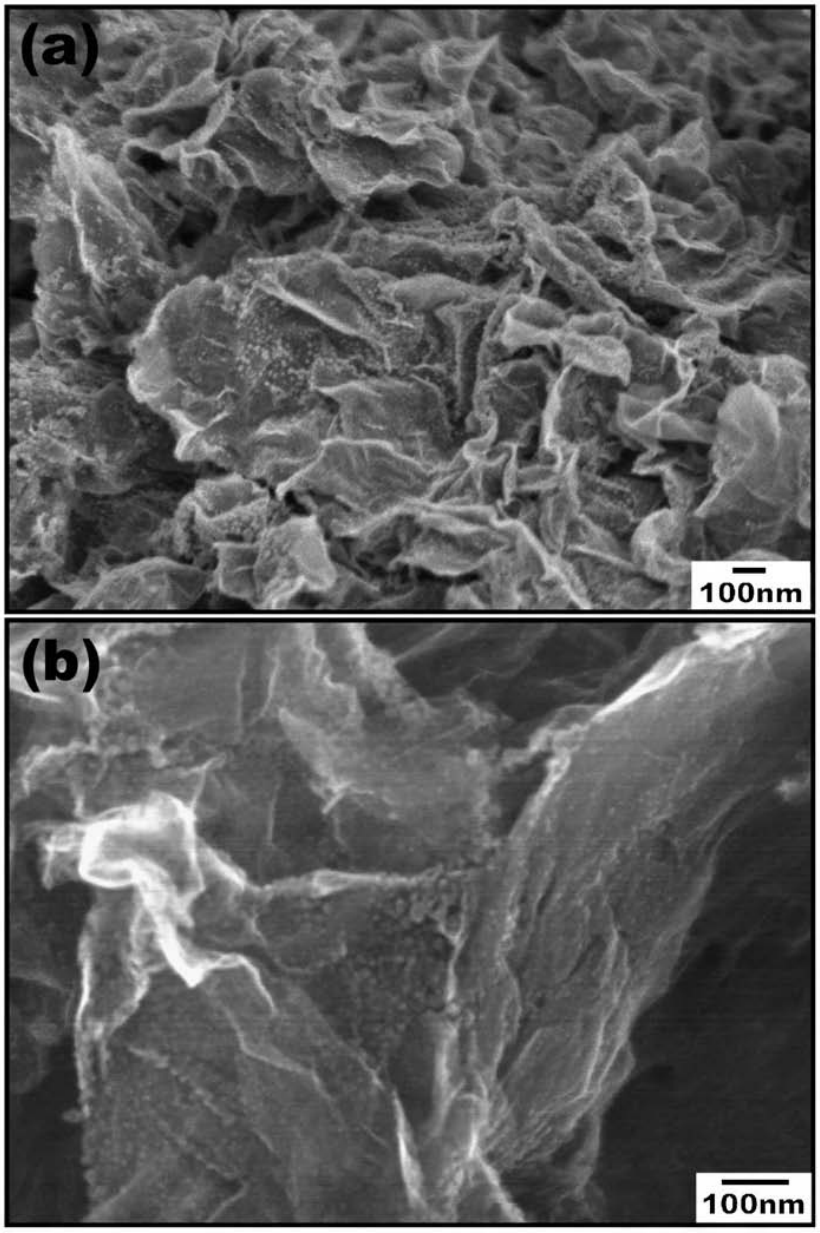

Fig. 5-2 FE-SEM images of the as-prepared Mn_3O_4/GNS nanocomposites: (a) low magnification image, showing the general morphology of graphene nanosheets with embedded Mn_3O_4 nanoparticles and (b) high magnification image, illustrating Mn_3O_4 nanoparticles on graphene nanosheets.

shows a low magnification FE-SEM image. It can be seen that graphene nanosheets were curly and well separated, with a large amount of Mn_3O_4 nanoparticles distributed on their layers. These particles were densely and homogeneously deposited. A high magnification FE-SEM image is shown in **Fig. 5-2(b)**, clearly illustrating Mn_3O_4 nanoparticles on graphene nanosheets.

Fig. 5-3(a) shows a low magnification TEM image of the as-prepared Mn_3O_4/GNS nanocomposites. Graphene nanosheets were corrugated and curly, and had the same morphology as observed in FE-SEM. TEM observation also identified that Mn_3O_4 nanoparticles were uniformly distributed on the surface of graphene nanosheets. The inset in **Fig. 5-3(a)** presents the corresponding SAED pattern, and the visible diffraction rings can be indexed to graphitic carbon (0 0 2) planes and Hausmannite Mn_3O_4 phase, (1 0 3), (2 1 1), (2 2 0) crystal planes. The *d*-spacing of the graphitic planes (0 0 2) was 0.376 nm, a little larger than the value for pristine graphite, as the interplanar distance was enlarged by chemical modification in the synthesis process. HRTEM (**Fig. 5-3(b)**) was focused on a few Mn_3O_4 nanoparticles and yielded their lattice information. The (1 0 1) and (2 1 1) crystal planes of Mn_3O_4 lattice can be clearly identified from the *d*-spacing of 0.49 nm and 0.25 nm, respectively. The particle size of Mn_3O_4 was determined to be around 10 nm, which is in consistent with that of FE-SEM observation.

An AFM image within a 500 nm by 500 nm area is shown in **Fig. 5-4** (top). Height differences are clearly distinguishable on the surface of the nanocomposite material. Combined with the scale bar, some flat areas can be discovered, which are different from the background and can be identified as graphene nanosheets (as indicated by arrows). Some spherical fragments can also be found on these flat areas at a relatively

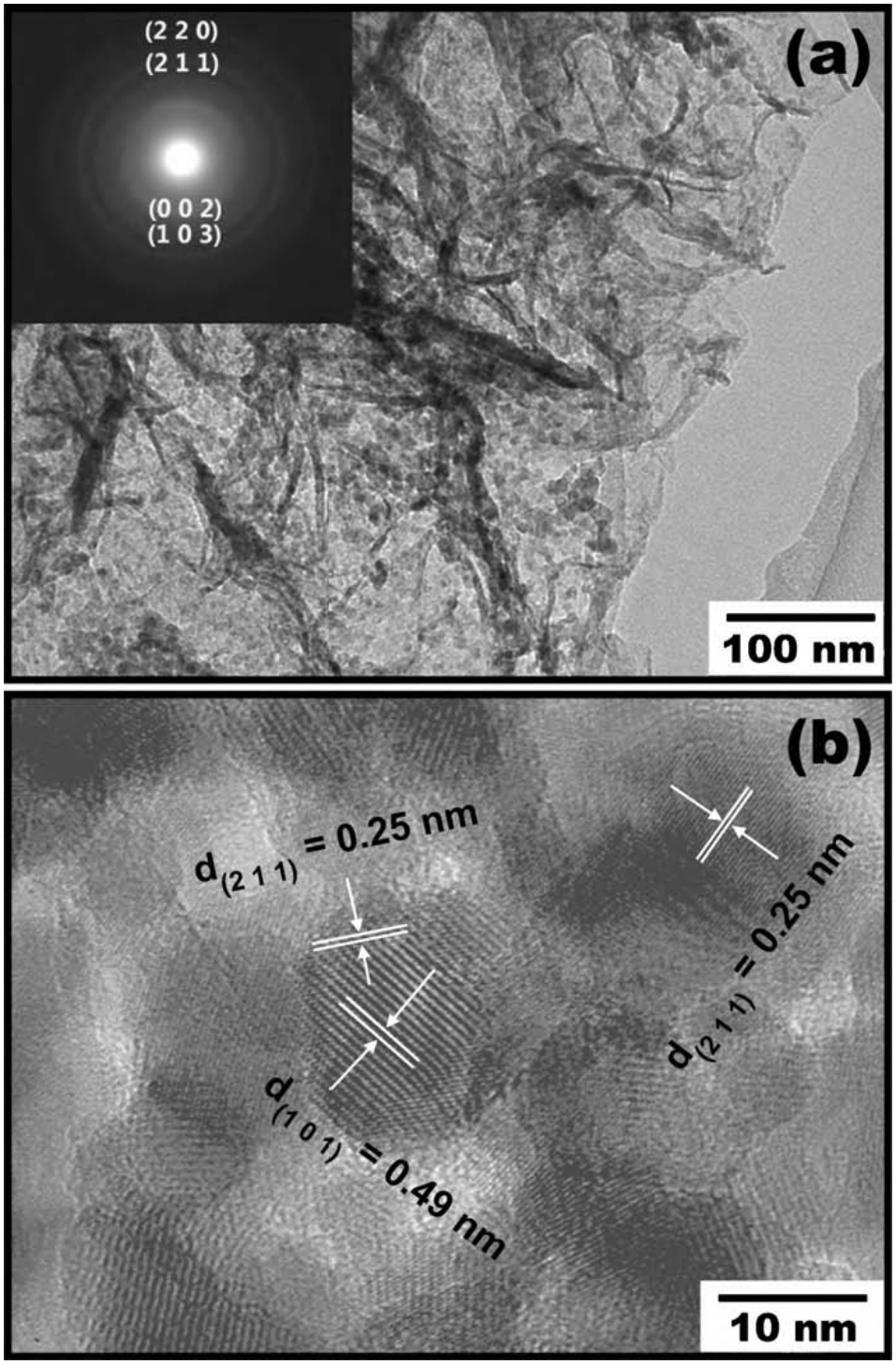

Fig. 5-3 TEM images of the as-prepared Mn_3O_4/GNS nanocomposites: (a) a low magnification TEM image showing dense Mn_3O_4 nanoparticles deposited on a large area of graphene nanosheets and the SAED pattern (inset) displaying graphene (0 0 2) and Mn_3O_4 (1 0 3), (2 1 1), and (2 2 0) diffraction rings; (b) an HRTEM image illustrating the *d*-spacing of Mn_3O_4 nanoparticles, which were evaluated to be around 10 nm in size.

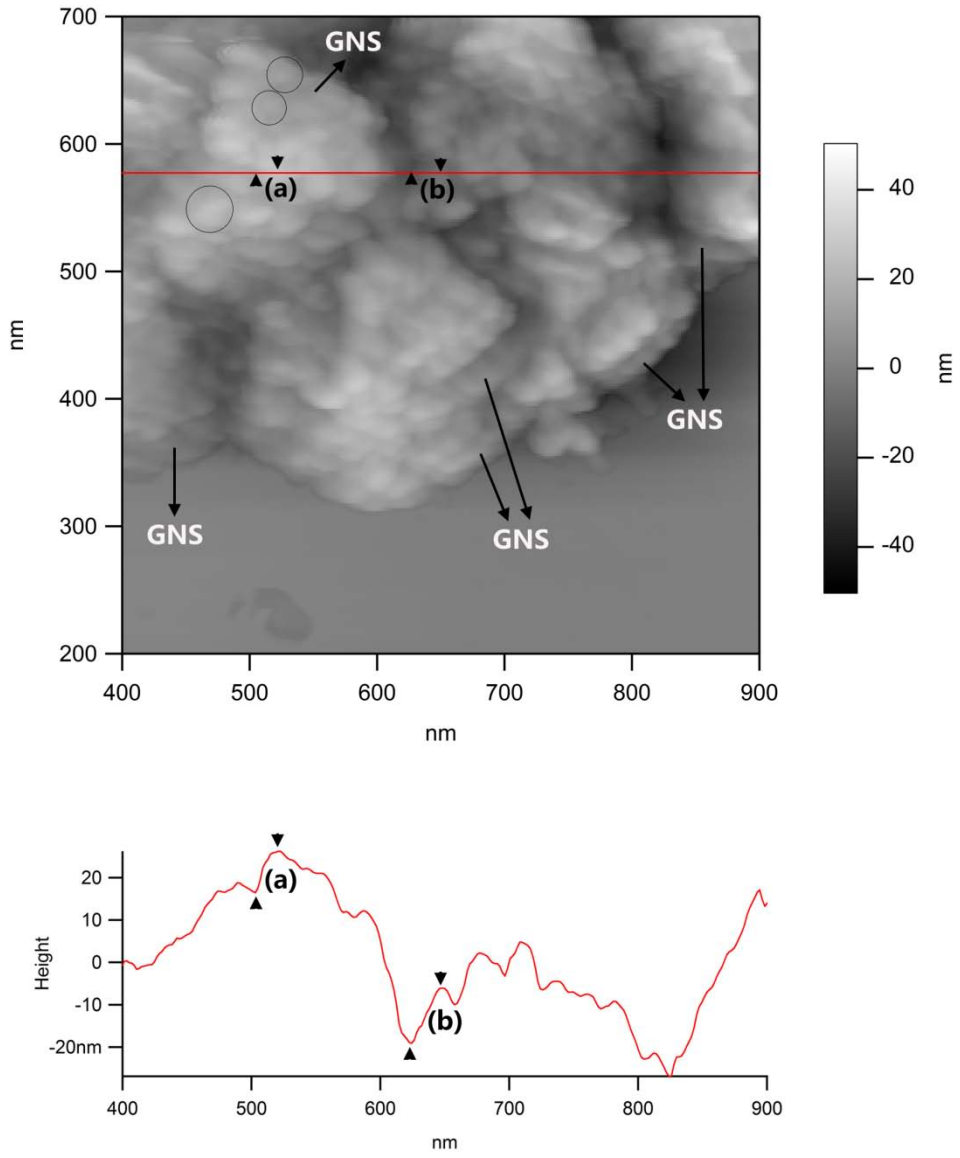

Fig. 5-4 AFM images of the as-prepared Mn_3O_4/GNS nanocomposites: (top) an image taken in a scan area of 500 nm by 500 nm, displaying graphene nanosheets (indicated by arrows) with embedded Mn_3O_4 nanoparticles (indicated by circles); (bottom) height profile across the examined area, as indicated by the red line, from which the particle size was determined to be 9.7 nm and 12.6 nm for particles (a) and (b), respectively.

higher level and can be identified as Mn_3O_4 nanoparticles (highlighted by circles). Graphene nanosheets are stacked (~5 nm thick) with Mn_3O_4 nanoparticles in between from the top view; Mn_3O_4 nanoparticles appear to be deposited on the surface of each graphene nanosheet. Indeed, graphene nanosheets are stabilized by Mn_3O_4 nanoparticles to form the type of "sandwich" architecture described in the previous chapter.[125] The

bright Mn_3O_4 nanoparticles are blurry and distorted, and some of them appear larger than they actually are, due to the resolution limit of the AFM tips within a nanoscale range. The particle size can be determined by the height differences of the desired particles on the height profile (**Fig. 5-4** (bottom)). Along the red line across the area, the particle sizes were 9.7 nm and 12.6 nm for particles (a) and (b), respectively, consistent with the results obtained from TEM analysis (~10 nm). BET surface area measurements were also performed on pure graphene nanosheets and Mn_3O_4/GNS nanocomposites by N_2 adsorption. The pure graphene nanosheets have a specific BET surface area of 93.7 $m^2\ g^{-1}$, while Mn_3O_4/GNS nanocomposites have a BET area of 1327.3 $m^2\ g^{-1}$, an increase of more than 14 times. This clearly proves that Mn_3O_4 nanoparticles can effectively reduce the stacking of graphene nanosheets.

CV was used to measure the specific capacitance of pure graphene and Mn_3O_4/GNS nanocomposite electrodes. The two electrolytes, 1 M Na_2SO_4 and 6 M KOH, were chosen on the basis of previous reports of nanocrystalline Mn_3O_4[148] and graphene nanosheets[44] in supercapacitor applications. **Fig. 5-5(a) and (b)** show the CV curves of graphene nanosheet electrodes in 1 M Na_2SO_4 electrolyte and 6 M KOH electrolyte, respectively. Neither of these two CV curves are perfect rectangles, in contrast to those reported by Ruoff and co-workers.[44] This unusual behaviour in shape, and the existence of redox peaks, might be attributable to the effects of epoxyl, hydroxyl, and carboxyl functional groups, which came from the chemical synthesis process used in this chapter.[27, 137] To test this possibility, elemental analyses of graphene nanosheets were undertaken. **Table 1** shows the elemental analyses for graphene nanosheets vacuum dried at 60 °C (denoted as GNS-60) and sintered at 450 °C under argon atmosphere (denoted as GNS-450), respectively.

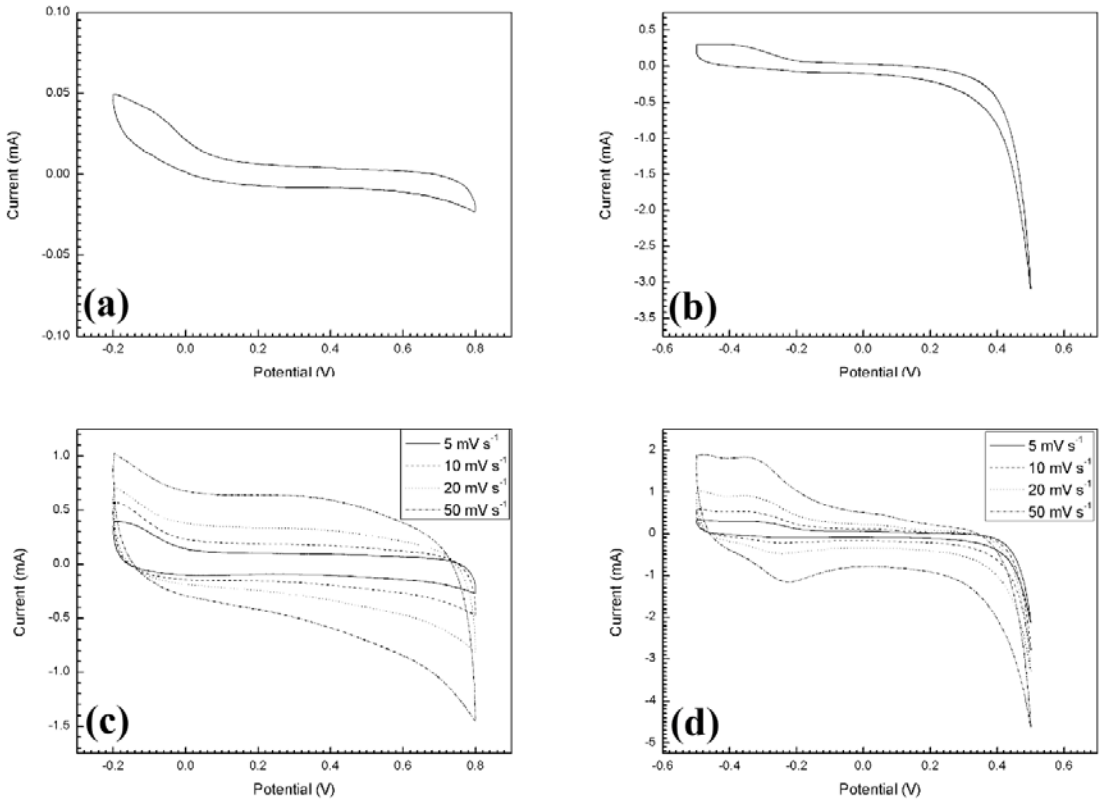

Fig. 5-5 CV curves of dried graphene nanosheets at a 5 mV s^{-1} scan rate in (a) 1 M Na_2SO_4 and (b) 6 M KOH, and CV curves of Mn_3O_4/GNS nanocomposite powders at scan rates of 5 mV s^{-1}, 10 mV s^{-1}, 20 mV s^{-1}, and 50 mV s^{-1} in (c) 1 M Na_2SO_4 and (d) 6 M KOH.

Table 5-1 Elemental analysis for GNS-60 and GNS-450 (wt%)

	C	H	N	O
GNS-60	80.57	0.13	2.93	16.37
GNS-450	82.89	0.11	2.69	14.31

GNS-60: graphene nanosheets vacuum dried at 60 ºC

GNS-450: graphene nanosheets sintered at 450 ºC under argon atmosphere

The results of the elemental analysis clearly demonstrate that graphene nanosheets contain 80.57 wt% carbon, 16.37 wt% oxygen, 2.93 wt% nitrogen and 0.13 wt% hydrogen. The presence of functional groups is confirmed by the high weight percentage of oxygen. Even after heat treatment, the graphene nanosheets still contain O, N and H elements (O: 14.31 wt%; N: 2.69 wt%; H: 0.11 wt%), indicating the retention of functional groups in the graphene samples. These results suggest that after heat treatment, functional groups exist in the graphene nanosheets in Mn_3O_4/GNS nanocomposites, contributing to pseudocapacitance. Therefore, the CV curves do not show a rectangle shape.

The values of specific capacitance achieved when using graphene electrodes were 17 F g^{-1} in 1 M Na_2SO_4 and 159 F g^{-1} in 6 M KOH at 5 mV s^{-1}. The specific capacitance in 1 M Na_2SO_4 was relatively low, which could be attributed to the nature of the electrolyte (1 M Na_2SO_4). To obtain the maximum power performance for an electrochemical capacitor, the internal electrical resistance in the capacitor must be minimized. This can be achieved by maximizing the conductance of the electrolyte, which provides the basis for either double-layer capacitance or for the Faradaic processes associated with charge or discharge of pseudocapacitance. The ionic conductivity of Na^+ is lower than that of K^+. So, the ionic conductivity of a 1 M Na_2SO_4 electrolyte is much lower than that of a 6 M KOH electrolyte.[50] Another factor contributing to the relatively low specific capacitance observed in 1 M Na_2SO_4 could be that the functional groups attached to graphene nanosheets are more chemically active in alkali electrolytes where redox reactions occur. This is evidenced by the shapes of CV curves (see **Fig. 5-5(b)**). In 1 M Na_2SO_4 electrolyte, the capacitance mainly originates from double layer capacitance; whereas in 6 M KOH electrolyte, redox peaks are clearly visible, indicating the participation of functional groups in electrochemical

activities and the additional contribution of pseudocapacitance. These effects could induce relatively low capacitance for graphene nanosheets in 1 M Na_2SO_4 electrolyte and high specific capacitance in 6 M KOH.

Ruoff's group first reported use of graphene as supercapacitor electrodes and they claimed the specific capacitance of chemically modified graphene to be 135 F g^{-1} in aqueous 5.5 M KOH electrolyte and 99 F g^{-1} in organic electrolyte, respectively.[44] The CV curves of their graphene electrodes were perfect rectangles in shape in both aqueous and organic solutions, which implied that no functional groups were attached to their graphene nanosheets. However, graphene nanosheets often contain epoxyl, hydroxyl, and carboxyl functional groups and defects from the chemical synthesis process,[137] and, as discussed above, in this project the as-prepared graphene still contains functional groups after heat treatment. The presence of these functional groups, in addition to causing CV curves with redox features that differ from the rectangular shaped curves obtained by Ruoff et al., may also contribute to the higher specific capacitance in 6 M KOH observed in this project compared to that observed by Ruoff et al.. The presence of small amounts of functional groups might provide pseudocapacitance to increase the overall capacitance.

The CV curves of Mn_3O_4/GNS nanocomposite powders are shown in **Fig. 5-5(c) and (d)**. In 1 M Na_2SO_4 electrolyte, all the curves at various scan rates featured the nearly ideal rectangular shape over the potential range (**Fig. 5-5(c)**). Both graphene and Mn_3O_4 nanoparticles could make electrochemical contributions to the specific capacitance. The Na^+ ions in the electrolyte were free to insert and de-insert themselves on the surface of the graphene sheets and also had access through the Mn_3O_4 nanoparticles. On the other hand, in 6 M KOH electrolyte, redox peaks were clearly observed when CV

measurement was performed for Mn_3O_4/GNS nanocomposite powders (**Fig. 5-5 (d)**). The peaks were caused by the functional groups attached to the graphene nanosheets. The highest specific capacitance was determined to be 175 F g^{-1} in 1 M Na_2SO_4 and 256 F g^{-1} in 6 M KOH at 5 mV s^{-1}. The supercapacitance of the nanocomposite was significantly increased, compared to that of pure graphene nanosheets. The significantly increased specific surface area of the nanocomposite material was thought to be the major reason for the enhanced capacitance. The electrochemical performances of graphene and Mn_3O_4/GNS nanocomposite electrodes are better in 6 M KOH than in 1 M Na_2SO_4. This can be accounted for by the nature of the two electrolytes. Compared to 1 M Na_2SO_4, 6 M KOH solution has more free charge carriers (6 M K^+ *vs.* 2 M Na^+) to minimize the internal resistance in the capacitor cell. As K^+ ions have higher mobility than Na^+ ions in aqueous solvents, the conductance of the capacitor cell will be improved.

The specific capacitances per surface area of graphene and Mn_3O_4/GNS nanocomposites are 0.181 F m^{-2} and 0.132 F m^{-2} in 1 M Na_2SO_4 electrolyte, and 1.69 F m^{-2} and 0.193 F m^{-2} in 6 M KOH electrolyte, respectively. The surface-related capacitance for graphene in 6 M KOH is quite high, compared to previously reported carbon materials with or without porosity. This enhancement could be ascribed to the functional groups attached to the surface of graphene nanosheets, contributing pseudocapacitance to the overall capacitance. Several research groups have recently reported this phenomenon. The specific capacitance of surface-functionalized carbons can be significantly improved owing to the surface functionalities.[150] For example, N-containing carbon–carbon nanotube (CNT) composites and O-enriched carbon materials have demonstrated specific capacitances of 0.75 F m^{-2} and 1 F m^{-2}, respectively.[151, 152] Hulicova et al. developed N-enriched carbon for supercapacitors,

which exhibited a specific capacitance of about 3 F m^{-2} in acidic and alkali electrolytes.[153, 154] Therefore, it is believed that the functional groups attached to graphene nanosheets could make contributions to the enhanced supercapacitance.

To further clarify the contributions of Mn_3O_4 nanoparticles and graphene nanosheets to the overall supercapacitance, a TGA was performed on the Mn_3O_4/GNS nanocomposite. It has been determined that the composites contain 88.56 wt% Mn_3O_4 nanoparticles and 11.44 wt% graphene. Therefore, the supercapacitance contribution of Mn_3O_4 nanoparticles in nanocomposites can be evaluated to be 195 F g^{-1} in 1 M Na_2SO_4 electrolyte and 268 F g^{-1} in 6 M KOH electrolyte, respectively.

In both electrolytes, Mn_3O_4 nanoparticles make two types of contributions. Firstly, the specific capacitance is increased due to the pseudocapacitance derived from the Mn_3O_4 nanoparticles, making an additional electrochemical contribution to the overall specific capacitance. Secondly, the significantly increased BET surface area of the Mn_3O_4/GNS nanocomposite over that of pure graphene naosheets should also contribute to the enhancement of supercapacitance. The extended interplanar space and accessible surface area allows the active ions (Na^+ and K^+) to intercalate and de-intercalate more easily and sufficiently. However, in addition to the contributions of the Mn_3O_4 nanoparticles, pseudocapacitance also benefits from the contribution of the functional groups attached to the graphene nanosheets. Therefore, the enhancement of specific capacitance of Mn_3O_4/GNS nanocomposite can be ascribed to both the electrochemical contributions of Mn_3O_4 nanoparticles, pseudocapacitance originated from functional groups attached to graphene nanosheets, and the increased specific surface area.

5.4 Conclusions

Mn_3O_4/GNS nanocomposite was synthesized via a chemical method based on the preparation of MnO_2 organosol. The as-prepared materials exhibited outstanding electrochemical properties as supercapacitor electrodes, because of the electrochemical activities of embedded Mn_3O_4 nanoparticles, functional groups attached to graphene nanosheets, and the activated graphene open network with its increased specific surface area and enlarged interlayer space. These Mn_3O_4 particles were ~10 nm in size, were densely distributed on graphene nanosheets, and played a crucial role in enhancing electrochemical performance. A high specific capacitance of 256 F g^{-1} was achieved for Mn_3O_4/GNS nanocomposites, which is almost double that of pure graphene nanosheets.

Chapter Six

In-situ Synthesis of Co_3O_4/Graphene Nanocomposite Material for Lithium-Ion Batteries and Supercapacitors with High Capacity and Supercapacitance

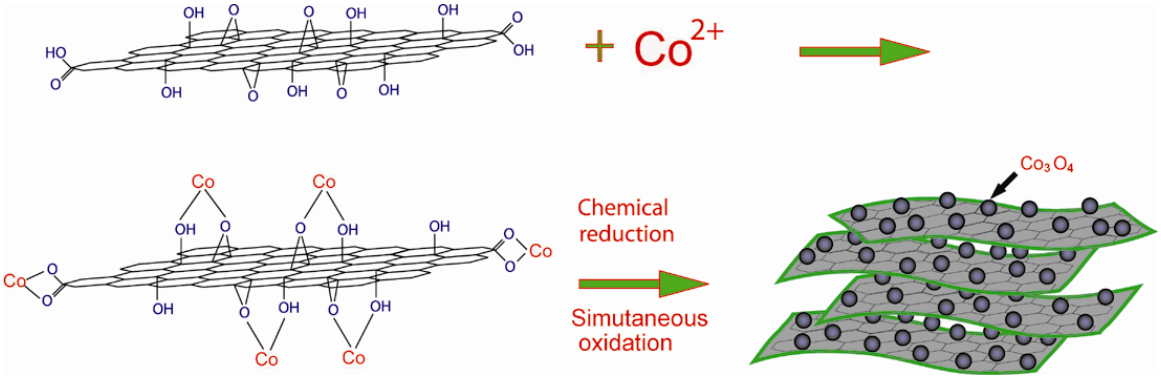

Chapter 6 — In-situ Synthesis of Co_3O_4/Graphene Nanocomposite Material for Lithium-Ion Batteries and Supercapacitors with High Capacity and Supercapacitance

6.1 Introduction

Among the reported transition metal oxides, cobalt (II, III) oxide (Co_3O_4) has delivered promising electrochemical performance as an anode material for lithium-ion batteries[155] and superior specific capacitance for supercapacitors.[156] The synthesis of nanocrystalline Co_3O_4 has been carried out using various methods to obtain nanosized Co_3O_4 of different architectures, such as nanotubes,[155] nanoparticles,[157] nanorods,[158] and hollowed spheres.[159] In the case of Co_3O_4/carbon nanotube (CNT), the nanocomposite was shown to have good electrical conductivity and extra electrochemical properties, which could be potentially applied to lithium-ion batteries[160] and supercapacitors.[161]

In comparison, graphene nanosheets have a larger specific surface area, a better organized 2D nanostructure, a more flexible carbon matrix and electrochemical properties superior to those of CNTs. Given this, this project aimed to prepare a Co_3O_4/GNS nanocomposite by introducing Co_3O_4 nanoparticles into graphene nanosheets. An in-situ synthesis of graphene anchored with Co_3O_4 nanoparticles in a basic aqueous solution has been previously reported by Wu et al..[162] With the transformation of $Co(OH)_2$ to Co_3O_4 by calcination, Co_3O_4/GNS was successfully obtained. In this chapter, a new synthetic approach that involves the reduction of Co^{2+} ions from the salt solution and air-oxidation to form Co_3O_4 nanoparticles in-situ of the graphene nanosheets, is reported. Also reported is the testing of the electrochemical performance of the Co_3O_4/GNS nanocomposite material and investigation of its

potential application as electrodes in lithium-ion batteries and supercapacitors. The individual roles and contributions of graphene and the embedded Co_3O_4 nanoparticles will also be discussed.

6.2 Experimental

6.2.1 Material Synthesis

GONS were prepared using a known modification of the Hummers method.[35, 36] Twenty ml of GONS aqueous dispersion (2 mg GONS in 1 ml of DI water) was then obtained by ultrasonication with an ultrasonic probe (Branson Digital Sonifier S450D, 500 W, 30% amplitude) for an hour. The GONS dispersion was diluted to 80 ml with DI water and mixed thoroughly with 20 ml of $CoCl_2$ aqueous solution (30 mg of $CoCl_2 \cdot 6H_2O$) under magnetic stirring. Graphene oxide nanosheets have carboxylic acid, epoxyl and hydroxyl functional groups on the edge and on the basal plane.[137] Therefore, individual graphene nanosheets are negatively charged.[163] Co^{2+} anions attracted and anchored on the basal planes and edges of GONS homogeneously. Twenty ml of freshly prepared 5 mg ml^{-1} $NaBH_4$ solution was added dropwise within 10 min to the above solution and the mixed solution was refluxed at 100 °C for 3 h. During this process, GONS were reduced to GNS and Co^{2+} anions to Co nanoparticles simultaneously. The mixture was refluxed at 100 °C in the air atmosphere; Co nanoparticles were oxidized to Co_3O_4 nanoparticles rapidly. The reaction mechanism is depicted in **Scheme 6-1** and detailed in Ref.[125] and Chapter 4. The resultant black precipitate was isolated by filtration, washed with DI water and ethanol three times each,

and dried under vacuum for 12 h. To increase crystallinity, the product was annealed at 200 °C under argon atmosphere for 15 h.

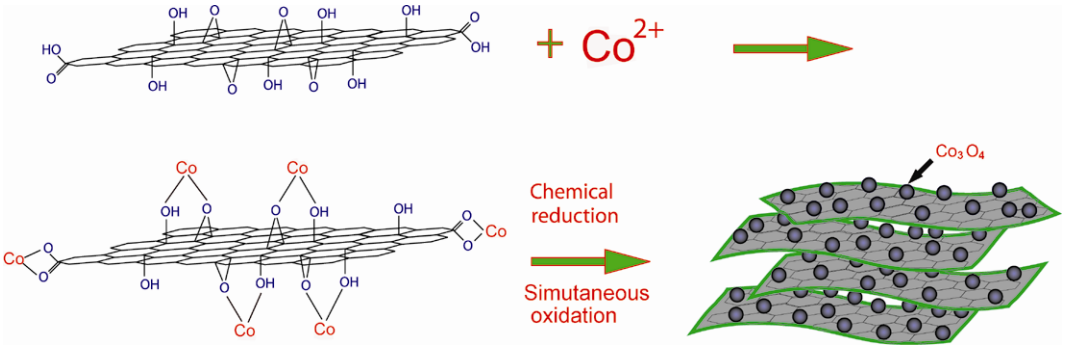

Scheme 6-1 Schematic of the reaction mechanism for the formation of Co_3O_4/GNS nanocomposite.

6.2.2 Material Characterization

The XRD pattern of the synthesized materials was measured using a GBC MMA X-ray diffractometer. The Raman spectrum was acquired on a Jobin Yvon HR800 confocal Raman system with 632.81 nm diode laser excitation on a 300 lines/mm grating at room temperature. FE-SEM observations were performed using a JEOL JSM-7500FA FE-SEM instrument with the sample loaded on a carbon tape. The TEM analysis was carried out using a JEOL 2011 TEM facility. AFM images were collected under tapping mode with a MFP-3D Stand Alone (MFD-3D-SA) AFM (manufactured by Asylum Research) with SuperSharpSilicon – Non-Contact/Tapping Mode – High Resonance Frequency – Reflex Coating (SSS-NCHR) AFM tips for enhanced resolution. The graphene (carbon) content in the composite material was determined by TGA on a Mettler Toledo TGA/DSC instrument in air at 10 °C min^{-1} at temperature range of 25–1000 °C. The specific surface area of the Co_3O_4/GNS nanocomposite was determined

by the gas sorption technique using a Quanta Chrome Nova 1000 Gas Sorption Analyzer based on the BET method.

6.2.3 Electrochemical Testing

Electrodes for electrochemical measurements were fabricated by mixing 89.9 wt% Co_3O_4/GNS powders and 10.1 wt% PVdF in the presence of NMP, and the resultant slurry mixture was pasted onto copper foils for lithium-ion cell testing and platinum foil substrates for supercapacitors, before being heated at 110 °C under vacuum overnight. For lithium-ion batteries, CR2032-type coin cells were assembled in a glove box for electrochemical characterization. The electrolyte was 1 M $LiPF_6$ in a 1:1 mixture of ethylene carbonate and dimethyl carbonate. Li metal foil was used as the counter electrode. The cells were galvanostatically charged and discharged at a current density of 55 mA g^{-1}, within the range of 0.01–3.0 V. CV curves were collected at 0.1 mV s^{-1} within the range of 0.01–3.0 V using an electrochemistry workstation (CHI660C). For supercapacitors, the electrochemical properties were examined by the CV technique using the CHI660C electrochemistry workstation. A beaker-type three-electrode cell was assembled with a working electrode, a counter electrode (platinum foil), and a reference electrode (SCE) immersed in 2 M KOH solution. CV was applied over the potential range of −0.25 to 0.55 V in 2 M KOH, at the scan rates of 5 mV s^{-1}, 10 mV s^{-1}, 20 mV s^{-1}, and 50 mV s^{-1}, respectively. For comparative studies, the electrochemical performances of nanosized commercial Co_3O_4 powders (<50 nm) and bare graphene nanosheets were investigated under the same conditions for lithium-ions batteries and supercapacitors.

6.3 Results and Discussion

Fig. 6-1(a) shows the XRD pattern of the prepared Co_3O_4/GNS nanocomposite material. Well-defined diffraction peaks at around 19°, 31°, 37°, 45°, 59°, and 65° are

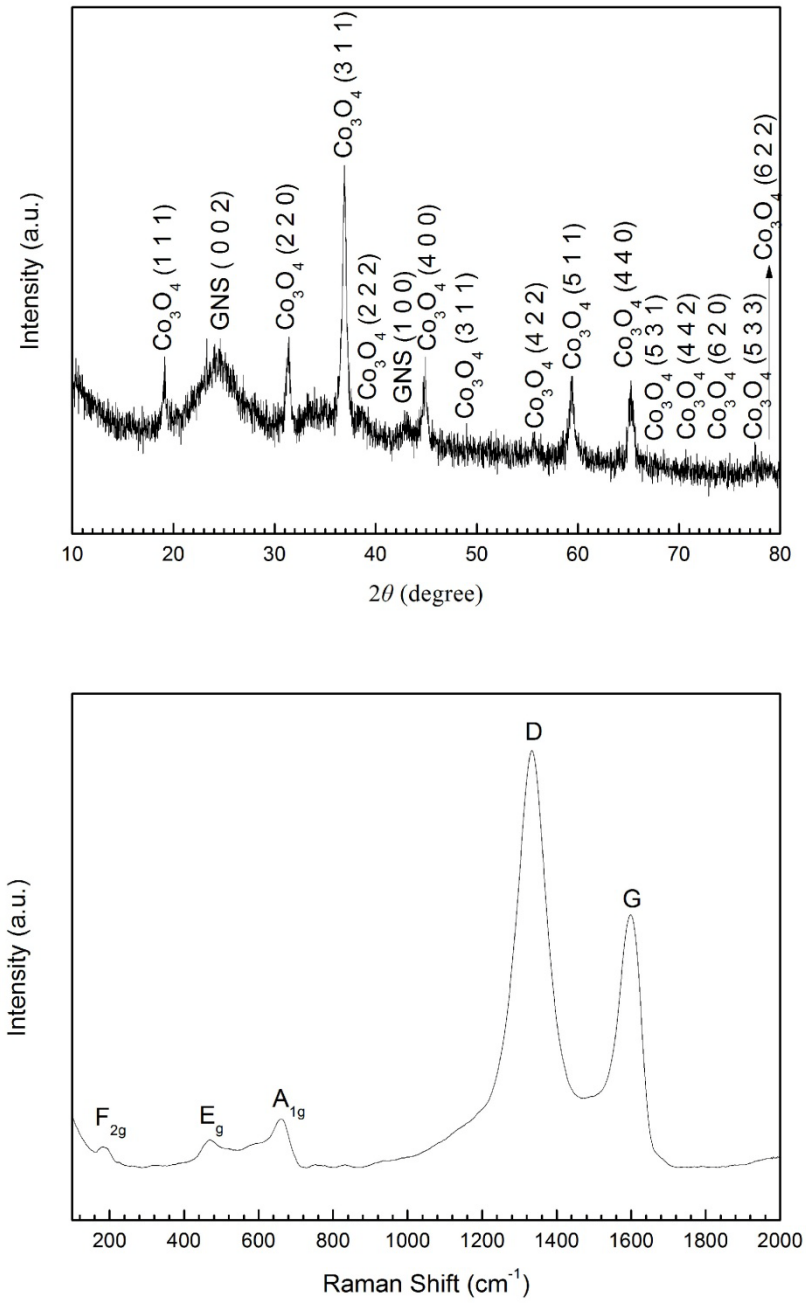

Fig. 6-1 (a) XRD pattern and (b) Raman spectrum of the as-prepared Co_3O_4/GNS nanocomposite material.

indicative of nanosized Co_3O_4, which is in good agreement with the JCPDS card 76-1802. The sharp diffraction peaks reflect the excellent crystallinity of the Co_3O_4 nanoparticles. Graphene nanosheets display a broad graphitic (0 0 2) peak and a weak (1 0 0) peak, as seen in the XRD patterns, implying breakage of the interplanar carbon bonds of the pristine graphite and formation of graphene nanosheets. In the Raman spectrum (**Fig. 6-1(b)**), two typical Raman peaks of carbon, the D line and G line, are observed at 1333 cm^{-1} and 1598 cm^{-1}, respectively. The D line is stronger than the G line, and the D/G intensity ratio in the spectrum is significantly larger than that of well-crystallized graphite, indicative of a decrease in the sp^2 carbon matrix compared with that of pristine graphite and the exfoliation of graphene layers.[27] As the intensity of the D line and the G line is quite high, only three other Raman peaks are clearly visible. These three peaks are located at 182 cm^{-1}, 470 cm^{-1}, and 658 cm^{-1}, respectively, and can be assigned to the F_{2g}, E_g, and A_{1g} active modes of the Co_3O_4 nanoparticles. The frequencies of these three Raman peaks are similar to that found in the standard microcrystalline Co_3O_4 powders.[164] As a comparison, **Fig. 6-2** shows the XRD pattern and the Raman spectrum of pure graphene nanosheets; these confirm the presence of graphene in the nanocomposite material.

The morphology of the nanocomposite material was observed by FE-SEM in general beam-high resolution (GB-HR) mode. The FE-SEM image **(Fig. 6-3(a)**) acquired at a low magnification exhibits numerous graphene nanosheets in curly and corrugated states. At a higher magnification (**Fig. 6-3(b)**), Co_3O_4 nanoparticles, with a size of ~20 nm, can be found distributed densely and homogeneously on the surfaces of graphene nanosheets. The insertion of Co_3O_4 nanoparticles between the interlayers of the graphene nanosheets (as shown in **Fig. 6-3(b)**) can also be observed, and this

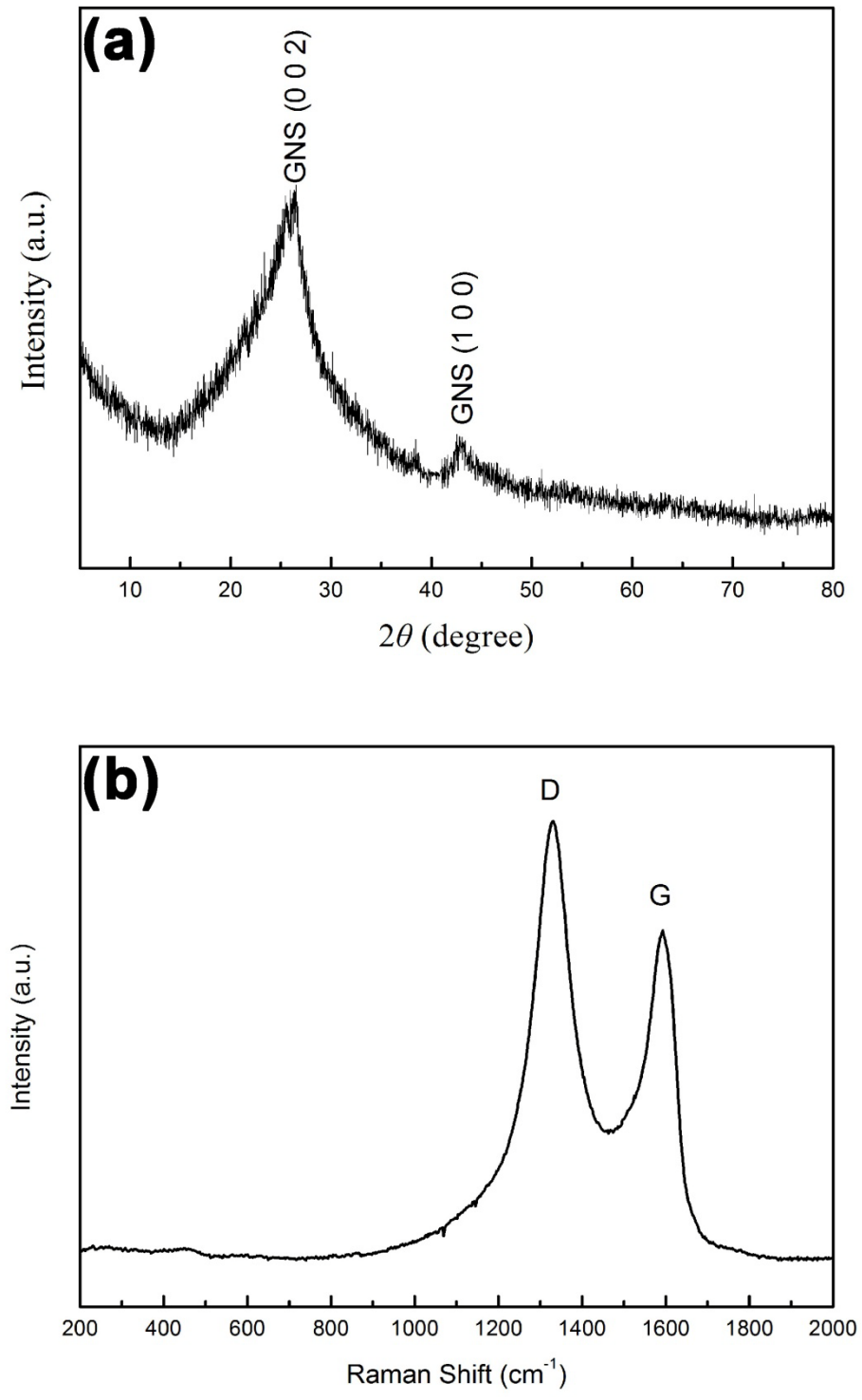

Fig. 6-2 (a) XRD and (b) Raman spectrum of pure graphene nanosheets.

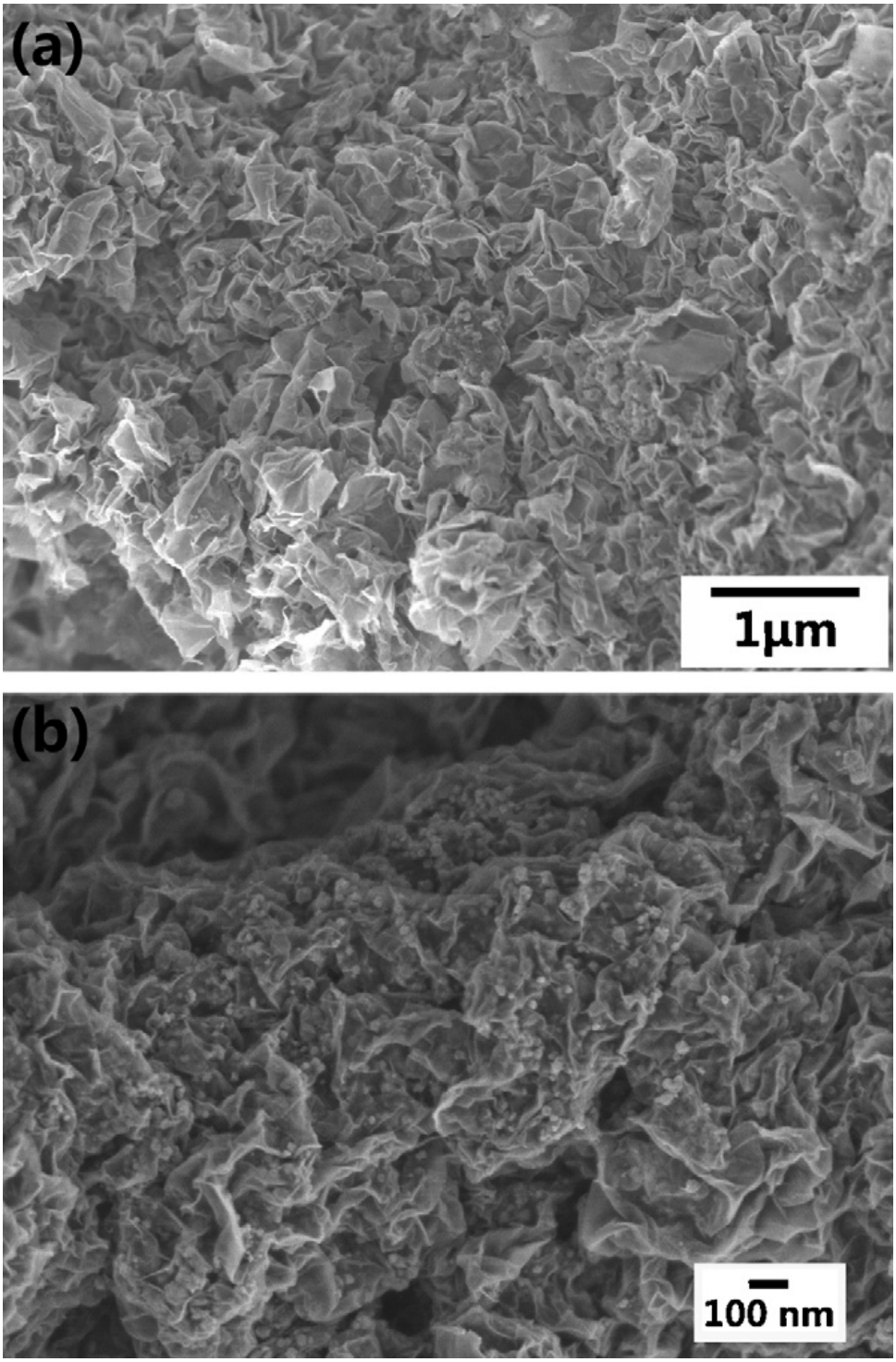

Fig. 6-3 FE-SEM images of the Co_3O_4/GNS nanocomposite obtained under GB-HR mode: (a) numerous curly graphene nanosheets observed at a low magnification, and (b) a higher magnification image, displaying the distribution of Co_3O_4 nanoparticles on graphene nanosheets. The embedded Co_3O_4 nanoparticles are ~20 nm in size.

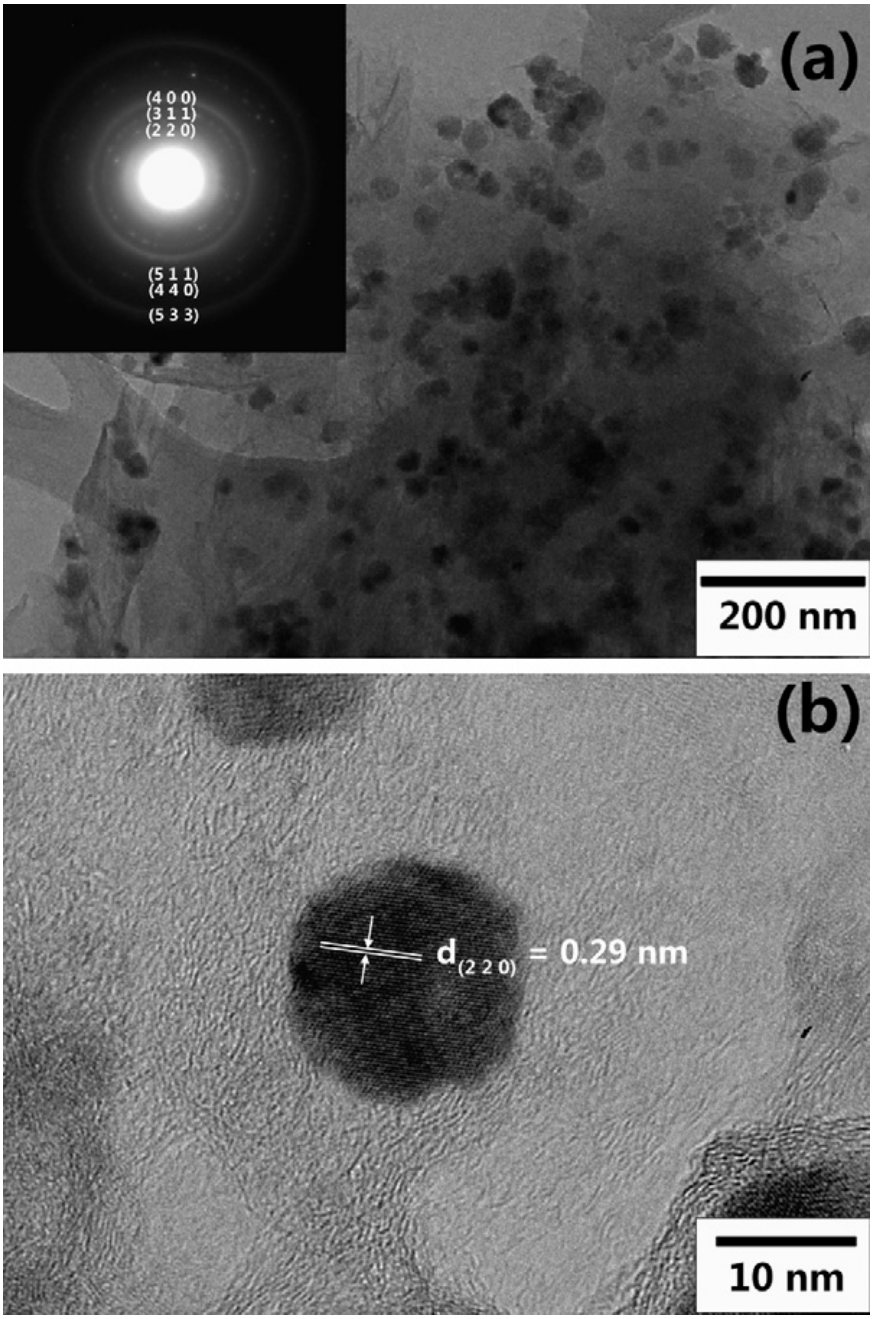

Fig. 6-4 TEM images of the Co_3O_4/GNS nanocomposite material: (a) a low magnification image showing Co_3O_4 nanoparticles dispersed on graphene nanosheets; (inset) the SAED pattern within this examined region; (b) an HRTEM image focusing on a single Co_3O_4 nanoparticle.

confirms the presence of the sandwich-like architecture of the composite. The crystal structure of the Co_3O_4/GNS nanocomposite material was further examined by TEM analysis. **Fig. 6-4(a)** shows a low magnification TEM image, in which Co_3O_4

nanoparticles are clearly visible and dispersed homogenously on the graphene nanosheets. As the graphene nanosheets are corrugated in nature, some regions appeared darker, and the Co_3O_4 nanoparticles therefore appeared to be very close to each other, however, were actually isolated by different layers of graphene nanosheets. The particle sizes of these Co_3O_4 nanoparticles were determined to be 15–25 nm, which is consistent with the results of FE-SEM observation. The inset in **Fig. 6-4(a)** shows a SAED pattern within this examined area. The diffraction rings from inside to outside indexed to (2 2 0), (3 1 1), (4 0 0), (5 1 1), (4 4 0), and (5 3 3) planes of Co_3O_4 nanoparticles, respectively. An HRTEM image focusing on a single Co_3O_4 nanoparticle is shown in **Fig. 6-4(b)**. Crystal fringes were clearly displayed, and the *d*-spacing of this Co_3O_4 nanoparticle was derived to be 0.29 nm, corresponding to the spacing between (2 2 0) planes of nanocrystalline Co_3O_4.

AFM images (**Fig. 6-5**) within a 400 nm by 400 nm area reveal surface traces of graphene nanosheets and Co_3O_4 nanoparticles. As shown in **Fig. 6-5(a)**, Co_3O_4 nanoparticles are identified as bright dots. When height differences are considered, the AFM image clearly shows that some of the Co_3O_4 nanoparticles were deposited on a lower graphene nanosheet layer as indicated by a lighter colour above the red line. Whereas, other Co_3O_4 nanoparticles were dispersed on a relatively higher layer of graphene nanosheets as indicated by a brighter colour below the red line. Graphene nanosheets were stacked in several layers and were corrugated when they were dried, resulting in height differences in the various areas examined. The Co_3O_4 nanoparticles stabilized the graphene nanosheets and acted as spacers to prevent the graphene layers from aggregating. The Co_3O_4 nanoparticles deposited at different height levels, as shown in this AFM image. **Fig. 6-5(b)** presents a height profile across the examined region, as marked by the red line in **Fig. 6-5(a)**. The height difference of the single

Co_3O_4 nanoparticle on the line is 17.8 nm, which is the size of the particle. The thickness of the graphene nanosheet lying on the line is evaluated to be 3–5 nm, which further confirmed the formation of several layers of graphene nanosheets.

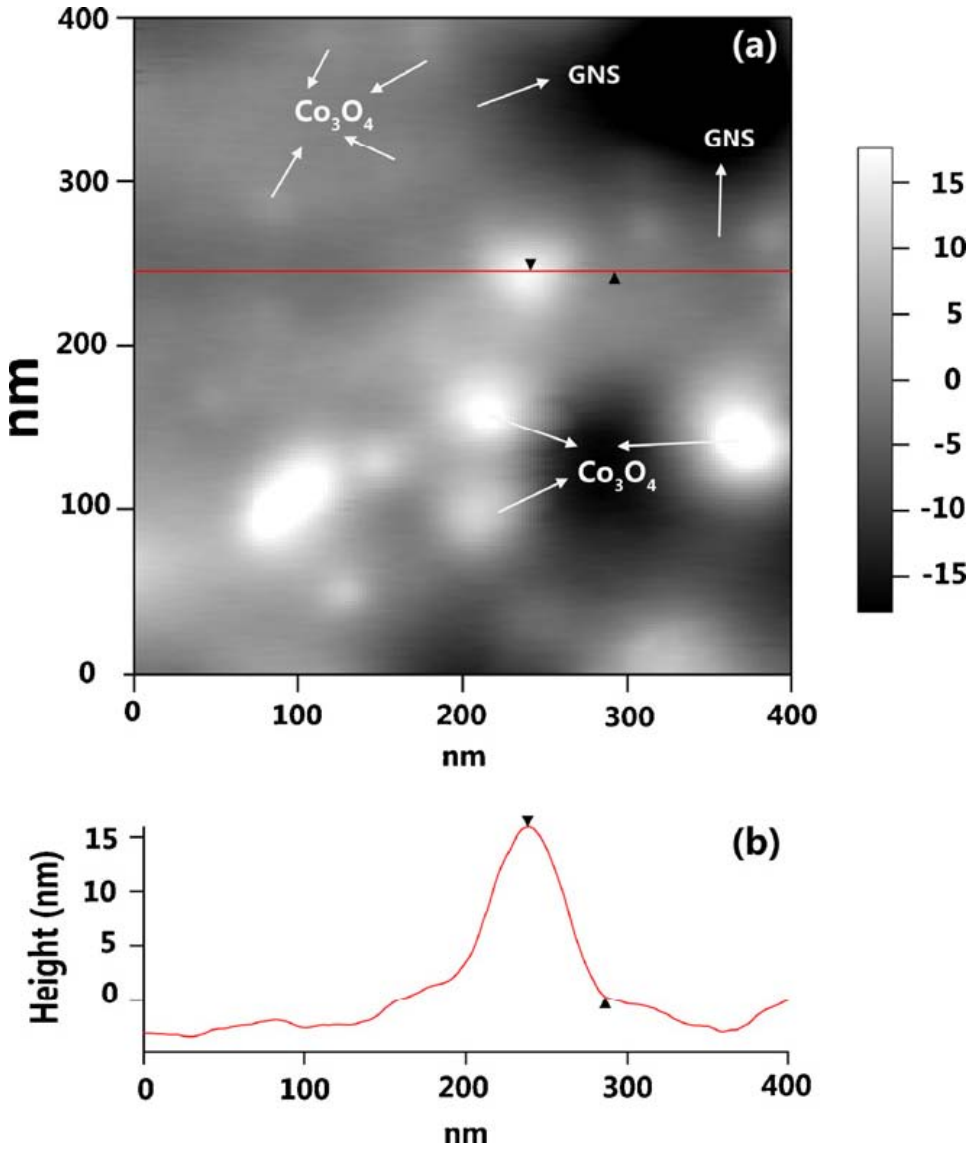

Fig. 6-5 AFM images covering an area of 400 nm by 400 nm: (a) surface evidence of graphene nanosheets and deposited Co_3O_4 nanoparticles; (b) height profile across the red line; the particle size of the single Co_3O_4 nanoparticle on the line is 17.8 nm.

The weight percentage of the graphene nanosheets in Co_3O_4/GNS nanocomposite was determined by TGA measurement (as shown in **Fig. 6-6**). The dramatic weight loss was due to the decomposition of Co_3O_4 to CoO and the consumption of graphene in air as

temperature increased. The final product left was CoO only, with a weight percent of ~51.0%. The composition of Co_3O_4 nanoparticles in the Co_3O_4/GNS nanocomposite was determined to be 45.4 wt% based on the weight percentage of CoO. Therefore, the nanocomposite consists of 45.4 wt% graphene and 54.6 wt% Co_3O_4 nanoparticles.

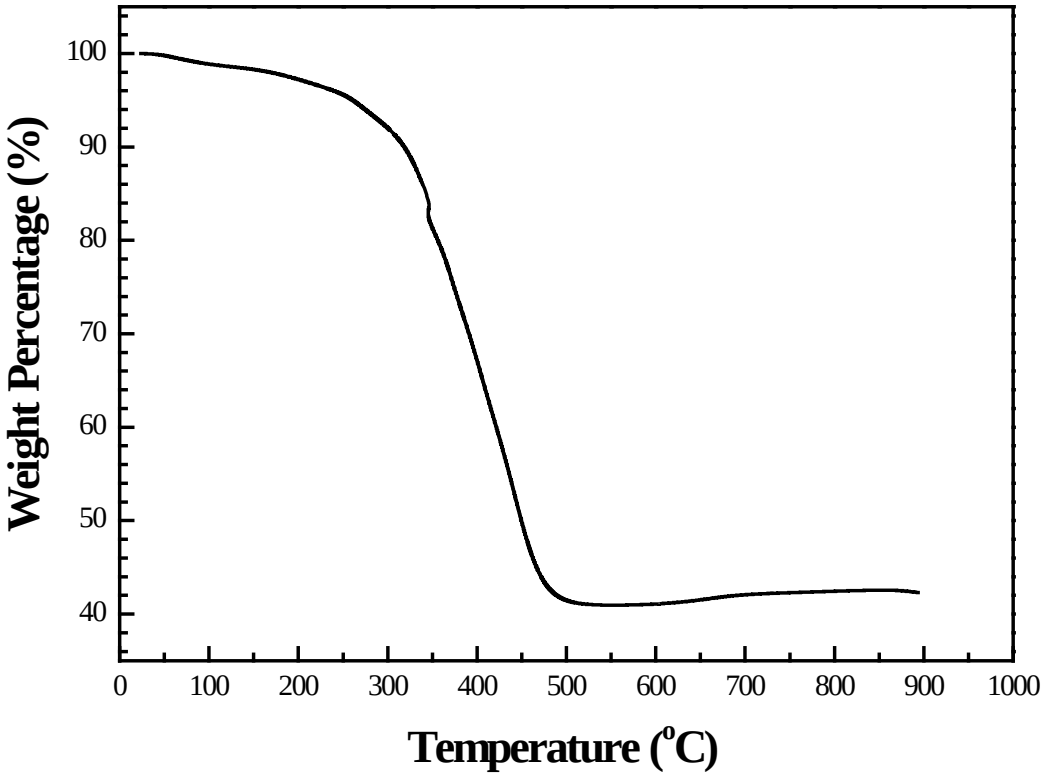

Fig. 6-6 TGA curve of the Co_3O_4/GNS nanocomposite.

The electrochemical reactivity of Co_3O_4/GNS nanocomposite as an anode material in lithium ion cells was first assessed by CV measurements. **Fig. 6-7** shows the CV curves of Co_3O_4/GNS electrode in the 1st, 2nd, and 50th scanning cycles. The redox reactions involved between Co_3O_4 and Li can be expressed as follows:

$$8Li^+ + Co_3O_4 + 8e^{-1} \leftrightarrow 4Li_2O + 3Co \quad (\textbf{Eq. 6-1})$$

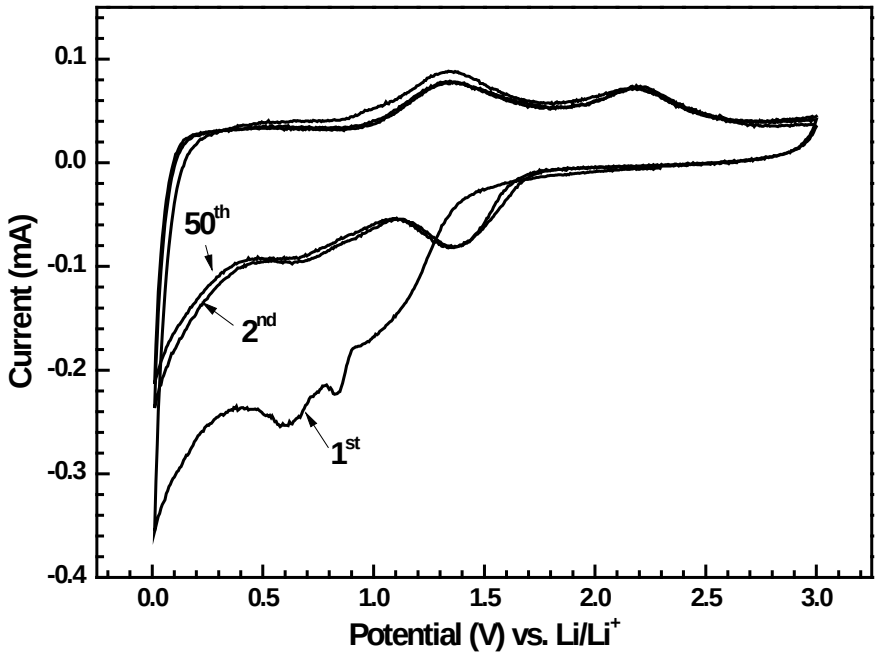

Fig. 6-7 CV curves of Co_3O_4/GNS anode over a voltage range of 0.01–3 V at a scan rate of 0.1 mV s^{-1} in the 1st, 2nd and 50th cycles.

In the first cycle, the discharge curve has a longer sloping part, and two small cathodic peaks appear at 0.62 V and 0.84 V, which can be attributed to the formation of the solid electrolyte interphase (SEI) layer. Both of the peaks disappear from the second cycle. The other two reduction peaks are located around 0.6 V and 1.35 V, and could be due to the insertion of lithium ions into Co_3O_4 nanoparticles at different stages. Two oxidation peaks appear around 1.32 V and 2.2 V, and these could be due to the process of lithium ion extraction from the Co_3O_4 nanoparticles. The insertion and extraction processes of lithium ions through graphene nanosheets are evidenced by the reduction and oxidation peaks located at 0.01 V and 0.17 V, respectively.

Fig. 6-8 shows the charge/discharge profile of the Co_3O_4/GNS nanocomposite

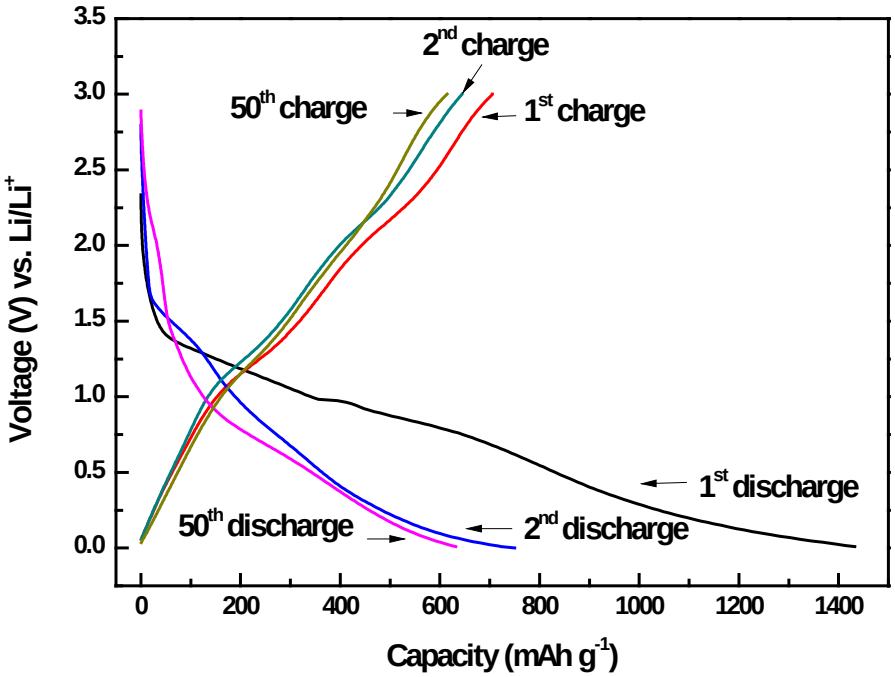

Fig. 6-8 Charge/discharge profiles of Co_3O_4/GNS anode at a current rate of 55 mA g^{-1} in the 1st, 2nd and 50th cycles.

material as an anode in a lithium cell under galvanostatic charge/discharge cycling at a current rate of 55 mA g^{-1}. In the first cycle, the Co_3O_4/GNS nanocomposite material delivered a lithium insertion capacity of 1433 mAh g^{-1} and a reversible charge capacity of 705 mAh g^{-1}. In the second cycle, a discharge capacity of 722 mAh g^{-1} was obtained, while the reversibility was improved significantly and the composite electrode maintained good cyclability. The theoretical lithium storage capacity that graphene could contribute is 744 mAh g^{-1}, based on the assumption that all graphene nanosheets are well separated and strictly monolayers. Co_3O_4 has a theoretical lithium capacity of 890 mAh g^{-1}. The as-prepared Co_3O_4/GNS nanocomposite material contains 54.6 wt% of Co_3O_4 nanoparticles and 45.4 wt% of graphene nanosheets. Therefore, the maximum possible theoretical capacity of the Co_3O_4/GNS nanocomposite material is calculated to be 823.7 mAh g^{-1}, based on the theoretical capacities of graphene (744 mAh g^{-1}) and

Co_3O_4 (890 mAh g^{-1}). Thus, the initial reversible discharge capacity (722 mAh g^{-1}) obtained for the Co_3O_4/GNS nanocomposite material was very close to the theoretical capacity of the Co_3O_4/GNS nanocomposite material.

The reversible lithium storage capacity *vs.* cycle number of Co_3O_4/GNS, commercial Co_3O_4 nanoparticles and bare graphene nanosheets is shown in **Fig. 6-9**. The Co_3O_4/GNS electrode delivered a reversible discharge capacity of 722 mAh g^{-1} at 55 mA g^{-1} and maintained a capacity of 631 mAh g^{-1} after 50 cycles. The Co_3O_4 nanoparticle electrode exhibited better lithium storage capacity at the first few cycles but then faded quickly during the cycling test. Only 230 mAh g^{-1} was maintained after 50 cycles. Similarly, the bare graphene electrode only exhibited a discharge capacity of only 273 mAh g^{-1} after 50 cycles and 255 mAh g^{-1} after 100 cycles at 55 mA g^{-1}, as demonstrated in Chapter 4. Therefore, it has been shown that the Co_3O_4/GNS electrode performed much better than the bare graphene electrode or the Co_3O_4 nanoparticle electrode, by exhibiting highly reversible lithium storage capacity, excellent cycling stability, and high Columbic efficiency. This enhancement of electrochemical properties when Co_3O_4/GNS is used instead of bare graphene or Co_3O_4 nanoparticles, can be attributed to the contributions of both graphene nanosheets and Co_3O_4 nanoparticles. The distribution of Co_3O_4 nanoparticles among the graphene nanosheets has effectively separated the graphene nanosheets, creating a uniformly layered structure, and, increased the lithium storage capacity of the material. The graphene nanosheets in this case have provided carbons as a buffer medium to overcome the problem associated with the volume expansion/contraction in the lithium cells when Co_3O_4 nanoparticles react with lithium by lithium insertion/extraction.[126, 127] Furthermore, the aggregation of Co_3O_4 nanoparticles on the graphene nanosheets is efficiently prevented. Therefore, upon cycling, the active material can resist cracking and crumbling, and

maintain large capacity and cycling stability.[126] As graphene has good conductivity,[165] the internal resistance in the lithium cells could be minimized to stabilize the electronic and ionic conductivity, thereby leading to a higher specific capacity.[166]

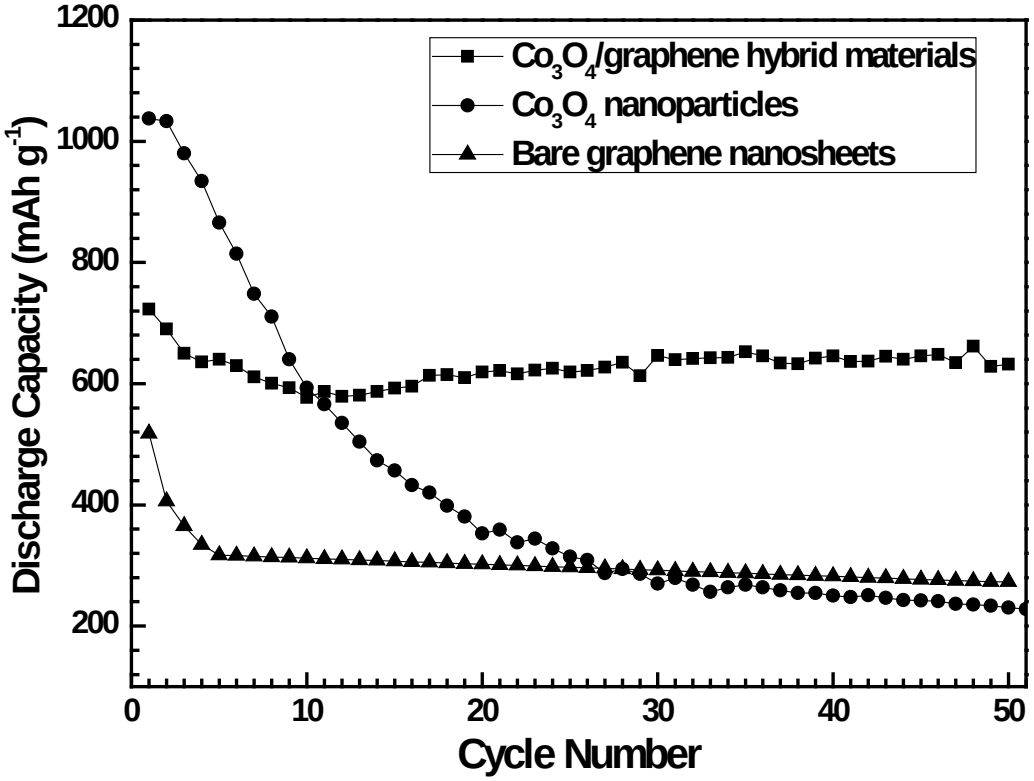

Fig. 6-9 Cycling performance of Co_3O_4/GNS nanocomposite material, Co_3O_4 nanoparticles, and bare graphene nanosheets as anode materials at a current of 55 mA g^{-1}.

Fig. 6-10 shows the CV curves of the as-prepared Co_3O_4/GNS nanocomposite material as electrode material in a supercapacitor with 2 M KOH electrolyte at different scanning rates. All the CV curves present a similar shape; oxidation and reduction peaks appear at various scan rates. The oxidation peak at 0.36 V and the reduction peak at 0.42 V were assigned to the redox reactions arising from the embedded Co_3O_4

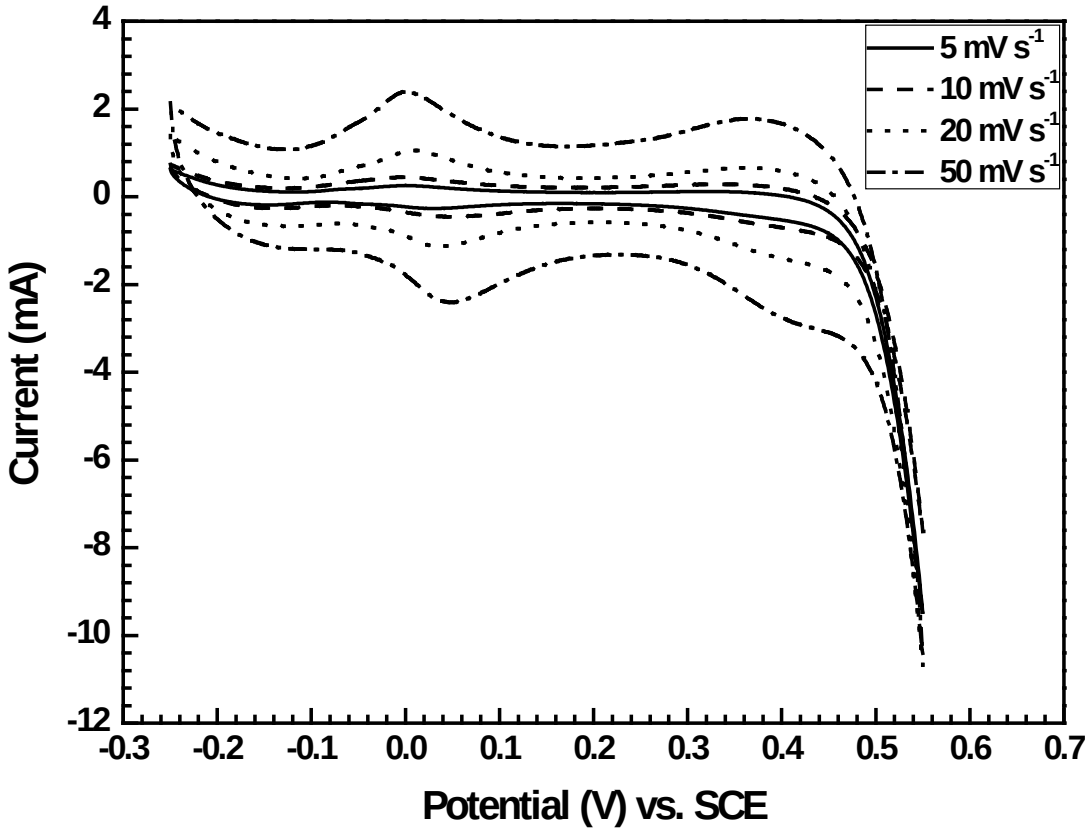

Fig. 6-10 CV curves of Co_3O_4/GNS as working electrode in a supercapacitor cell in 2 M KOH over a voltage range of −0.25–0.55 V at scan rates of 5 mV s^{-1}, 10 mV s^{-1}, 20 mV s^{-1}, and 50 mV s^{-1}, respectively.

nanoparticles in 2 M KOH. In the lower voltage region, the −0.01 V oxidation peak and the 0.04 V reduction peak are due to the effects of epoxyl, hydroxyl, and carboxyl functional groups attached to the graphene nanosheets. These functional groups formed in the chemical synthesis process of graphene nanosheets.[27, 137] The indirect evidence for these surface functional groups in the graphene-based composites was confirmed by elemental analysis as detailed in Chapter 5.[167] The maximum specific capacitance evaluated is 478 F g^{-1} at a scan rate of 5 mV s^{-1}. It is considered that the total specific capacitance is made up of double layer capacitance generated by the graphene, and pseudocapacitance contributed by Co_3O_4 nanoparticle facilitated redox

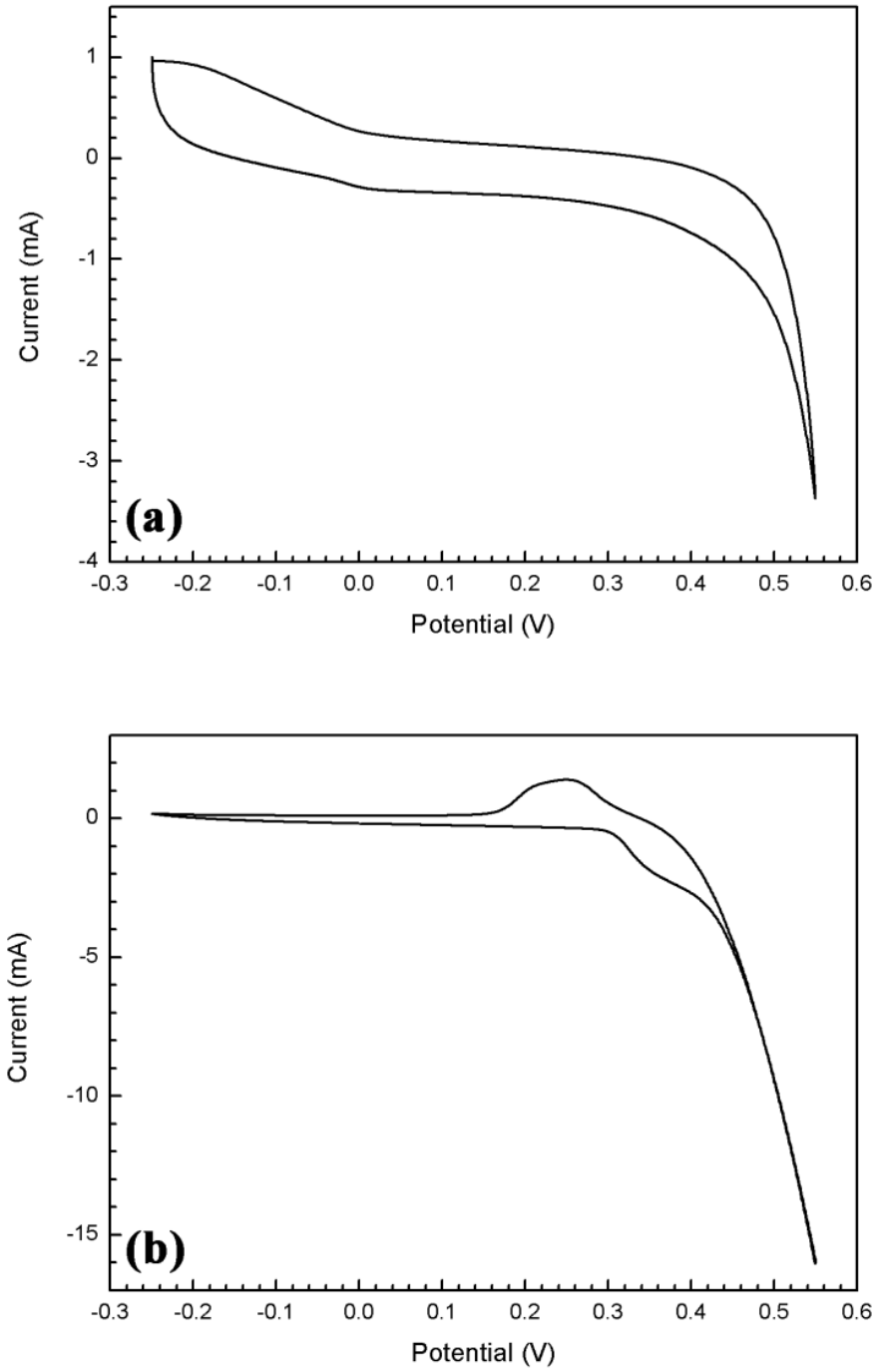

Fig. 6-11 CV curves of (a) pure graphene nanosheets and (b) commercial Co_3O_4 powders (< 50 nm) in 2 M KOH electrolyte at a scan rate of 5 mV s^{-1}.

reactions. Nanosized commercial Co_3O_4 powders (<50 nm) and bare graphene nanosheets yield a maximum specific capacitance of 118 F g^{-1} and 245 F g^{-1}, respectively, at 5 mV s^{-1} in 2 M KOH (**Fig. 6-11**). Compared to the specific capacitance

delivered by commercial Co_3O_4 nanoparticles and bare graphene nanosheets, the electrochemical performance of the Co_3O_4/GNS composite material is significantly increased as Co_3O_4 nanoparticles are inserted into graphene nanosheets. The presence of the Co_3O_4 nanoparticles prevents the graphene nanosheets from aggregating, making both sides of the graphene nanosheets accessible for K^+ ion insertion and de-insertion. Graphene nanosheets also provide a highly conductive carbon matrix to minimize the internal resistance and facilitate the electrochemical activities. As bare graphene nanosheets are in the form of multi-layers, the BET surface area of graphene is only 93.7 m2 g^{-1} and not sufficiently extended (BET result in Chapter 5). By contrast, the BET surface area of the as-prepared Co_3O_4/GNS nanocomposite material obtained from the N_2 adsorption/desorption isotherms in **Fig. 6-12**, is significantly extended to

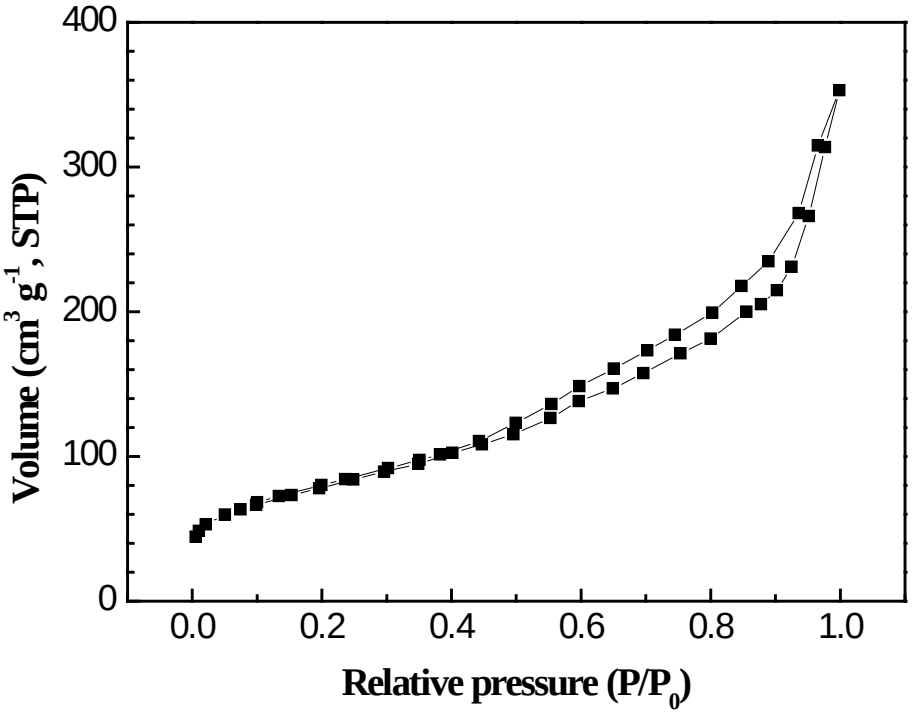

Fig. 6-12 N_2 adsorption/desorption isotherms of Co_3O_4/GNS nanocomposite.

219.2 m^2 g^{-1} due to the function of Co_3O_4 nanoparticles as spacers. The extended graphene layers, with enlarged interlayer space and surface area, are therefore favourable for the formation of double layer capacitance. Furthermore, the particle size of Co_3O_4 in a graphene domain is restricted upon formation between graphene layers and is relatively smaller (15–25 nm), compared to commercial Co_3O_4 nanoparticles (<50 nm). The superior electrochemical behaviour of the composite material is also associated with these smaller embedded nanoparticles. The decrease of the particle size of the deposited Co_3O_4 nanoparticles would lead to the increase of the specific capacitance of those nanoparticles in the composite. A similar effect has been reported for composites having particles of RuO_2 deposited on carbon nanofibres.[168] It is also very interesting to find that the surface-related capacitance of the composite material is 2.18 F m^{-2}. This result is relatively large compared with ordinary carbon,[71] however, it is similar to carbon materials with surface functionalities.[153, 154] It has been proposed that surface functional groups attached to the carbon materials could provide supplementary pseudocapacitive contribution to a dominant double-layer capacitance to enhance the specific capacitance of the modified carbon materials.[150-152, 169] Therefore, it is believed the functional groups in the as-prepared nanocomposite material are also electrochemically active, and could participate in the redox reactions and contribute extra pseudocapacitance to the electrochemical performance.

In summary, Co_3O_4 nanoparticles play two major roles in the Co_3O_4/GNS nanocomposite material in managing the enhancement of the electrochemical performance. Firstly, the Co_3O_4 nanoparticles act as spacers to stabilize the graphene nanosheets. The interlayer space and accessible surface area of the graphene are therefore extended when Co_3O_4 nanoparticles are inserted. When applied in lithium-ion batteries and supercapacitors, graphene provides a highly conductive medium and much

more flexible layers with enlarged interlayer space and increased surface area, benefiting the electrochemical performance in energy storage. Secondly, Co_3O_4 nanoparticles participate in the electrochemical activities, not only in lithium-ion batteries, but also in the supercapacitors. Co_3O_4 nanoparticles can deliver a high lithium-ion storage capacity and pseudocapacitance from redox reactions, and therefore make electrochemical contributions towards the overall electrochemical performance of the composite material.

6.4 Conclusions

An in-situ chemical method has been developed to prepare Co_3O_4/GNS nanocomposite material for energy storage applications. The prepared nanocomposite material consists of uniform Co_3O_4 nanoparticles (15–25 nm in size) distributed on separated graphene nanosheets. The electrochemical properties of the composite material are enhanced significantly, as embedded Co_3O_4 nanoparticles can protect graphene from aggregation. Co_3O_4/GNS nanocomposite material exhibited a high lithium storage capacity of 722 mAh g^{-1} in lithium-ion cells and a high supercapacitance of 478 F g^{-1} in supercapacitors.

Chapter Seven

Superior Electrochemical Performance of Sulfur/Graphene Nanocomposite Material for High-Capacity Lithium-Sulfur Batteries

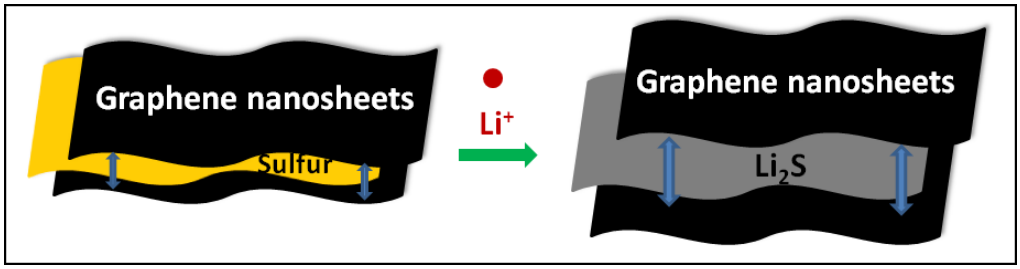

Chapter 7 — Superior Electrochemical Performance of Sulfur/Graphene Nanocomposite Material for High-Capacity Lithium-Sulfur Batteries

7.1 Introduction

As an alternative power source to lithium-ion batteries,[170] lithium-sulfur batteries have been investigated for decades. The configuration of a standard lithium-sulfur cell is quite simple, with lithium metal acting as the anode and sulfur playing the role of the cathode. A typical discharge process consists of two discharge stages: the reduction of sulfur to polysulfide followed by further reduction of polysulfide in the first stage (**Eq. 7-1**), and the transformation of polysulfide into sulfide in the second stage (**Eq. 7-2**).[170-172]

$$S_8 + Li^+ + e^- \rightarrow Li_2S_x \text{ (2.4–2.1 V)} \qquad \textbf{(Eq. 7-1)}$$

$$Li_2S_x + Li^+ + e^- \rightarrow Li_2S_2 \text{ and/or } Li_2S \text{ (2.1–1.5 V)} \qquad \textbf{(Eq. 7-2)}$$

Based on the complete reaction from S_8 to Li_2S, sulfur has the highest theoretical capacity of 1675 mAh g^{-1} and an energy density of 2600 Wh kg^{-1} among hitherto considered cathode materials. Therefore, lithium-sulfur batteries have great potential as the next generation of lithium batteries for large-scale and high-power applications on account of their low cost, environmental friendliness, high capacity, and high energy density.

Despite these promising advantages, lithium-sulfur batteries are still far from being employed in practical applications. The major hurdles of lithium-sulfur batteries are associated with the nonconduction of sulfur, the lack of suitable electrolytes, and the capacity degradation on cycling. Because sulfur is electronically insulating, certain

amounts of conductive additives have to be added to maintain good conductivity. Several forms of carbon, such as activated carbon,[173] carbon nanotubes,[174] mesoporous carbon,[175, 176] and conductive polymers[177-180] have been used in sulfur electrodes, with moderate capacity and cycling performance being achieved. However, it was found that polysulfide dissolved in the liquid electrolyte and migrated ("shuttled") through the separator to the anode. The diffused polysulfide could be further reduced to solid Li_2S_2 or LiS_2, which covered the lithium electrode and caused active mass loss and capacity fading.[181, 182] To overcome the shuttle issue, various electrolytes have been developed such as optimized organic electrolytes,[183] room-temperature ionic liquids that can limit the dissolution of polysulfide anions,[175, 184] conductive sulfur-contained polymer electrolytes,[185-187] solid-state based electrolytes,[188-190] and nanocomposite polymer electrolytes.[191] In 2009, Ji et al. reported that sulfur/mesoporous carbon composite used as the cathode material for lithium-sulfur batteries resulted in an excellent electrochemical performance.[192] With the assistance of a polymer-modified carbon surface, a reversible capacity of up to 1320 mAh g^{-1} at 0.1 C was achieved in an organic electrolyte, with good capacity retention for 20 cycles. Recently, sulfur/highly porous graphene nanocomposite was also applied by means of a sulfur-incorporation method and the cycling performance improved significantly, with ultrahigh specific capacity at a low current rate.[45] Another example was graphene-wrapped sulfur particles trapped by a poly(ethylene glycol) (PEG) coating. However, moderate capacities were achieved and the electrochemical performance was only marginally improved.[193] The latest substantial outcomes include a reservoir mechanism introduced to trap polysulfide anions during discharge processes,[194] elemental sulfur encapsulated and sequestered by mesoporous hollow carbon capsules,[195] and silicon–sulfur batteries.[196] In these cases, the

specific capacities of the lithium-sulfur cells were greatly enhanced with excellent cycling stabilities.

There have been many electrolytes reported for lithium-sulfur batteries; however, there has been no systematic report about the effect of different electrolytes on the cycling properties. A binary electrolyte based on tetra(ethylene glycol) dimethyl ether (TEGDME) and 1,3-dioxolane (DOX) was studied for use in lithium-sulfur batteries by Korean researchers in 2002.[197] It was found that the cyclic ether (DOX) could facilitate the formation of shorter polysulfide anions at around 2.4 V and the linear ether (TEGDME) could reduce the viscosity of the electrolyte for improved sulfur utilization at a low voltage plateau from around 2.1 V. Therefore, an electrolyte consisting of 1 M lithium bis(trifluoromethane sulfone)imide (LiTFSI, $LiN(SO_2CF_3)_2$) in a mixture of 1,2-dimethoxyethane (DME) and 1,3-dioxolane (DOX), was employed in this investigation. This chapter reports on the superior electrochemical performance of a S/GNS nanocomposite, in which elemental sulfur is impregnated into graphene nanosheet frameworks, when it is used as the cathode material in lithium-sulfur batteries. Phase change always accompanies the redox reactions in lithium-sulfur batteries but the soft and flexible graphene nanosheets provide a buffer to accommodate the volume change of sulfur, thereby leading to a durable cycle life for lithium-sulfur cells. The as-prepared S/GNS nanocomposite delivered a lithium storage capacity of 1580 mAh g^{-1} at 0.05 C, which is very close to its theoretical capacity, and showed an excellent cycling performance. The high specific capacity and enhanced cycling performance could also be attributed to the further improvement of sulfur utilization with the above electrolyte. Surprisingly, the as-prepared S/GNS nanocomposite also exhibited discharge capacities of 1201 mAh g^{-1} at a 1 C rate and 950 mAh g^{-1} at a 2 C rate, with excellent cyclability for up to 100 cycles.

7.2 Experimental

7.2.1 Material Synthesis

GONS was initially prepared by means of a modified Hummers method[36] followed by reduction with hydrazine to obtain graphene nanosheets.[35] The graphene product was washed, dried, and directly used without any further modification. Typically, graphene (50 mg) was mixed with elemental sulfur (50 mg) in a weight ratio of 1:1. The mixture was ground in a mortar for 15 min, then placed in an oven and maintained at 160 °C in air for 1 h.

7.2.2 Material Characterization

An XRD pattern of the obtained material was recorded with a Siemens D5000 X-ray diffractometer from 10 to 80° under a scan rate of 1° min^{-1}. For comparison, the XRD patterns of crystalline sulfur and pure graphene nanosheets were also obtained under the same conditions. General morphologies, energy-dispersive X-ray elemental mapping of S/GNS nanocomposite material, and the surface observation of the electrodes were conducted with a Zeiss Supra 55VP FESEM with an Oxford EDS system. The Raman spectra were recorded with a Renishaw inVia Raman spectrometer by using 514 nm excitation and 1800 L mm^{-1} grating. The samples were focused using a 50x objective, and the scans were recorded by means of a 10 s exposure from 100 to 3500 cm^{-1}. Sulfur content in the nanocomposite material was determined in air by TGA with a TGA/DTA analyzer (TA Instruments, SDT 2960 module).

7.2.3 Electrochemical Testing

To fabricate electrodes for electrochemical measurement, a blend of the as-prepared S/GNS nanocomposite material (80 wt%), carbon black (10 wt%), and PVdF (10 wt%) was mixed with NMP to form a slurry. The slurry was coated on aluminum foils and then dried at 80 °C for 12 h in a vacuum oven. Lithium foils were used as the negative electrode. The electrolyte was prepared by dissolving 1 M LiTFSI salt in a mixed solvent of DME and DOX (8:2 in volume ratio). The preparation of the electrolyte and the assembly of CR2032 coin cells were performed in an argon-filled glove box (Unilab, MBraun, Germany), in which the moisture and oxygen were controlled to be less than 0.1 ppm. CV measurements were conducted with an Electrochemistry Workstation (CHI660D) at a sweep rate of 0.1 mV s^{-1} in a potential window of 1–3.5 V versus Li/Li^+ reference electrode. The AC impedance measurements were performed on a freshly prepared cell before cycling, and after 5 and 50 cycles, respectively. The frequency was set in the range of 100 kHz to 0.01 Hz with amplitude of 5 mV. The galvanostatic charge/discharge test was carried out in the voltage range of 1 to 3 V at room temperature, at the current rates of 84, 1675, and 3350 mA g^{-1} (equivalent to 0.05, 1, and 2 C), respectively.

7.3 Results and Discussion

A S/GNS nanocomposite was prepared by homogeneously mixing graphene nanosheets with commercial crystalline sulfur, heating the mixture above the melting point of sulfur (160 °C). During the impregnation process, sulfur was transformed into its liquid state and diffused into the space between the graphene interlayers. As shown in the XRD patterns in **Fig. 7-1(a)**, pure elemental sulfur has various diffraction peaks. However, for

pure graphene nanosheets and the S/GNS nanocomposite material, only the diffraction peaks of graphene (carbon) are visible. No diffraction lines of sulfur can be identified in the XRD pattern of the S/GNS nanocomposite because the crystalline sulfur has been converted into amorphous sulfur and then dispersed within the graphene nanosheet

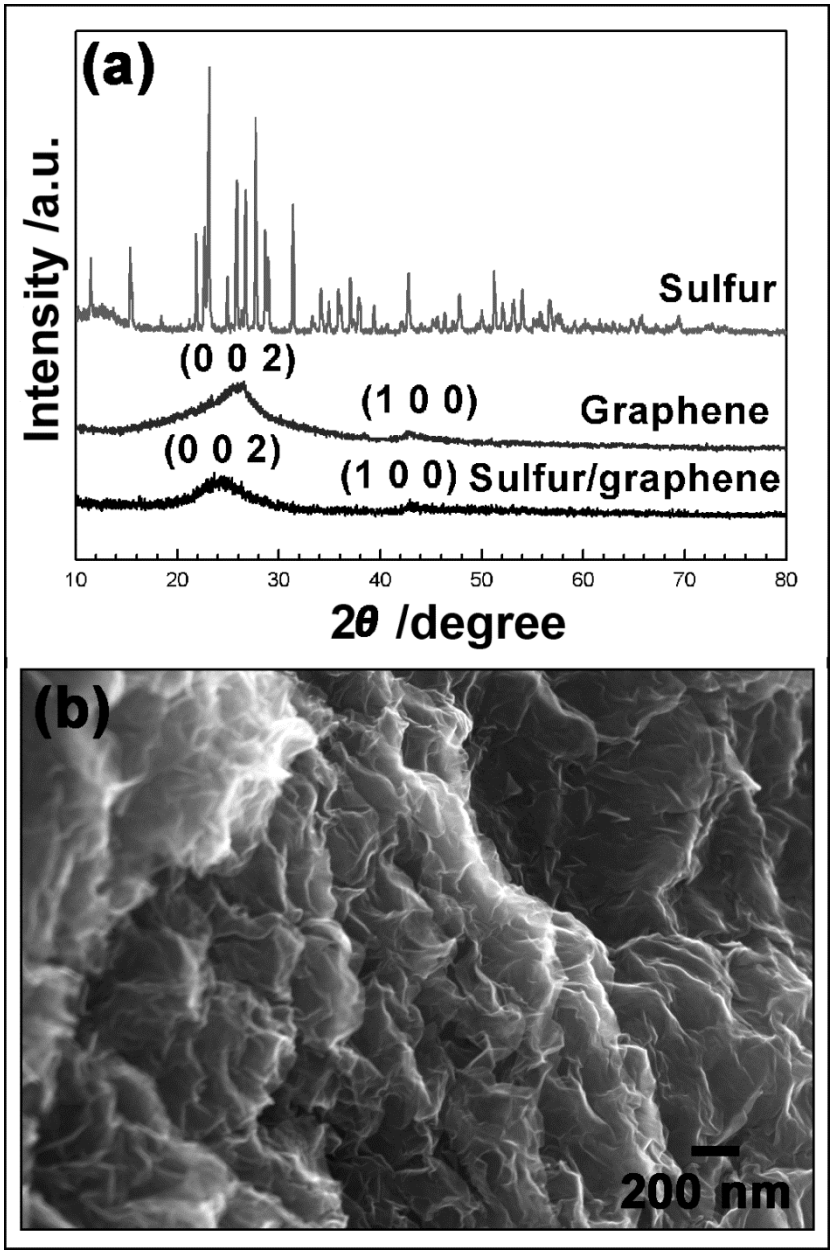

Fig. 7-1 (a) Pure sulfur crystalline, pure graphene nanosheets, and S/GNS nanocomposite. (b) A high resolution FESEM image showing general morphology of the S/GNS nanocomposite material.

matrix.[173] **Fig. 7-1(b)** shows an FE-SEM image of the S/GNS nanocomposite, which only displays corrugated flexible graphene nanosheets without any aggregations of sulfur powders. This indicates the full incorporation of sulfur into the graphene nanosheet matrix. A similar phenomenon has also been observed in sulfur/mesoporous carbon composite.[192] Energy dispersive X-ray (EDX) elemental mapping (**Fig. 7-2**) provides additional evidence confirming the uniform distribution of sulfur on the surface of graphene nanosheets in the nanocomposite. The carbon and sulfur elemental

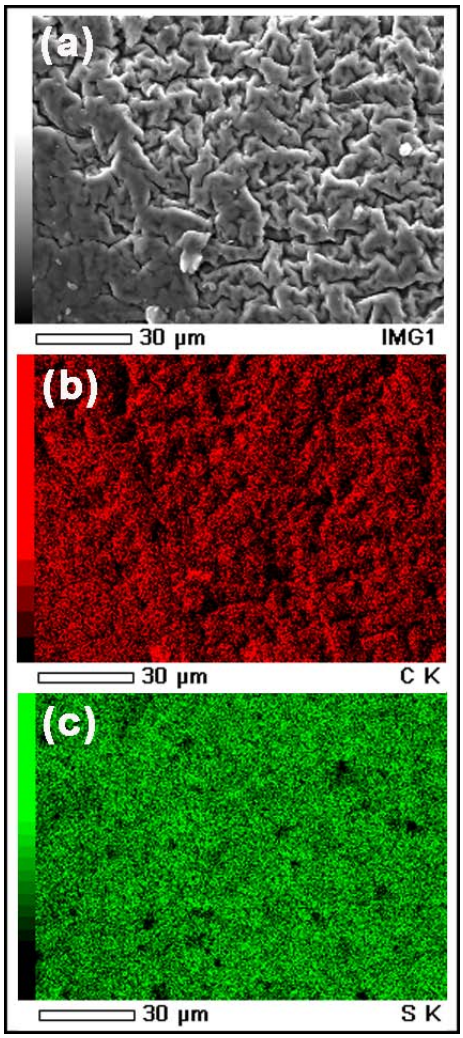

Fig. 7-2 (a) A low-magnification FESEM image of S/GNS nanocomposite material. (b) Elemental mapping of carbon, and (c) elemental mapping of sulfur.

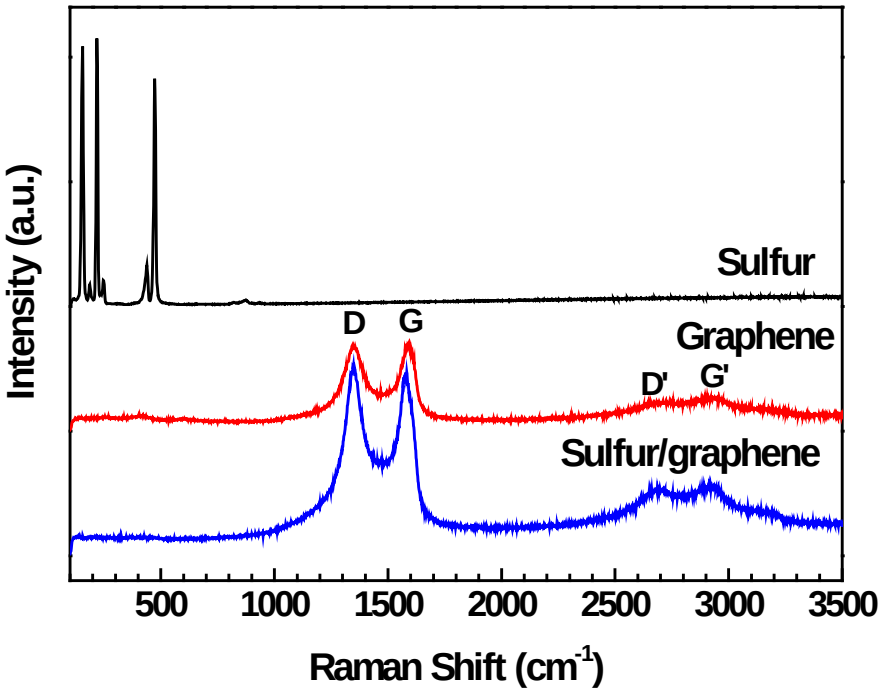

Fig. 7-3 Raman spectra of crystalline sulfur, pure graphene nanosheets, and S/GNS nanocomposite at an extended range from 100 to 3500 cm^{-1}.

maps (**Fig. 7-2(b) and (c)**) clearly demonstrate that the amorphous sulfur has filled the interlayer space between the graphene nanosheets, which ensures intimate contact between graphene and sulfur. Therefore, graphene nanosheets can effectively function as a highly conductive medium with a large surface area for the distribution of sulfur on the surfaces of graphene nanosheets.

Raman spectra of crystalline sulfur, pure graphene nanosheets, and S/GNS nanocomposite are shown in **Fig. 7-3**. Sulfur presents six Raman peaks at a low wavenumber region, and they are assigned to E_2 (155 cm^{-1}), B_1 (186 cm^{-1}), A_1 (219 cm^{-1}), E_3 (247 cm^{-1}), E_3 (438 cm^{-1}), and A_1 (474 cm^{-1}) modes of crystalline sulfur, respectively.[198] Graphene and S/GNS nanocomposite exhibit Raman spectra very

similar to each other with typical D bands (1349 cm^{-1}), G bands (1590 cm^{-1} for graphene and 1578 cm^{-1} for S/GNS nanocomposite), D' bands (2694 cm^{-1}), and G' bands (2919 cm^{-1}) within the examined range. In the spectra of both graphene and S/GNS, generally, G bands are assigned to the E_{2g} vibrational mode, and D bands are associated with broken symmetry or a high density of defects.[199] The D/G intensity ratio increases significantly relative to pristine graphite, which indicates the exfoliation of graphene sheets from the sp^2 carbon matrix of bulk graphite.[27] The Raman peaks, and their locations in the S/GNS spectrum, further confirmed the presence of graphene in the S/GNS nanocomposite. However, no sulfur bands could be detected in the Raman spectrum of S/GNS nanocomposite because sulfur remains amorphous and is fully covered by graphene nanosheets. The sulfur content in the nanocomposite was determined by TGA conducted under an atmosphere of air (as shown in **Fig. 7-4**). There were two obvious regions associated with the weight loss of the composite material. The weight loss from around 180 to 250 °C should be ascribed to the evaporation of sulfur, whereas the combustion of graphene was responsible for the weight loss from 500 to 570 °C. Therefore the composition of sulfur was calculated from the TGA to be 44.5 wt% in the S/GNS nanocomposite. The obtained sulfur content in the as-prepared nanocomposite was doubled when compared with the previously reported result of a S/GNS composite,[45] which was only 22 wt% at an initial weight ratio of 1:1.5 for graphene and sulfur.

Fig. 7-5 shows the CV curves of an S/GNS electrode in the voltage range of 1.0–3.5 V. Graphene is electrochemically inert in the selected voltage range, therefore the redox peaks on the CV curves can only be attributed to the reactions between lithium ions and sulfur. The first cathodic peak located around 2.4 V corresponds to the reduction of

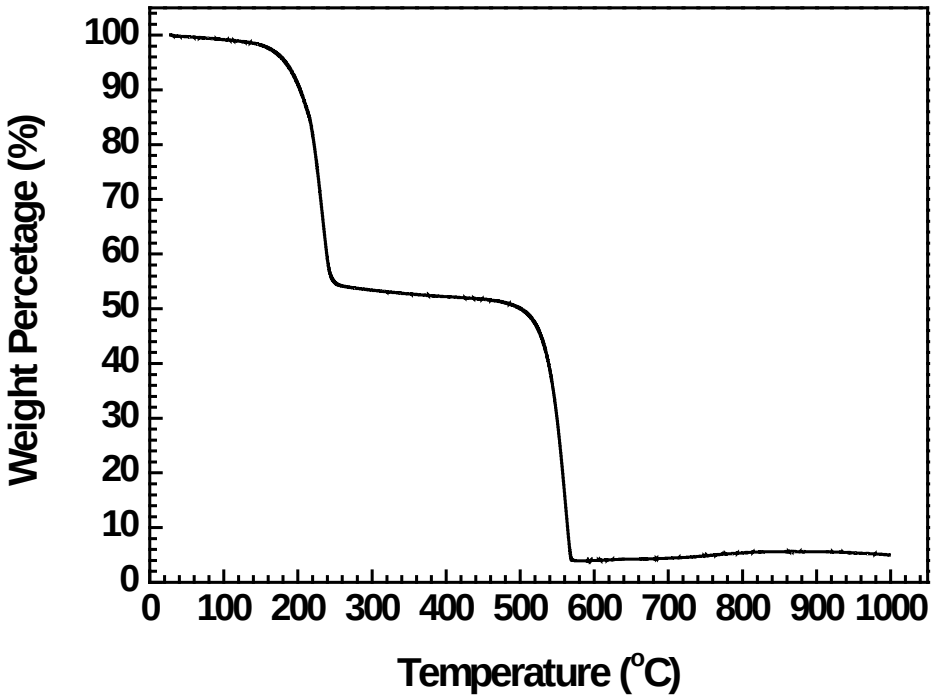

Fig. 7-4 TGA curve of the S/GNS nanocomposite material, ranging from room temperature to 1000 °C at 5 °C min^{-1} in air.

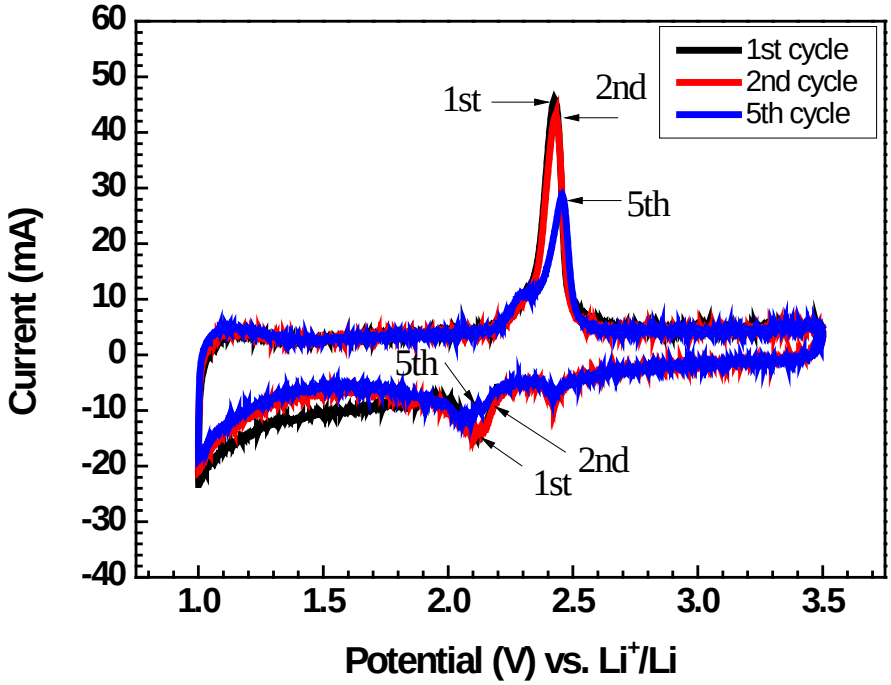

Fig. 7-5 CV curves of the S/GNS nanocomposite electrode in the 1st, 2nd, and 5th cycle. The scanning rate is 0.1 mV s^{-1}.

elemental sulfur to lithium polysulfide (Li_2S_x, $2<x<8$). The second cathodic peak at 2.1 V can be attributed to the change of lithium polysulfide to lithium sulfide (Li_2S_2 and Li_2S). The CV curves in the subsequent scanning cycles show a cathodic peak at 2.1 V, which represents a deep discharge procedure at the second discharge stage and effective utilization of sulfur. During the charge process, lithium polysulfide and lithium sulfide are converted into elemental sulfur, which corresponds to the anodic peak at around 2.4 V. A few small "shoulder" peaks can be seen in the fifth cycle, which could be associated with the slightly dissolved polysulfide anions; they diffuse to the lithium anode and form Li_2S_2 and/or Li_2S after reacting with lithium.[184] It should also be noted that the areas of these voltammetric peaks slightly decreased upon cycling. This could be due to the shuttling of active sulfur material on the electrodes, thereby causing a minor loss of active sulfur. However, the positions of the redox peaks on the CV curves do not shift, which indicates that the redox reactions between sulfur and lithium ions in the S/GNS electrodes are highly reversible.

Only sulfur is responsible for the overall electrochemical capacities of the S/GNS electrodes over the voltage range of 1–3 V. Consequently, the specific capacities reported in this chapter are based on the mass of sulfur only. **Fig. 7-6** shows charge/discharge profiles of S/GNS nanocomposite electrodes in the first scanning cycle at different current rates. Two discharge plateaus can be easily distinguished. The first discharge plateau (2.4–2.1 V) is short, whereas the second plateau (2.1–1.5 V) extends for longer, and contributes to the majority of the discharge capacity. These discharge voltage plateaus are consistent with the redox peaks in the CV curves (**Fig. 7-5**). At current rates of 0.05 and 1 C, the second discharge stages present a long horizontal plateau, whereas at the 2 C rate, the discharge profile shows a slope, which signifies an

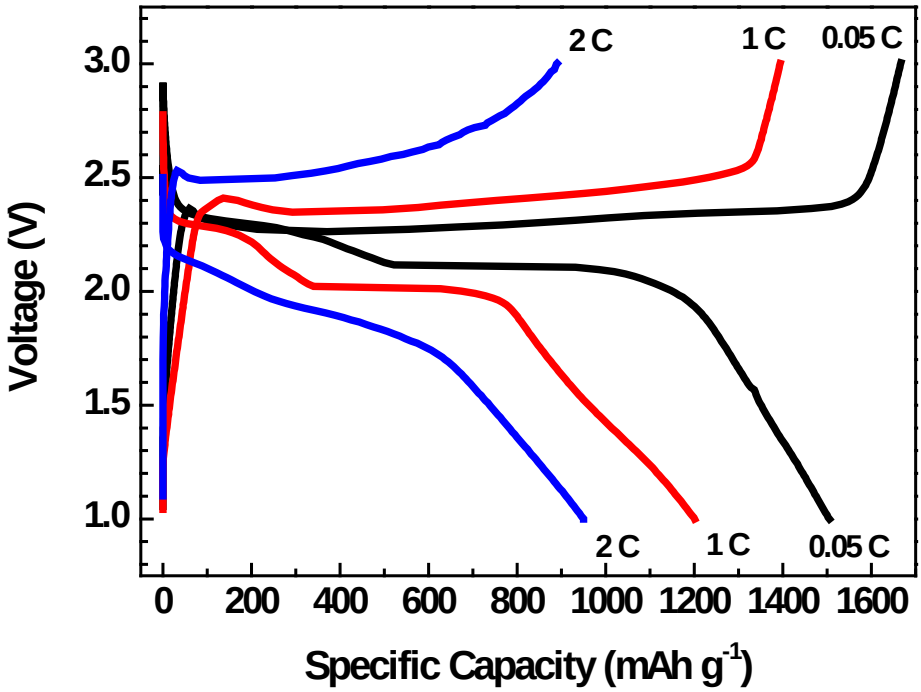

Fig. 7-6 The charge/discharge profiles of S/GNS nanocomposite electrodes in the first cycle at current rates of 0.05 C, 1 C, and 2 C, respectively.

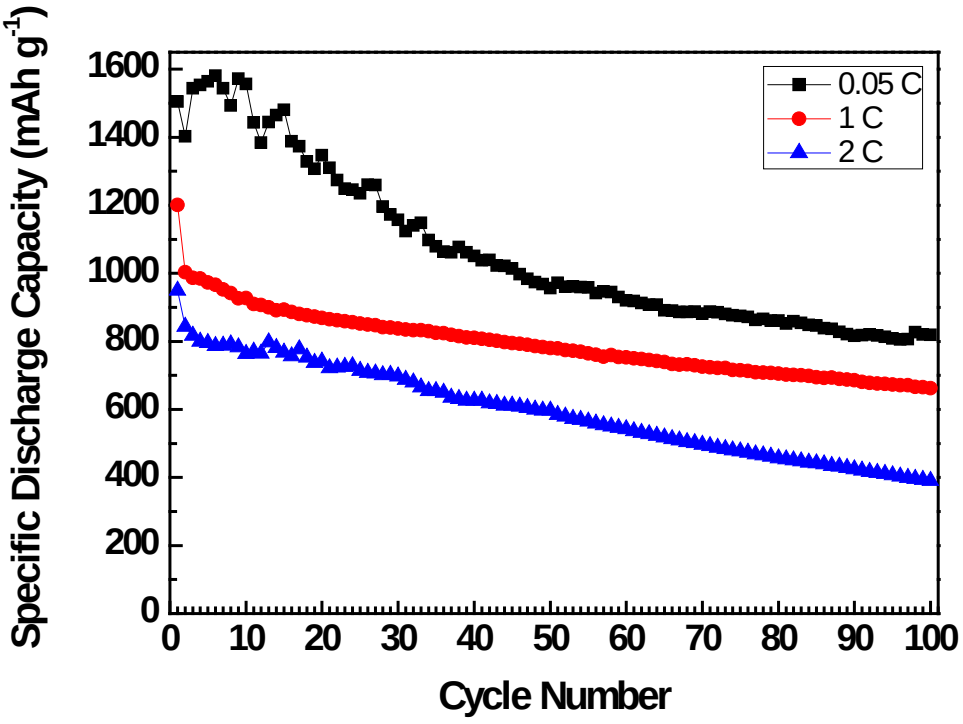

Fig. 7-7 Cycling performance of S/GNS nanocomposite electrodes at 0.05 C, 1 C, and 2 C, for 100 cycles.

incomplete reduction process on account of the higher current rate. The S/GNS nanocomposite material demonstrated a capability of complete lithiation even at the 1 C rate. **Fig. 7-7** shows the charge/discharge cycling performances at 84 (0.05 C), 1675 (1 C), and 3350 mA g^{-1} (2 C), respectively. The as-prepared S/GNS nanocomposite material delivered a specific discharge capacity of 1505 mAh g^{-1} at 0.05 C in the first cycle; the highest discharge capacity of 1580 mAh g^{-1} was achieved in the sixth cycle. The specific discharge capacity increased gradually during the first six cycles, which indicated increased utilization of sulfur upon cycling at the low current rate. The S/GNS electrode maintained very high discharge capacity over the first ten cycles and delivered reasonable discharge capacities for 100 cycles. A specific capacity of 819 mAh g^{-1} was retained in the 100th cycle.

Operation at high current rates is generally demanded for applications such as mobile phones and electric vehicles. Therefore, the electrochemical performance of S/GNS nanocomposite material at higher current rates was also investigated. It was found that the S/GNS nanocomposite could deliver an outstanding electrochemical performance at high current rates such as 1 and 2 C. The S/GNS nanocomposite electrodes achieved a discharge capacity of 1201 mAh g^{-1} at 1 C and 950 mAh g^{-1} at 2 C, respectively. The capacity declined slightly upon cycling, resulting in retained capacities of 662 mAh g^{-1} at 1 C and 391 mAh g^{-1} at 2 C after 100 cycles. This demonstrates the excellent high-rate cycling characteristics of the S/GNS electrodes.

Fig. 7-8 shows the electrochemical impedance spectroscopy (EIS) of the S/GNS nanocomposite electrode, measured after different cycles. The inset illustrates a magnified view of the impedance spectra in the high-frequency region. The value of the

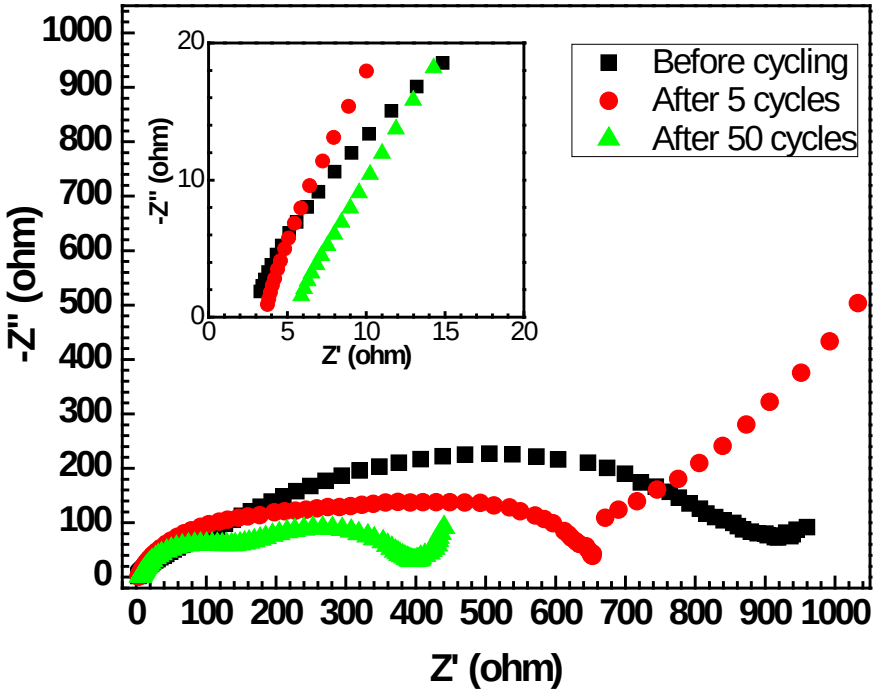

Fig. 7-8 EIS spectra of the S/GNS nanocomposite electrode before cycling, and after 5 and 50 cycles. The inset shows magnified EIS spectra at high frequency region.

intercept on the Z' axis is the resistance of the electrolyte (R_e) of the cell, which is very low. The initial R_e was 3.3 Ω for a noncycled cell. This increased slightly to 3.7 and 5.8 Ω after 5 and 50 cycles, respectively. In the high-frequency region, the impedance response displays a semicircle loop, and the corresponding diameter represents the charge-transfer resistance at the electrode/electrolyte interface. The diameters of the semicircles decrease with cycling; this could be because of the decrease in the charge-transport resistance at the interface of S/GNS active material and the electrolyte. It should be noted that two overlapped semicircles were found when the cell completed 50 cycles. The first semicircle in the high-frequency region is due to the formation of the solid electrolyte interface (SEI) film, which protects the electrode and results in an enhanced cycling performance. The middle-frequency semicircle is related to the impendence that arises from charge-transfer resistance at the interface of electrolyte and

S/GNS active material. It is clear that the charge-transfer resistance gradually decreases upon cycling. This can be attributed to more irreversible lithium insertions at the planar or basal edges on graphene nanosheets, which results from the attached functional groups at the unorganized carbon sites.[200, 201] This effect further increases the electric conductivity of graphene nanosheets in the lithium-sulfur cell. Therefore, the transportation of lithium ions becomes much easier as the cycle number increases, which benefits the electrochemical performance of the S/GNS electrodes.

The electrochemical performance of lithium-sulfur cells has been improved significantly relative to previously reported results. This significant improvement should be attributed to the use of the graphene nanosheet matrix. Firstly, graphene nanosheets act as the electric conduction medium to minimize the internal resistance of lithium-sulfur cells, as has been confirmed by the EIS measurements. Secondly, graphene nanosheets accommodate sulfur in the form of a sandwich structure. The soft and flexible graphene nanosheets provide an effective buffer to cushion the volume expansion and contraction of the S/GNS electrodes during the charge/discharge process. **Scheme 7-1** illustrates the sandwich structure of the S/GNS nanocomposite electrode and its cushion effect during volume change.

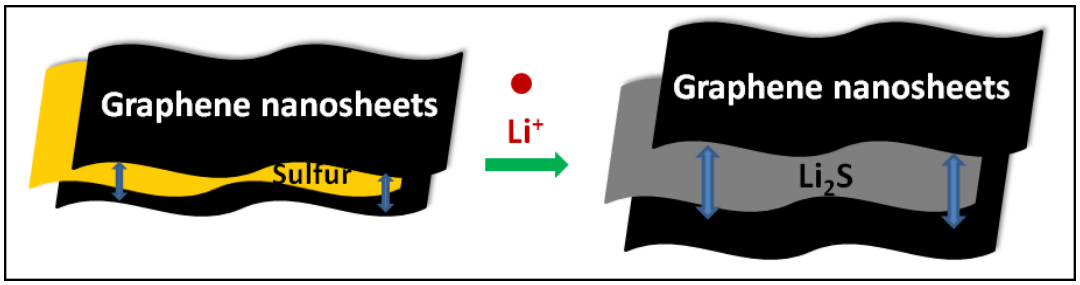

Scheme 7-1 Schematic illustration of the sandwich structure of S/GNS nanocomposite.

To further explore the buffer effect of graphene nanosheets, the surface of the S/GNS nanocomposite electrodes were analyzed before and after cycling by means of FE-SEM observations, which have been proved to be effective in identifying fracture on electrodes.[202, 203] The freshly prepared S/GNS nanocomposite electrode was taken for direct FE-SEM observation. The cycled cell was dismantled in the argon-filled glove box. The cycled electrode was washed with ethanol, dried in a vacuum oven, and then observed by means of FE-SEM for comparison. **Fig. 7-9(a) and (b)** show the low- and high-magnification FE-SEM images of the S/GNS nanocomposite electrode before cycling. The surface of the electrode is very smooth with homogeneous distribution of sulfur particles. In **Fig. 7-9(c)**, the cycled electrode exhibited a few slightly cracked edges and a mildly unflattened surface relative to the noncycled electrode; this is due to

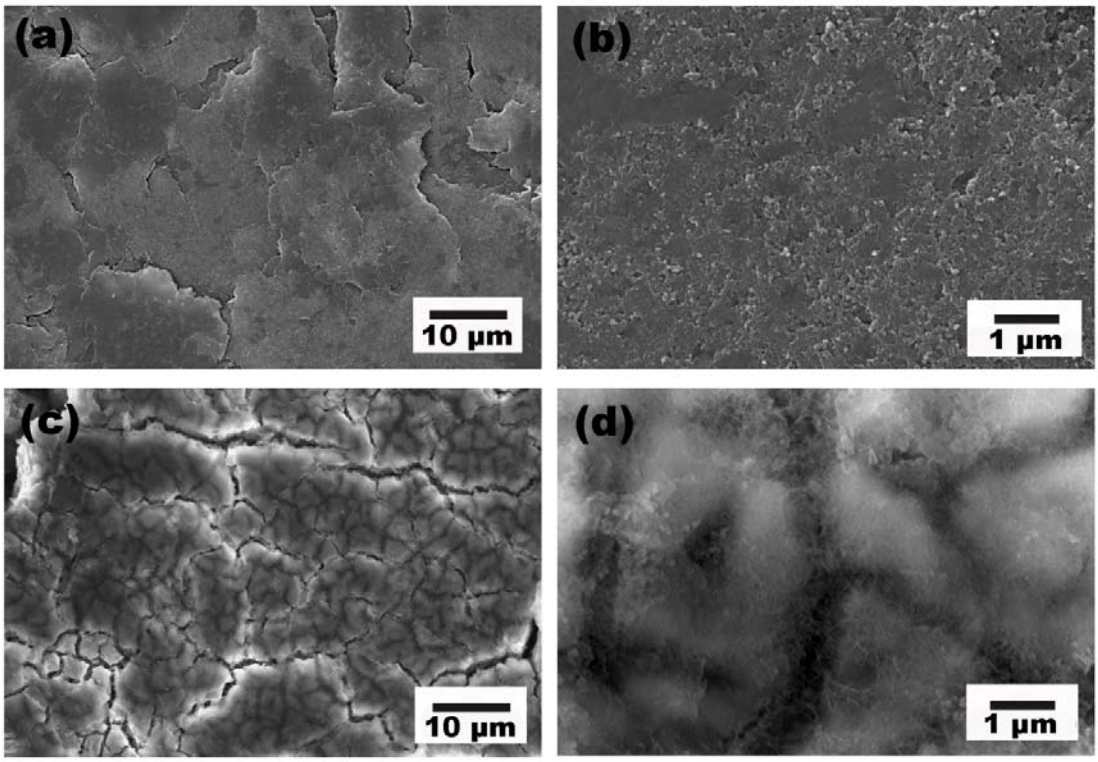

Fig. 7-9 FE-SEM images showing morphologies of the S/GNS nanocomposite electrodes. (a) and (b) are FE-SEM images before cycling test; (c) and (d) are FE-SEM images after 100 cycles.

the volume expansion during charge/discharge of sulfur, which arises from the transformation of elemental sulfur to polysulfide and the accumulation of an irreversible Li_2S phase.[204] At higher magnification (**Fig. 7-9(d)**), it can be seen that there is no obvious damage or collapse on the surface of the cycled electrode, which means that an integrated electrode structure has been preserved throughout the long term cycling. A few graphene nanosheets are visibly exposed due to the extrusion process that results from the volume expansion. Also, the S/GNS electrode fractures slightly and the aggregation of sulfur particles on the electrode becomes more intense. Both of these factors could be responsible for the decay in capacity as the cycling proceeds. Nevertheless, the integrity of the S/GNS nanocomposite electrode is well maintained, and this should be attributed to the cushion effect of the graphene nanosheet matrix. The flexible graphene nanosheets alleviate the side effects of volume expansion and therefore significantly enhance the electrochemical performance of lithium-sulfur cells.

7.4 Conclusions

S/GNS nanocomposite material has been prepared by means of a melting process. The as-prepared S/GNS nanocomposite exhibited initial lithium storage capacities of 1505, 1201, 950 mAh g^{-1} at 0.05, 1, and 2 C, respectively, and maintained good cyclability. The improvement of the capacity and cycle life could be ascribed to the dual functions of graphene nanosheets, which provide both electrical conduction and a buffer effect for sulfur electrodes. These effects were confirmed by AC impedance measurements and FE-SEM analysis on the cycled S/GNS nanocomposite electrode. The EDX mapping showed the homogeneous distribution of sulfur on the graphene nanosheet matrix. The sandwich-type architecture of the S/GNS nanocomposite material can help overcome

the major disadvantages of lithium-sulfur batteries and increase capacity very close to the theoretical capacity of sulfur. S/GNS nanocomposite material can significantly enhance the capacity and cyclability of lithium-sulfur batteries.

Chapter Eight

Graphene-Supported SnO_2 Nanoparticles Prepared by a Solvothermal Approach for an Enhanced Electrochemical Performance in Lithium-Ion Batteries

Chapter 8 — Graphene-Supported SnO_2 Nanoparticles Prepared by a Solvothermal Approach for an Enhanced Electrochemical Performance in Lithium-Ion Batteries

8.1 Introduction

SnO_2 has been examined as an anode material for lithium-ion batteries and has a high theoretical capacity of 782 mAh g^{-1}.[134] SnO_2 forms metal alloys when reacting with lithium, leading to reversible transformations between lithium tin alloys (Li_xSn) and tin metal when the lithiation and delithiation proceed. However, the capacity of a bulk SnO_2 electrode fades quickly during prolonged cycling.[127] To further improve the electrochemical performance and the cycle life of SnO_2 electrodes for long-term cycling, one approach is to synthesize nanosized SnO_2 crystals with different morphologies, such as nanowires,[205] nanotubes,[206] and mesoporous structures.[207] These nanostructured SnO_2 materials have been reported to deliver greatly enhanced specific capacities over commercial SnO_2 powders with durable cycling stabilities. An alternative approach is to synthesize SnO_2/GNS nanocomposites. This approach has proven feasibility and facilitates mechanical buffering of the volume expansion associated with charge/discharge processes in lithium-ion cells. A variety of methods have been implemented to distribute SnO_2 nanocrystals on graphene nanosheets, including in-situ chemical preparation,[127, 208] a reassembling process,[209] gas-liquid interfacial synthesis,[210] as well as hydrothermal and solvothermal methods.[211, 212]

This chapter reports on employment of a facile solvothermal technique to disperse SnO_2 nanoparticles with a controlled size on graphene nanosheets. The as-prepared SnO_2/GNS nanocomposite showed uniform distribution of SnO_2 nanoparticles and

significantly improved electrochemical properties, compared with bare graphene nanosheets and SnO_2 nanoparticles. The solvothermal approach developed in this investigation could be used for the synthesis of other metal oxide/graphene nanocomposites.

8.2 Experimental

8.2.1 Material Synthesis

GONS powders were prepared via a chemical approach derived from Hummers' method,[36] according to the previously reported procedure.[35] In a typical synthesis process, 40 mg GONS was firstly dispersed in 40 ml ethylene glycol by ultrasonification for 1 h, followed by the addition of 0.1 mmol $SnCl_2 \cdot 2H_2O$ powders. The mixture was vigorously stirred for half an hour, and then transferred to a 50 ml Teflon lined autoclave, which was sealed and maintained in an oven at 160 °C for 6 h. Afterwards, the black precipitates (SnO_2/GNS) were collected, washed with DI water and ethanol to remove the impurities, and isolated by vacuum filtration. The product was then dried in a vacuum oven at 60 °C, and further sintered at 300 °C for 4 h in argon to increase the crystallinity. For comparison, bare SnO_2 nanoparticles were also synthesized by the same experimental procedure without the presence of GONS in the mixture solution.

8.2.2 Material Characterization

The XRD pattern of the as-synthesized material was measured using a Siemens D5000 X-ray diffractometer from 10° to 80° under a scan rate of 1° min^{-1}. The Raman measurement of the SnO_2/GNS nanocomposite was conducted on a confocal Micro Raman Spectrometer with LabRAM HR system using a 632.8 nm He-Ne laser source. The spectra were recorded in the range of 200 to 2000 cm^{-1} with accumulated scans for an enhanced resolution. FE-SEM observations were performed using a Zeiss Supra 55VP FE-SEM with an Oxford energy dispersive spectrometry system. The TEM analysis was carried out using a JEOL 2011 TEM facility. The graphene (carbon) content in the composite material was determined by TGA on a TGA/DTA analyzer (TA Instruments, SDT 2960 module) in air at 10 °C min^{-1} ranging from room temperature to 1000 °C.

8.2.3 Electrochemical Testing

CR2032 coin cells were assembled in an argon-filled glove box (Unilab, MBraun, Germany) in which the levels of moisture and oxygen were controlled to be less than 0.1 ppm. The electrodes were made by mixing 80 wt% SnO_2/GNS active materials, 10 wt% carbon black, and 10 wt% PVdF binder in the NMP solvent to form a slurry. Then, the slurry was coated on copper foil substrates. Lithium foils were used as the negative electrodes. The electrolyte was 1 M $LiPF_6$ in ethylene carbonate and dimethyl carbonate (1:1). CV tests were carried out on an electrochemistry workstation (CHI660D) at a scan rate of 0.1 mV s^{-1} *vs.* Li/Li^+ reference electrode in the voltage range of 0.01 to 3 V. Galvanostatic charge/discharge measurements were conducted on

the Neware battery tester with a current rate of 0.1 C for 100 cycles. Electrochemical impedance spectroscopy was performed on the same electrochemistry workstation. The frequency was set in 0.01 Hz–100 kHz with the amplitude of 5 mV. The charge/discharge performance of bare graphene nanosheets and SnO_2 nanoparticles was also investigated for comparison.

8.3 Results and discussion

Scheme 8-1 shows a schematic diagram of the formation of the SnO_2/GNS nanocomposite. Firstly, Sn^{2+} ions were attracted to GO nanosheets in the ethylene glycol (EG) solution. Then, the anchored Sn^{2+} ions were reduced by EG via the following two-step reactions:

$$2HOCH_2-CH_2OH \rightarrow 2CH_3CHO + 2H_2O \qquad \textbf{(Eq. 8-1)}$$

$$2CH_3CHO + SnCl_2 \rightarrow CH_3CO-COCH_3 + Sn + 2HCl \qquad \textbf{(Eq. 8-2)}$$

Scheme 8-1 Schematic diagram of the formation of SnO_2/GNS nanocomposite.

Simultaneously, GONS were also gradually reduced by EG to form graphene nanosheets. As EG is a mild reducing agent, the reduction processes take a long time (6 h) to complete at high temperature (160 °C). Then, the formed Sn nanoparticles were

further oxidized by oxygen to become SnO_2 nanoparticles during the cooling period. Thus, the SnO_2/GNS nanocomposite was obtained under the assistance of EG which acted as both a dispersing agent and a reducing agent.

XRD patterns of the SnO_2/GNS nanocomposite and graphene are shown in **Fig. 8-1**. In **Fig. 8-1(a)**, X-ray diffraction lines of well-crystallized SnO_2 were indexed to the tetragonal rutile SnO_2 phase, which is consistent with the JCPDS card 01–0657. The weak peak of graphene is also visible at 42° in the composite, which matches the diffraction peak (1 0 0) marked on the XRD pattern of bare graphene nanosheets (as shown in **Fig. 8-1(b)**). XRD confirmed the coexisting phases of rutile SnO_2 and graphene and the formation of SnO_2/GNS nanocomposite.

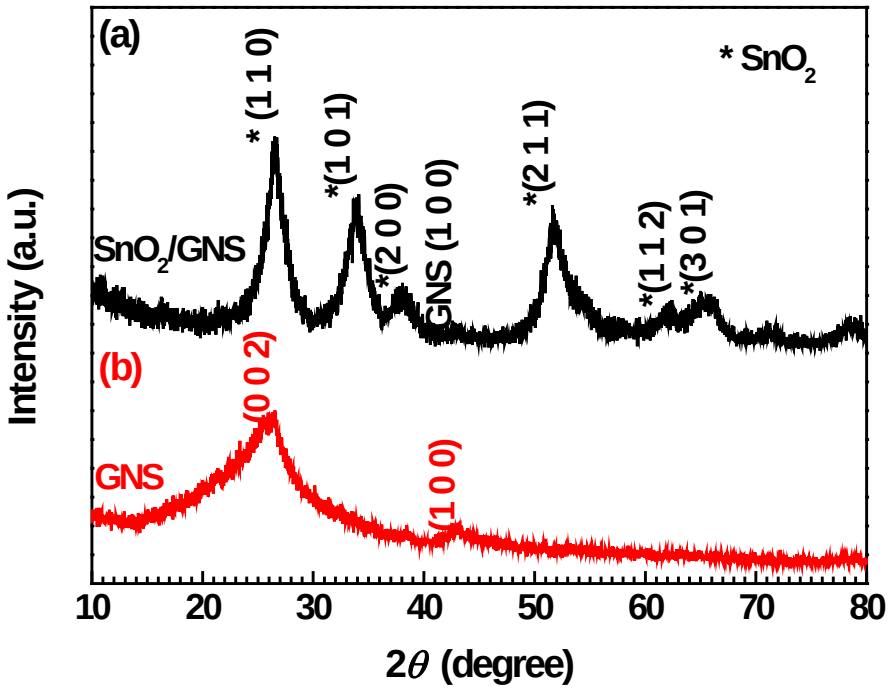

Fig. 8-1 XRD pattern of (a) SnO_2/GNS nanocomposite and (b) GNS.

Raman spectra of the as-prepared SnO_2/GNS nanocomposite and bare GNS are shown in **Fig. 8-2**. It can be seen that both of them show a high-intensity D band around 1327 cm^{-1} and a G band at 1587 cm^{-1}. The D band is stronger than the G band, and the D/G intensity ratio is significantly higher than that of pristine graphite,[34] which both confirm the existence of graphene nanosheets in the composite material. The D/G intensity ratio of the SnO_2/GNS nanocomposite is higher than that of the bare GNS, indicating the sp^2 carbon domains decreased when SnO_2 nanoparticles were inserted between graphene nanosheets.[27] The inset in **Fig. 8-2** displays magnified Raman spectra in the range of 400 to 900 cm^{-1} of both SnO_2/GNS and bare GNS. Two weak peaks were found at 465 and 620 cm^{-1} in the Raman spectrum of the SnO_2/GNS nanocomposite, which can be assigned to the E_g and A_{1g} active modes of SnO_2 crystallines.[213] For the bare GNS, no Raman peak was observed in this range.

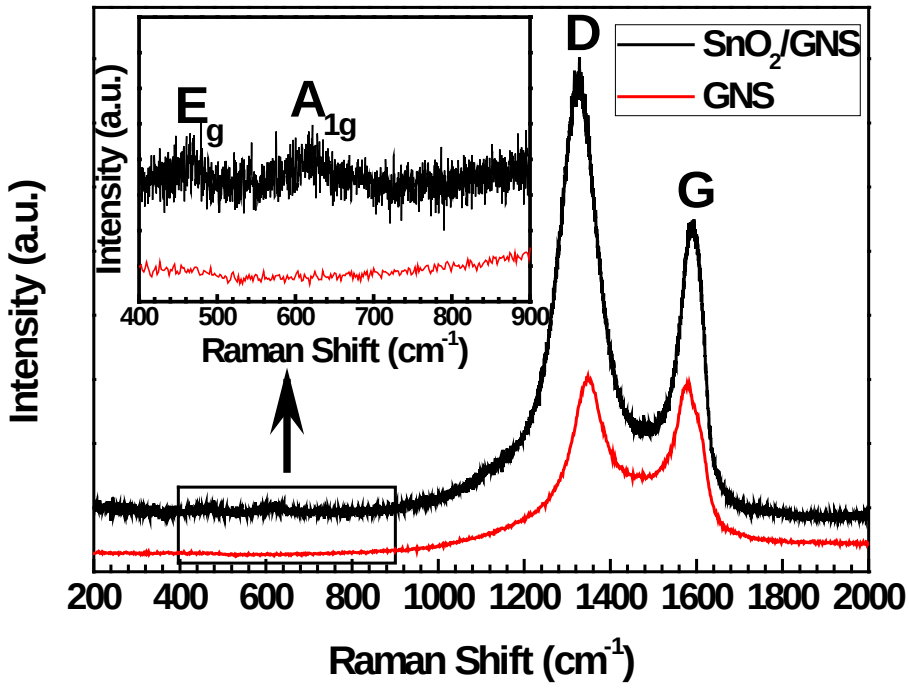

Fig. 8-2 Raman spectra of SnO_2/GNS nanocomposite and bare GNS from 200 to 2000 cm^{-1}. The inset shows magnified views of the spectra in the range of 400 to 900 cm^{-1}.

TGA was employed to determine the weight composition of the SnO_2/GNS nanocomposite (as shown in **Fig. 8-3**). The dramatic weight loss from 500 °C to 630 °C is associated with the burning of graphene in air. SnO_2 in the nanocomposite was stable up to 1000 °C. Therefore, the composition of the SnO_2/GNS nanocomposite was calculated to be 36.3 wt% SnO_2 and 63.7 wt% graphene.

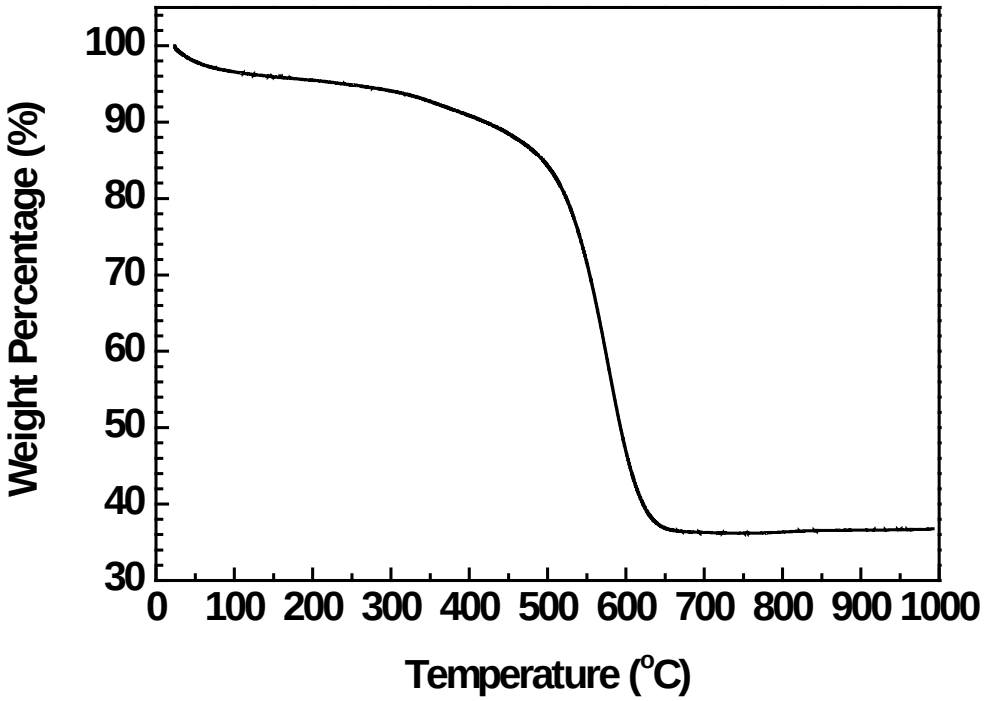

Fig. 8-3 TGA curve of SnO_2/GNS nanocomposite.

Fig. 8-4 displays FE-SEM images of the SnO_2/GNS nanocomposite. Corrugated graphene nanosheets are well expanded and form flower-like nanostructures (**Fig. 8-4(a)**). A magnified FE-SEM view further reveals details of a large, flat graphene nanosheet (**Fig. 8-4(b)**). Tiny SnO_2 nanoparticles were found anchored on this graphene flake. **Fig. 8-5** shows a TEM image of the SnO_2/GNS nanocomposite. Large numbers of

SnO_2 nanoparticles were homogeneously distributed on the graphene nanosheets as shown in **Fig. 8-5(a)**. The inset shows the SAED pattern. The diffraction rings were indexed as the crystal planes (1 1 0), (1 0 1), (2 0 0), (2 1 1), (2 1 0) of SnO_2, which clearly confirms the presence of SnO_2 in the nanocomposite material. HRTEM was performed on a few SnO_2 nanoparticles (**Fig. 8-5(b)**). SnO_2 nanocrystals were densely packed on the surface of graphene nanosheets. Two crystal planes were indexed to be (1 0 0) and (1 1 0) of SnO_2. The particle size of SnO_2 was determined to be around 5 nm.

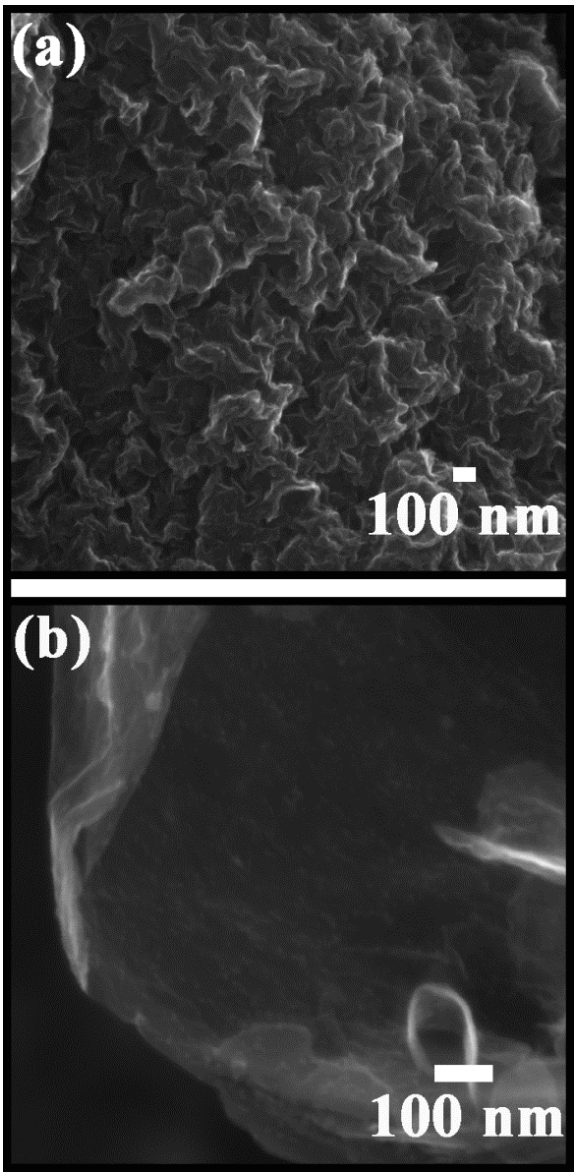

Fig. 8-4 FE-SEM images of SnO_2/GNS nanocomposite: (a) a low magnified image showing flower-like microstructure of graphene nanosheets and (b) a high magnified image focusing on a large graphene flake.

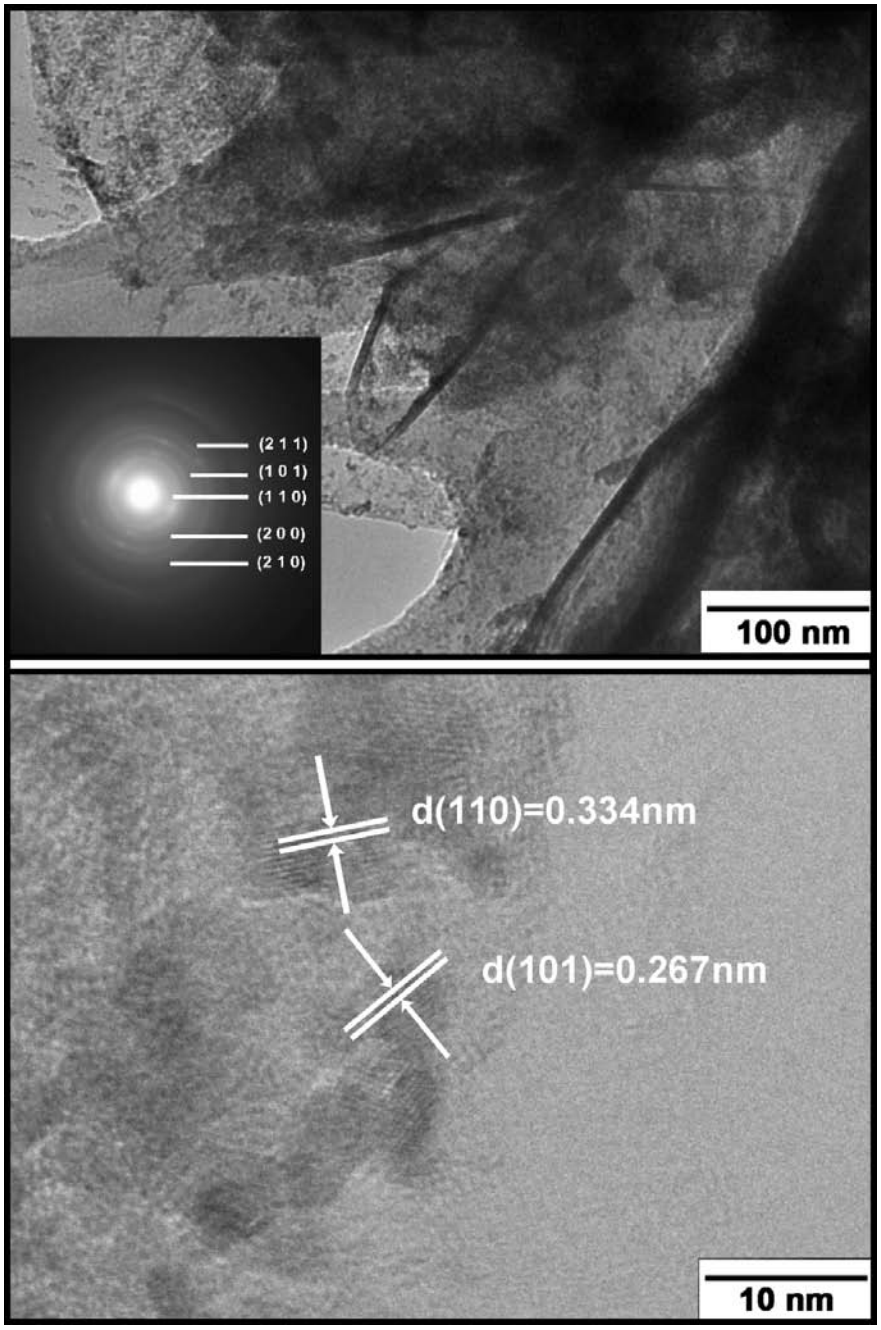

Fig. 8-5 TEM images of SnO_2/GNS nanocomposite: (a) a low magnified image exhibiting homogenous distribution of SnO_2 nanoparticles on graphene nanosheets. The inset shows the corresponding SAED ring pattern, where crystal planes (1 1 0), (1 0 1), (2 0 0), (2 1 1), (2 1 0) of SnO_2 are indexed; (b) an HRTEM image focusing on a few SnO_2 nanoparticles with indexed (1 0 0) and (1 1 0) crystal planes.

Fig. 8-6 presents typical CV characteristics related to the lithiation and delithiation processes of the SnO_2/GNS nanocomposite in the lithium-ion cell. A small cathodic peak appears at 0.8 V in the first cycle attributable to the formation of the SEI layer.

Another small reduction peak located around 0.06 V could be due to the reactions between lithium and SnO_2 nanoparticles to form Li_xSn alloys, whereas the reduction peak at 0.01 V could be identified as the insertion of lithium in graphene nanosheets. There are three oxidation peaks located around 0.13, 0.55, and 1.3 V, respectively. They correspond to different oxidation reactions during the charge process. The first anodic peak at 0.13 V represents the lithium extraction from graphene nanosheets. The 0.55 V oxidation peak can be assigned to the dealloying of Li_xSn, indicating a reversible process. The third weak oxidation at 1.3 V could result from the partial transformation of Sn metal to SnO_2.[107, 214] The high reversibility of the CV curves further confirms the reversible redox reactions occurring in the lithium-ion cell between lithium and SnO_2/GNS nanocomposite.

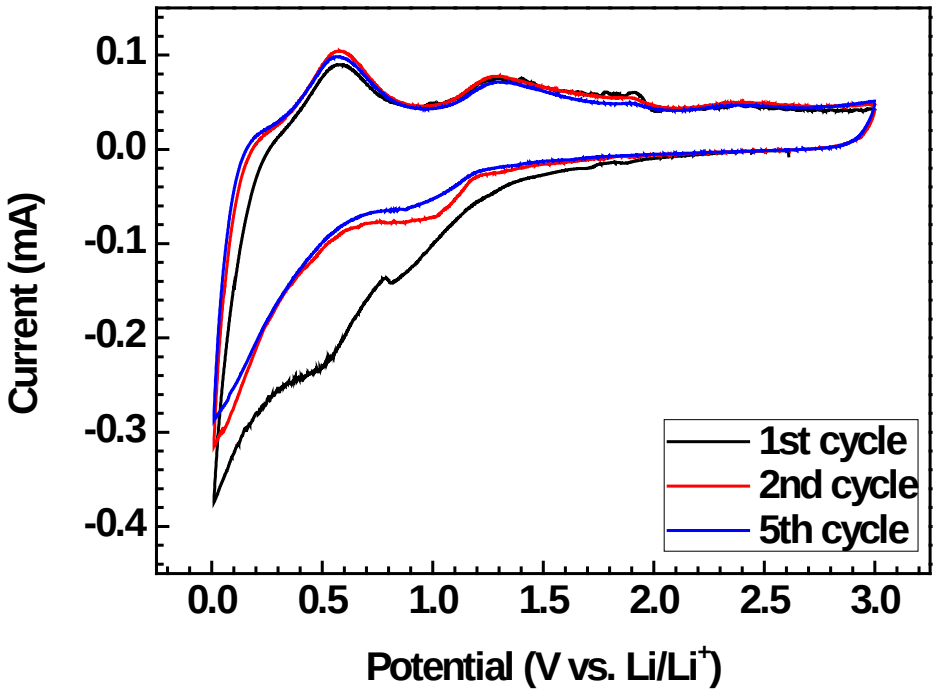

Fig. 8-6 CV curves of the SnO_2/GNS nanocomposite electrode at the 1st, 2nd and 5th cycle at a sweep rate of 0.1 mV s^{-1}.

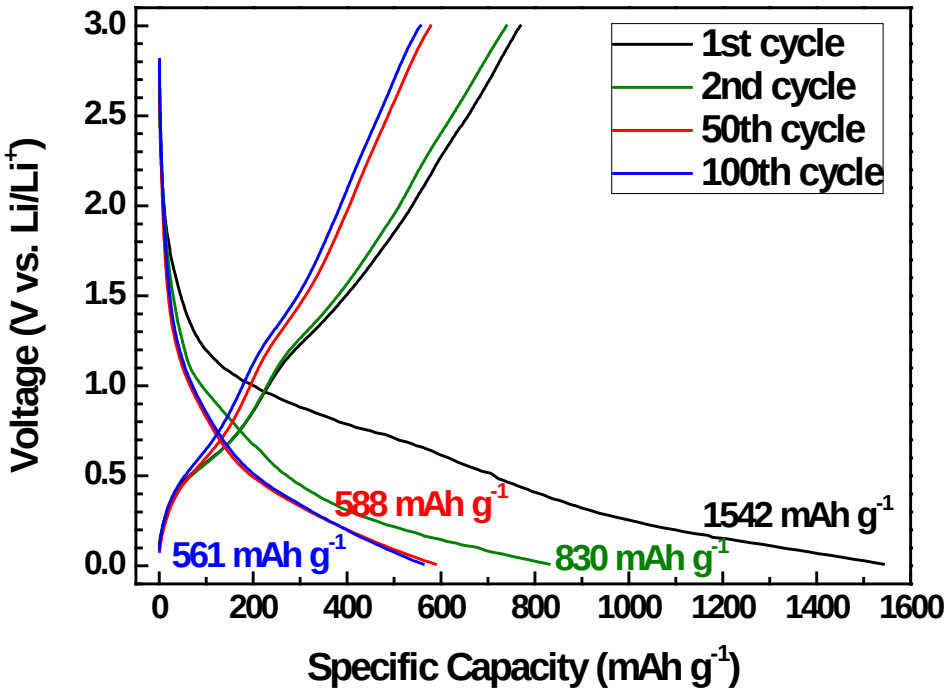

Fig. 8-7 Charge/discharge profiles of the SnO_2/GNS nanocomposite electrode at a current rate of 0.1 C.

Fig. 8-7 shows the charge/discharge profiles of the SnO_2/GNS nanocomposite electrode in different cycles at a current rate of 0.1 C. It can be seen that the SnO_2/GNS electrode delivered a discharge capacity of 1542 mAh g^{-1} in the first cycle. From the second cycle, the nanocomposite electrode exhibited highly reversible charge and discharge capacities. The maximum reversible discharge capacity of 830 mAh g^{-1} was achieved in the second discharge cycle. Specific discharge capacities of 588 and 561 mAh g^{-1} were obtained in the 50th and 100th cycle respectively, which indicates a very stable cycling performance. Significant improvement on the specific capacities has been achieved compared with bulk SnO_2 commercial powders. **Fig. 8-8** shows the long-term cycling properties of the SnO_2/GNS nanocomposite, bare graphene nanosheets and SnO_2 nanoparticles at a 0.1 C current rate. The SnO_2/GNS nanocomposite electrode demonstrated the highest reversible capacities and the best cycling stability. The

nanocomposite electrode delivered a discharge capacity of 1542 mAh g^{-1} in the first cycle and maintained stable capacities from the second cycle for 100 cycles with excellent capacity retention. On the other hand, the bare GNS electrode showed a large irreversible capacity with reversible discharge capacities during the 100 cycles lower than for the composite electrode. The capacities of SnO_2 nanoparticles decrease quickly upon cycling. The retained capacity was less than 30 mAh g^{-1} in the 100th cycle. **Fig. 8-9** demonstrates multiple-step cycling characteristics of the SnO_2/GNS nanocomposite electrode at 0.05 to 0.1, 0.2, 0.5, and 1 C and then reversing back to 0.1 and 0.05 C. The nanocomposite electrode was capable of delivering stable specific capacities at various current rates and could recover substantial capacities without obvious capacity decline when returning to lower current rates. This is indicative of a fully conserved microstructure of the nanocomposite electrode after cycling at higher current rates.

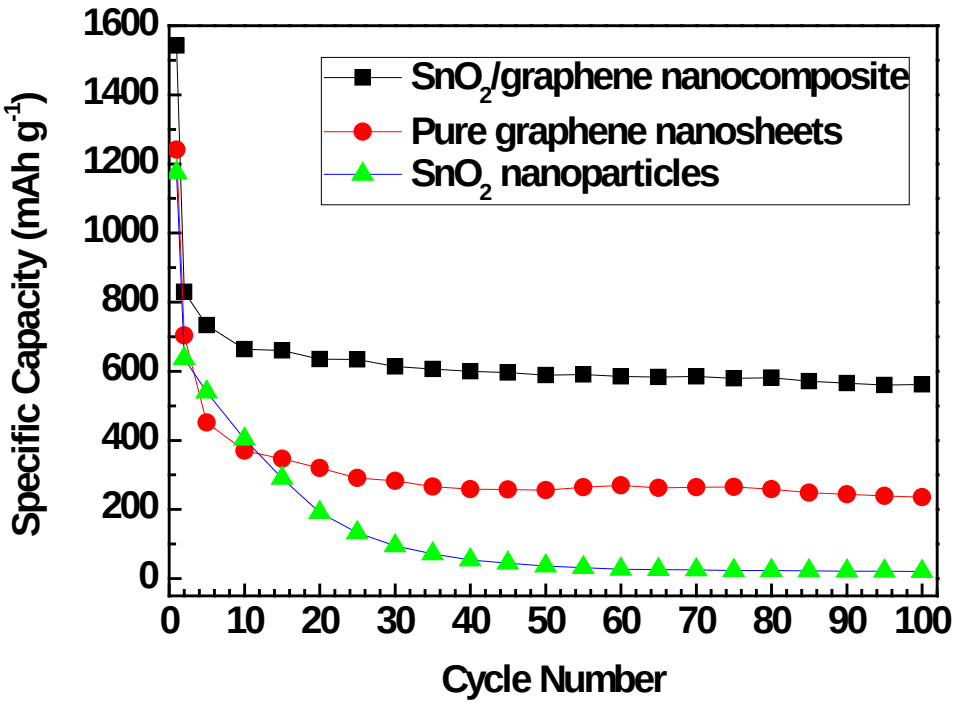

Fig. 8-8 Cycling performances of SnO_2/GNS nanocomposite, GNS, and SnO_2 nanoparticles.

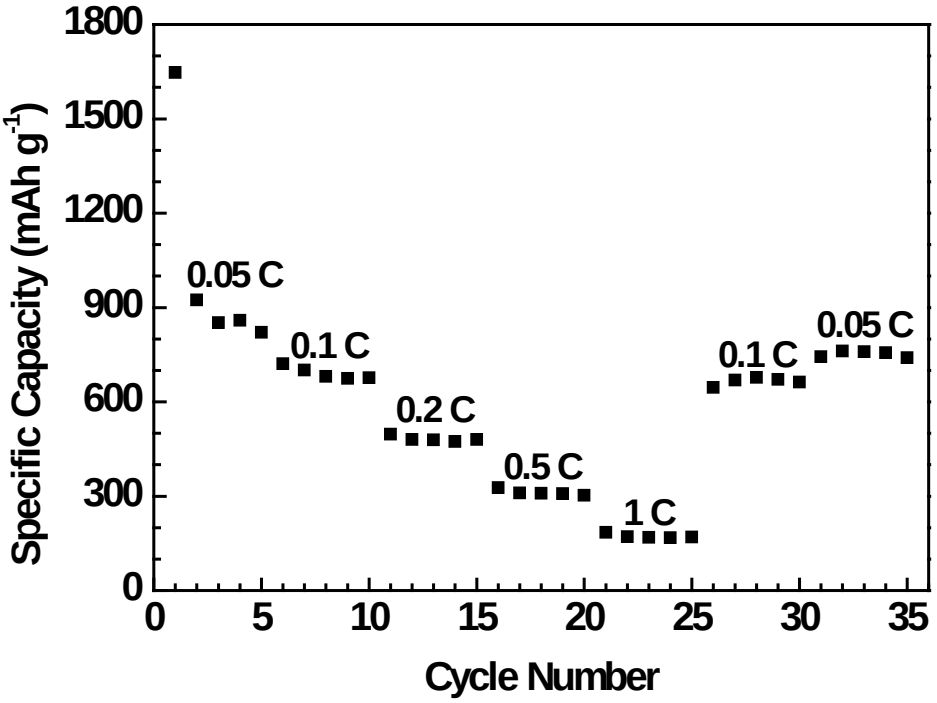

Fig. 8-9 Multiple-step cycling characteristic of the SnO_2/GNS nanocomposite electrode at different current rates.

Fig. 8-10 shows the AC impedance spectra of the SnO_2/GNS nanocomposite electrode before cycling, after 5 cycles and after 100 cycles. The intercept on the *Z*' axis at the high frequency region represents the resistance of the electrolyte (R_s), which is 56.2Ω for a fresh cell. The electrolyte resistance slightly decreased to 35Ω after 5 cycles and remained nearly unchanged after 100 cycles (36.2Ω). The diameters of the semicircles on the spectra imply the charger transfer resistances (R_{ct}) at the electrolyte/electrode interface. It should be noted that the initial charge transfer resistance was 575.9 before it gradually decreased to 242.5 Ω (after 5 cycles) and 95.25 Ω (after 100 cycles) upon prolonged cycling. The significantly decreased charge transfer resistance could be beneficial for an enhanced cycle life of a SnO_2/GNS nanocomposite electrode. The overall electrochemical performance of the SnO_2/GNS nanocomposite was improved compared with bare GNS and SnO_2 nanoparticles as graphene nanosheets supported

SnO_2 nanoparticles on their layered nanostructure. The inserted SnO_2 nanoparticles reduce the stacking degree of graphene nanosheets and also contribute to the reversible lithium storage. Graphene nanosheets in the nanocomposite not only accommodate the volume change associated with the reactions between lithium and SnO_2 nanoparticles, but also provide electrical conductance for the electrodes. The optimized nanoparticle distribution and small particle size of SnO_2 improve the electrochemical properties of the SnO_2/GNS nanocomposite prepared by the solvothermal method over those of SnO_2/GNS nanocomposites prepared by other methods. The well-dispersed SnO_2 nanoparticles effectively prevent the formation of agglomerates on graphene nanosheets, thereby inducing an enhanced electrochemical performance.

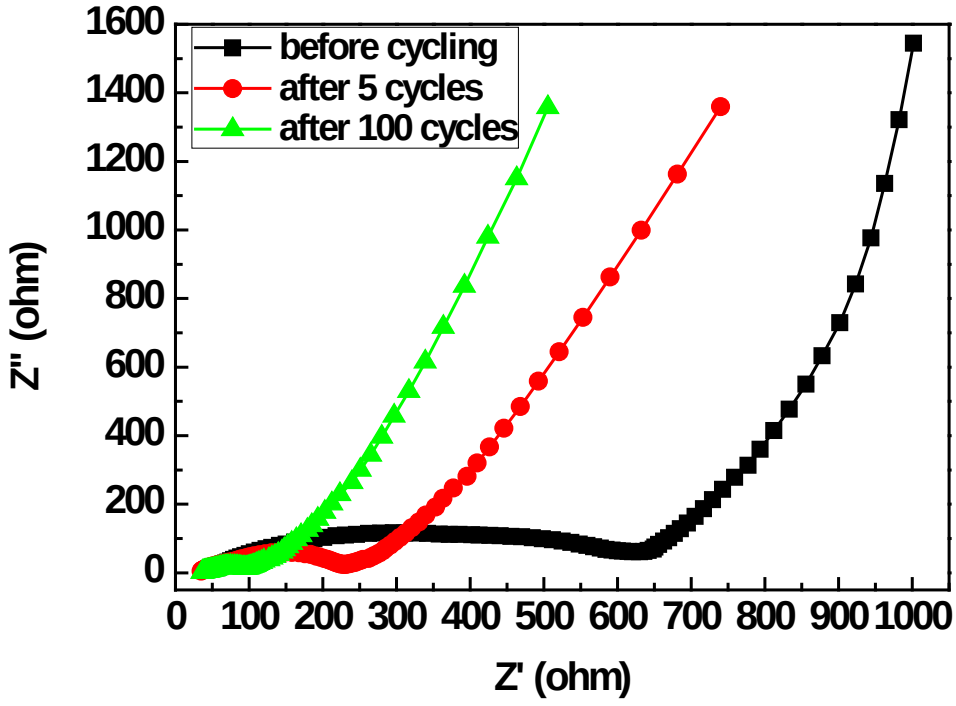

Fig. 8-10 AC impedance spectra of the SnO_2/GNS nanocomposite electrode (a) before cycling, (b) after 5 cycles, and (c) after 100 cycles.

8.4 Conclusions

A facile solvothermal preparation method was developed to synthesize a SnO_2/GNS nanocomposite with a uniform nanoparticle distribution. The as-prepared SnO_2/GNS nanocomposite exhibited improved lithium storage capacity and cycling performance compared to those of bare GNS and bare SnO_2 nanoparticles. The presence of GNS in the nanocomposite could increase the electrical conductivity and buffer the volume expansion associated with the lithiation and delithiation processes, leading to a significantly enhanced electrochemical performance. The solvothermal approach might be applicable for rapid and effective synthesis of other metal oxide/graphene nanocomposites.

Chapter Nine

Solvothermal Synthesis of CoS_2/Graphene Nanocomposite Material for High-Performance Supercapacitors

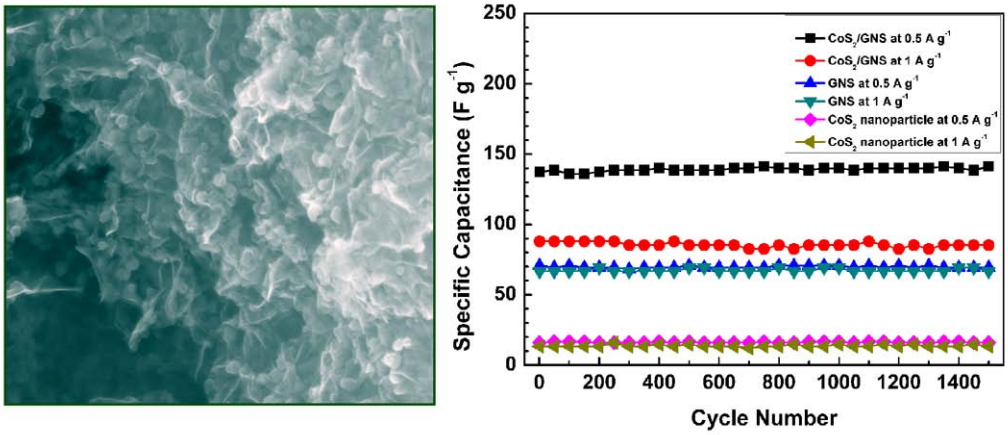

Chapter 9 — Solvothermal Synthesis of CoS_2/Graphene Nanocomposite Material for High-Performance Supercapacitors

9.1 Introduction

Similar to metal oxides, metal sulfides (MSs) are also electrochemically active as electrode materials for supercapacitors.[59-62, 215] They may also be used as spacers to keep graphene nanosheets from stacking. Successful attempts at using metal sulfides for battery applications have been reported: MoS_2/GNS[216-218] and Sn_3S_4/GNS.[219] However, there is no report yet on the application of MS/GNS for supercapacitors. This chapter presents, the first reported, solvothermal synthesis of CoS_2/GNS nanocomposite material for application to supercapacitors. The as-prepared nanocomposite exhibited high supercapacitance and stable capacitance retention in both aqueous and organic electrolytes.

9.2 Experimental

9.2.1 Materials Synthesis

The preparation of CoS_2/GNS was conducted by a facile solvothermal method. In a typical synthesis process, GONS powders were initially prepared by a modified Hummers' method,[36] as previously reported.[35] Then, 80 mg GONS powders were dispersed in a 40 ml mixed solution of DI water and ethylene glycol (3:1 in volume) by ultrasonication, followed by the addition of 0.3 mmol $CoCl_2 \cdot 6H_2O$ and 80 mg *L*-cysteine. The mixture solution was stirred for half an hour and transferred to a 50 ml

Teflon-lined autoclave, sealed and heated in an oven at 160 °C for 6 h. The product was then collected, washed with water and ethanol three times each and dried in a vacuum oven at 60 °C. Finally, the as-prepared CoS_2/GNS was thermal treated at 400 °C for 4 h in argon gas for enhanced crystallinity.

9.2.2 Materials Characterization

The XRD pattern of the as-synthesized material was measured using a Siemens D5000 X-ray diffractometer from 10° to 80° under a scan rate of 1° min^{-1}. The Raman measurements of the CoS_2/GNS nanocomposite were taken on a confocal MICRO Raman Spectrometer with LabRAM HR system using a 632.8 nm He-Ne laser source. The spectra were recorded in the range of 200 to 2000 cm^{-1} with accumulated scans for an enhanced resolution. FE-SEM observations were performed using a Zeiss Supra 55VP FESEM with an Oxford EDS system. The TEM analysis was carried out using a JEOL 2011 TEM facility. N_2 adsorption–desorption isotherms of the CoS_2/GNS nanocomposite were obtained on a TriStar II 3020 Surface Area and Porosity Analyzer at 77 K. The BET surface area was derived by using the experimental points at a relative pressure (P/P_0) of 0.05–0.25. The pore size distribution was plotted by using the BJH method on the desorption isotherm. The graphene (carbon) content in the composite material was determined by TGA on a TGA/DTA analyzer (TA Instruments, SDT 2960 module) in air at 10 °C min^{-1} ranging from room temperature to 1000 °C.

9.2.3 Electrochemical Testing

To prepare the electrodes for supercapacitors, 65 wt% CoS_2/GNS active material, 25 wt%

carbon black and 10 wt% PVdF binder were mixed together and thoroughly grinded. NMP was added to the mixture to form a slurry. Some of the slurry was then pasted on platinum foils and some on nickel foams. The fabricated electrodes were dried under vacuum at 100 °C for 12 h. For the electrochemical tests in an aqueous electrolyte, three-electrode test cells were assembled with a working electrode (a platinum foil with pasted mixture), a reference electrode (SCE), and a counter electrode (a large platinum foil). 6 M KOH aqueous solution was freshly prepared as the electrolyte. CV measurements were conducted from –0.6–0.4 V *vs*. SCE at 5, 10, 20, and 50 mV s^{-1} on an electrochemistry workstation (CHI660D). The galvanostatic charge/discharge characteristics were examined by a chromapermmtery technique on the same electrochemistry workstation. The voltage range was set to be 0–0.35 V with current rates of 0.5 A g^{-1} and 1 A g^{-1} for 1000 cycles. The electrochemical performance of the as-prepared CoS_2/GNS nanocomposite was also evaluated in an organic electrolyte in a two-electrode configuration. Electrodes with identical or similar masses of pasting mixtures on nickel foams were selected for the cell assembly in an argon-filled glove box (Unilab, MBraun, Germany), where the moisture and oxygen contents were controlled to be less than 0.1 ppm. Two electrodes were assembled face-to-face in a coin cell and a glassy fibre was used as the separator. The organic electrolyte was prepared by dissolving 1 M $LiClO_4$ in propylene carbonate (PC) in the same glove box. The galvanostatic charge/discharge performance was tested on a Neware battery tester with current rates of 0.5 A g^{-1} and 1 A g^{-1} respectively. The voltage range was set to be 0–1.5 V for 1500 cycles. For comparison, CoS_2 nanoparticles were prepared via the same experimental procedure, but without the presence of GONS in the mixture solution. Both pure GNS and CoS_2 nanoparticle electrodes were also examined under the same test conditions in aqueous and organic electrolytes.

9.3 Results and Discussion

The chemical reactions between $CoCl_2$ and *L*-cysteine have been previously reported in detail.[60] Co^{2+} ions coordinate with cysteine molecules to form a complex in the mixture solution. The S-H bond of cysteine is gradually weakened by the strong coordination bonds formed by hydrosulfide and Co^{2+}, and is finally broken at high temperature. By controlling the molar ratio of $CoCl_2$ and *L*-cysteine, CoS_2 nanoparticles are obtained. In the mixed solution, ethylene glycol is used, so that while $CoCl_2$ and *L*-cysteine react to produce CoS_2 nanoparticles, GO is simultaneously reduced to graphene, thereby ensuring homogenous distribution of CoS_2 nanoparticles on graphene nanosheets.

Fig. 9-1 shows the XRD patterns of the as-prepared CoS_2/GNS nanocomposite and bare GNS. As shown in **Fig. 9-1(a)**, well-resolved diffraction lines are indexed to the cattierite CoS_2 phase, which is in good agreement with the JCPDS card 89-3056. Two typical diffraction peaks (0 0 2) and (1 0 0) of GNS are also seen in **Fig. 9-1(a)**, which is consistent with the XRD pattern of bare GNS shown in **Fig. 9-1(b)**. The CoS_2/GNS nanocomposite was then characterized by Raman spectroscopy (as shown in **Fig. 9-2**). High-intensity D and G bands are located around 1327 cm^{-1} and 1587 cm^{-1} respectively in the Raman spectra of both CoS_2/GNS and GNS. The D/G intensity ratio was higher than that of pristine graphite,[34] confirming the presence of graphene nanosheets. The D/G intensity ratio of CoS_2/GNS nanocomposite is significantly higher than that of the bare GNS, which indicates a decreased in sp^2 carbon domains,[27] when CoS_2 nanoparticles are embedded between graphene nanosheets.

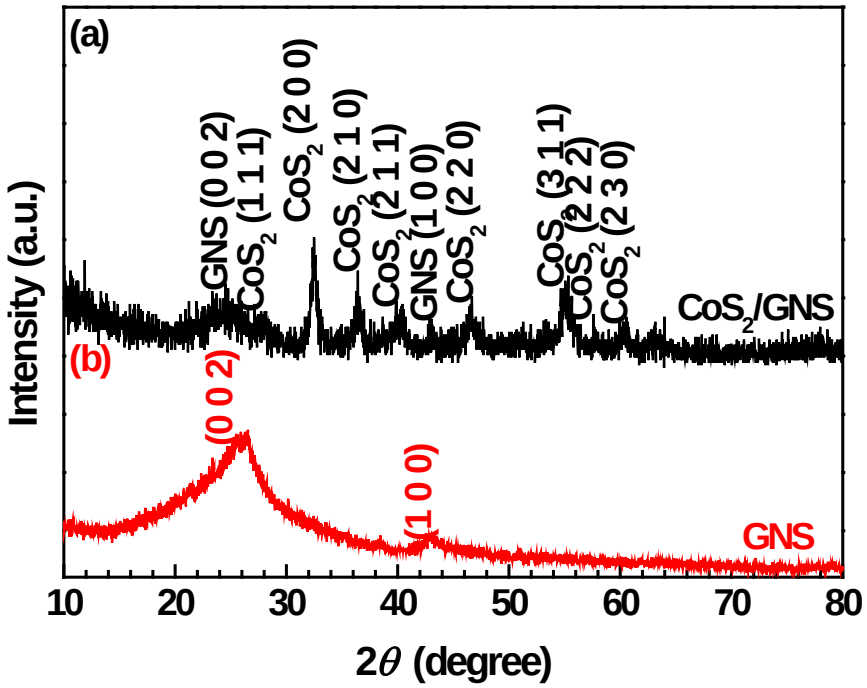

Fig. 9-1 XRD patterns of (a) CoS_2/GNS nanocomposite and (b) bare GNS.

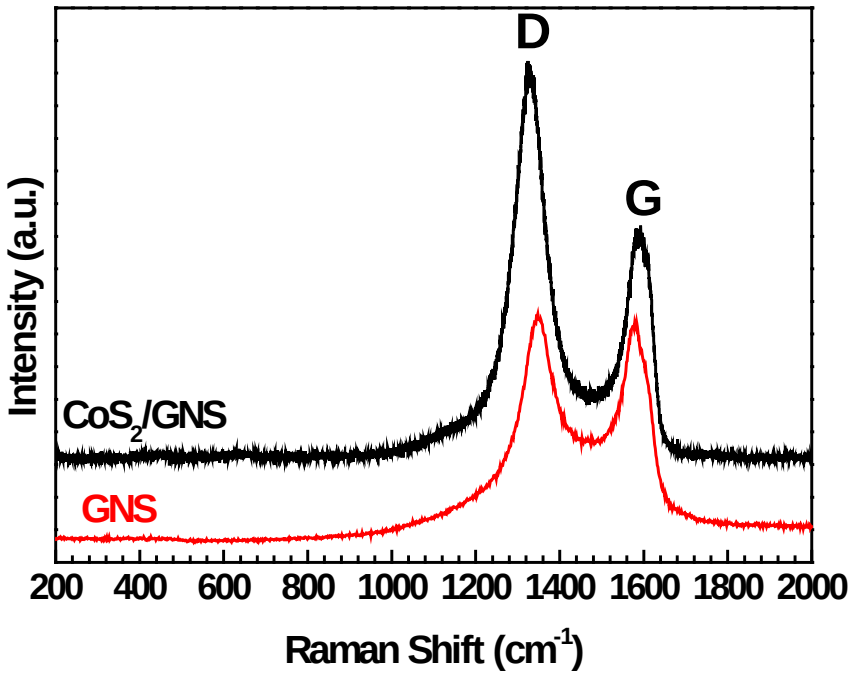

Fig. 9-2 Raman spectra of CoS_2/GNS and bare GNS in the range of 200 to 2000 cm^{-1}.

FE-SEM and TEM observations of the CoS_2/GNS nanocomposite are presented in **Fig. 9-3**. At a low magnification (**Fig. 9-3(a)**), corrugated graphene nanosheets are found to be well expanded caused by the decoration of CoS_2 nanoparticles. These nanoparticles are packed closely to each other and homogeneously distributed on the graphene nanosheets (**Fig. 9-3(b)**). TEM analysis further revealed that CoS_2 nanoparticles are anchored on well-separated graphene nanosheets (as shown in **Fig. 9-3(c)**). The corresponding SAED pattern (inset) indicates the co-existence of both graphene nanosheets and CoS_2 nanoparticles in the nanocomposite. The diffraction

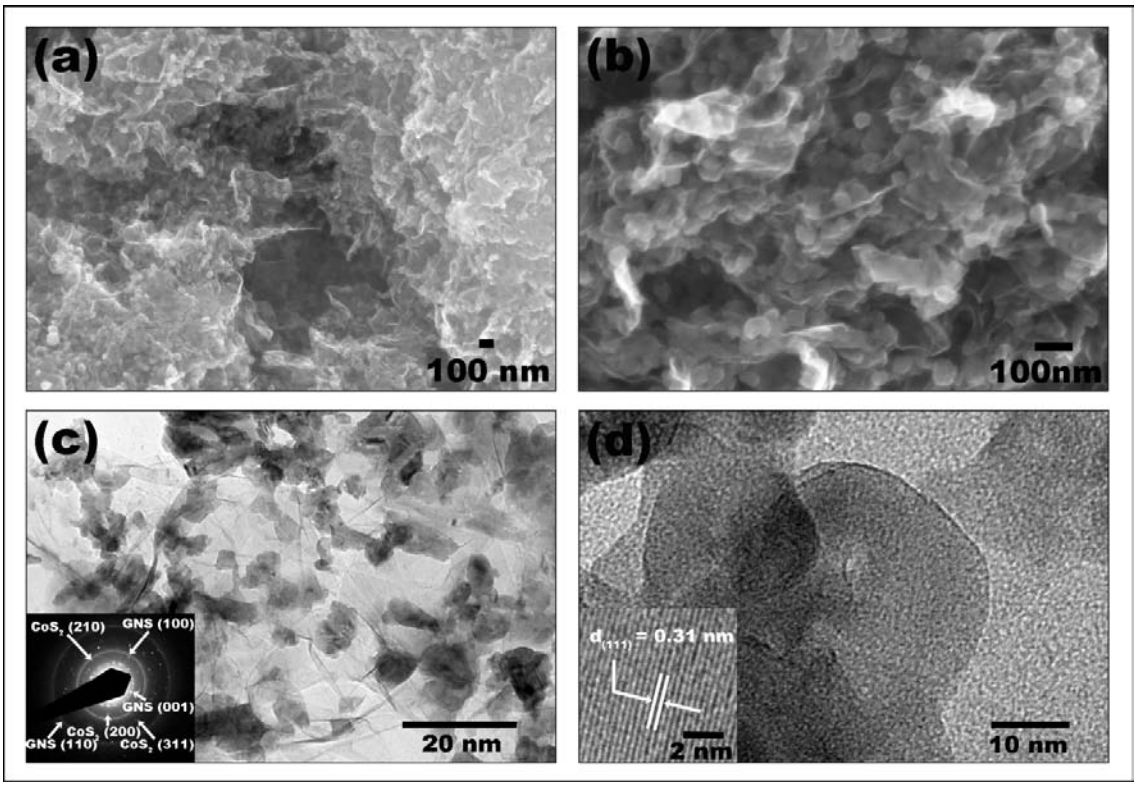

Fig. 9-3 FE-SEM and TEM observations of the CoS_2/GNS nanocomposite: (a) a low magnification SEM image exhibiting general morphology of the nanocomposite; (b) a higher magnification FE-SEM image with detailed CoS_2 nanoparticle distribution, (c) a TEM image showing CoS_2 nanoparticles dispersed on a single graphene nanosheet. The inset shows the SAED pattern with indexed diffraction rings; (d) an HRTEM image presenting lattice-resolved information of CoS_2 nanoparticles. The inset displays the (1 1 1) crystal planes of CoS_2 nanoparticles with a *d*-spacing of 0.31 nm.

rings are indexed to the crystal planes (0 0 1), (1 0 0) and (1 1 0) of graphene and (2 0 0), (2 1 0), and (3 1 1) of CoS_2 nanoparticles, respectively. **Fig. 9-3(d)** shows the lattice resolved HRTEM image of the CoS_2/GNS nanocomposite, in which the (1 1 1) plane of the CoS_2 nanoparticles was determined to be with a 0.31 nm *d*-spacing (as shown in the inset image). The particle size of CoS_2 nanoparticles is about 5–15 nm.

Fig. 9-4(a) exhibits the N_2 adsorption-desorption isotherm of the CoS_2/GNS nanocomposite and the corresponding pore size distribution (inset, **Fig. 9-4(a)**). The specific surface area of the CoS_2/GNS nanocomposite was calculated to be 176 m^2 g^{-1}, based on the BET method. The majority of the pores in the nanocomposite are about 3.18 nm in size, as marked in the inset of **Fig. 9-4(a)**. **Fig. 9-4(b)** shows the TGA graphs of both CoS_2/GNS and bare GNS. The TGA measurements identified the weight losses of both CoS_2/GNS and GNS from room temperature to 1000 °C in air. There are several stages of weight loss for CoS_2/GNS, which could be ascribed to different phase changes in the air atmosphere. However, the weight loss from 500 °C to 630 °C is due to the burning of graphene in air. This is confirmed by the TGA curve of the bare GNS in the same temperature range. Therefore, it can be determined that the weight composition of the CoS_2/GNS nanocomposite is about 42 wt% graphene and 58 wt% CoS_2.

Fig. 9-5(a), (b) and (c) display the CV curves of the CoS_2/GNS nanocomposite, bare GNS and CoS_2 nanoparticle electrodes in 6 M KOH aqueous solution at various scan rates. All the CV curves of the CoS_2/GNS electrode present a rectangular shape in the selected voltage range (as shown in **Fig. 9-5(a)**). The CV curves are highly reversible at different sweep rates and this implies a double layer mechanism of capacitance storage

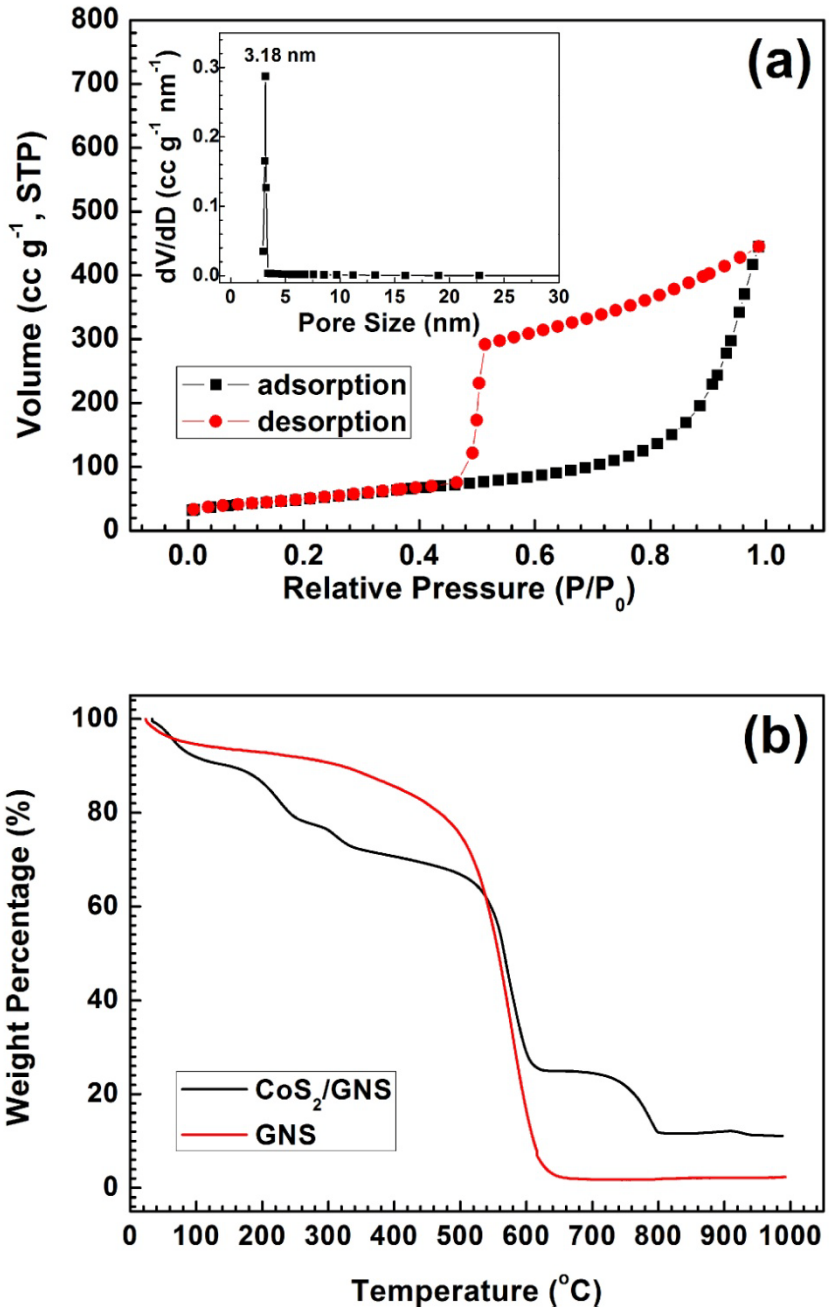

Fig. 9-4 (a) N_2 adsorption–desorption isotherms of the CoS_2/GNS nanocomposite. The inset is the pore size distribution; (b) TGA curves of CoS_2 and GNS in air ranging from room temperature to 1000 °C.

on the nanocomposite electrode in 6 M KOH. The CV curves for the bare GNS electrode (**Fig. 9-5(b)**) are very similar to those for the CoS_2/GNS electrode with a dominant double layer capacitance. However, the CV curves for the bare GNS electrode also show weak redox peaks. The appearance of these redox peaks indicates

pseudocapacitance arising from the functional groups attached to GNS. This phenomenon has been previously reported regarding bare GNS,[167] as discussed in Chapter 5. The oxygen-contained functional groups located at the edges and at the defects of graphene nanosheets provide a hydrophilic surface in the aqueous electrolyte that enhances the double-layer capacitance. The oxygen-contained functional groups also interact with metal ions in the electrolyte providing charge-transfer reactions for pseudocapacitance that contributes to the overall specific capacitance.[220, 221]

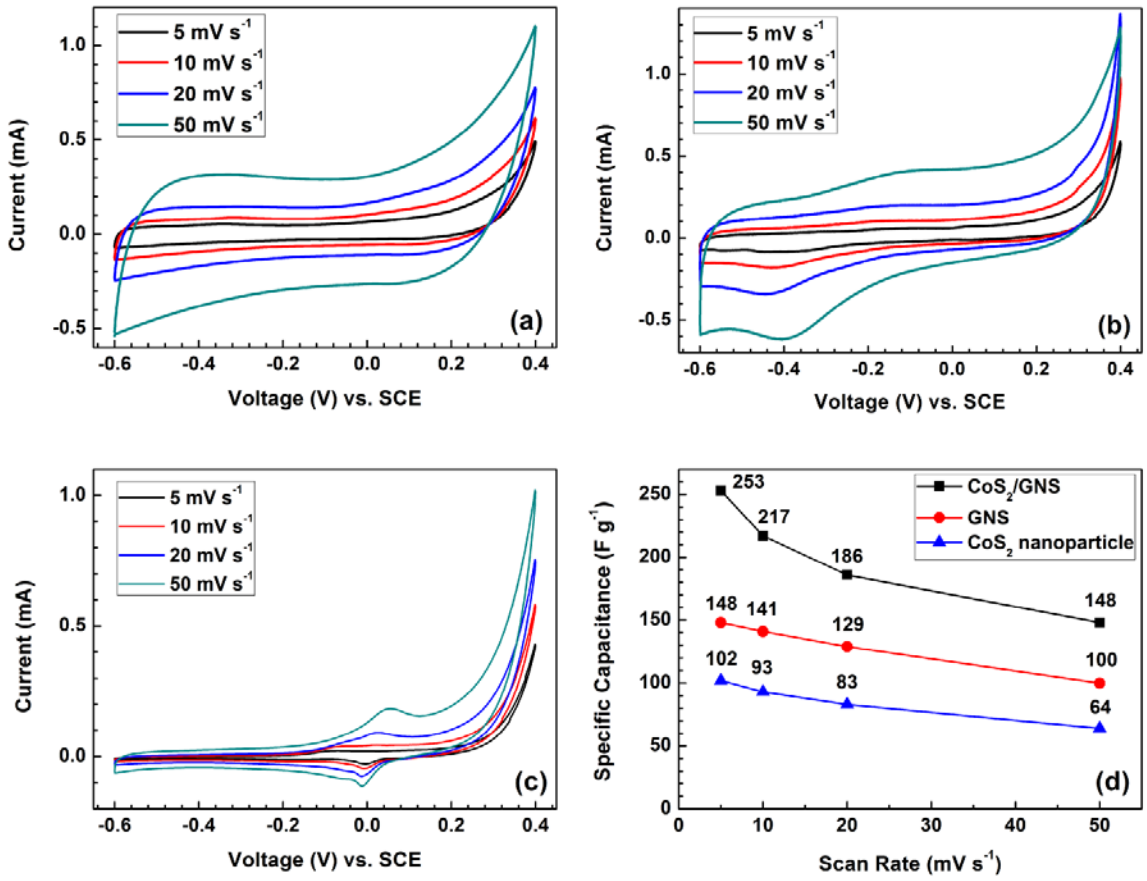

Fig. 9-5 CV curves of (a) CoS_2/GNS, (b) GNS, (c) CoS_2 nanoparticles; and (d) the corresponding specific capacitances at sweep rates of 5, 10, 20, and 50 mV s^{-1} in 6 M KOH solution.

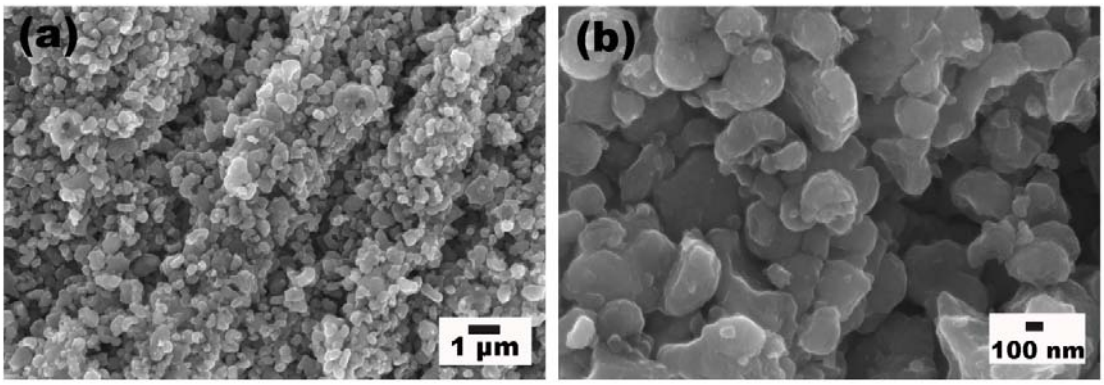

Fig. 9-6 (a) low and (b) high magnified FE-SEM images of the CoS_2 nanoparticles.

To identify the electrochemical activity of bare CoS_2 nanoparticles, CoS_2 nanoparticles with sizes of 100–500 nm (**Fig. 9-6**) were also prepared using the same procedure as that of the CoS_2/GNS nanocomposite. The CV curves of the CoS_2 nanoparticle electrode are shown in **Fig. 9-5(c)**, from which a redox couple can be found in a lower voltage region. The appearance of these redox peaks suggests pseudocapacitance from the redox reactions originated from the CoS_2 nanoparticles. The mechanism for the redox reactions of CoS_2 has not been well studied. However, it has been proposed that cobalt sulfide may have a similar mechanism to $Co(OH)_2$ in alkaline electrolyte due to the similar redox potentials and the fact that sulfur and oxygen are in the same group.[59] Unlike those typical CV curves of CoS reported for supercapacitors,[60, 62] the CoS_2 nanoparticles in this study showed obly one redox couple, which might be related to the following reversible process:

$$CoS_2 + OH^- \leftrightarrow CoS_2OH + H_2O + e^- \qquad \textbf{(Eq. 9-1)}$$

The specific capacitances (calculated from CV curves) *vs.* scan rates are plotted in **Fig. 9-5(d)**. It can be seen that the specific capacitance of all electrodes gradually decreases with the increase in scan rate. The CoS_2/GNS electrode demonstrated the

highest specific capacitance of 253 F g^{-1} at 5 mV s^{-1} and the best performance among all three materials. The bare GNS electrode showed higher capacitance than that of CoS_2 nanoparticles at various scan rates.

Fig. 9-7 shows the charge/discharge profiles of the CoS_2/GNS nanocomposite, bare

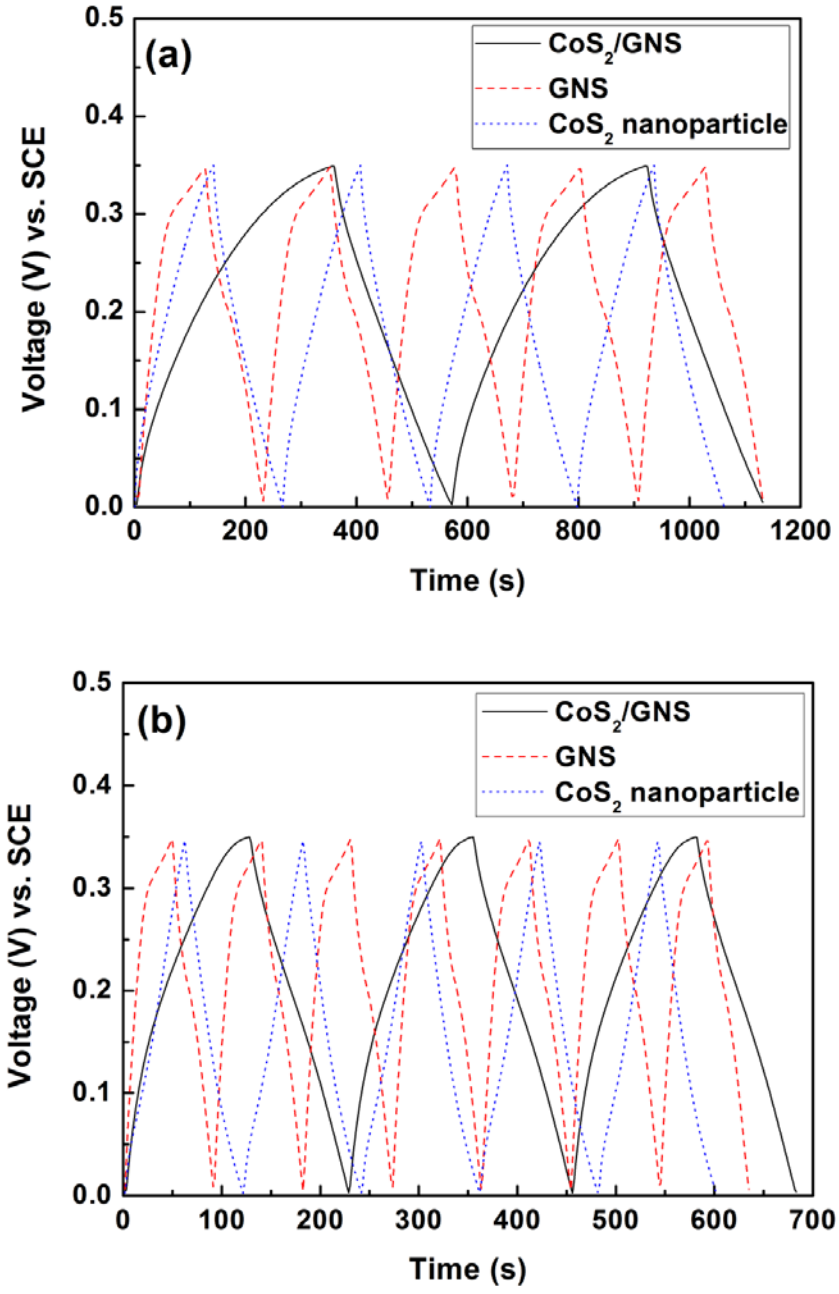

Fig. 9-7 Charge/discharge profiles of CoS_2/GNS, GNS and CoS_2 nanoparticles at (a) 0.5 A g^{-1} and (b) 1 A g^{-1} in 6 M KOH.

GNS and CoS_2 nanoparticle electrodes at 0.5 A g^{-1} and 1 A g^{-1} in 6 M KOH. The working potential was shifted to 0–0.35 V because the CV curves indicated that most of the capacitance of bare CoS_2 nanoparticles is generated in a more positive range. It is expected that the CoS_2/GNS nanocomposite could deliver high specific capacitance because it could utilize pseudocapacitance of the CoS_2 nanoparticles decorating the GNS. All these materials showed highly reversible charge/discharge cycles. The CoS_2/GNS electrode undertook much longer charge/discharge processes than those of the bare GNS and CoS_2 nanoparticle electrodes. This indicates a much higher electric storage capacity of the CoS_2/GNS electrodes. The long-term cycling performance of these three electrodes is shown in **Fig. 9-8**, which exhibits a relationship of specific

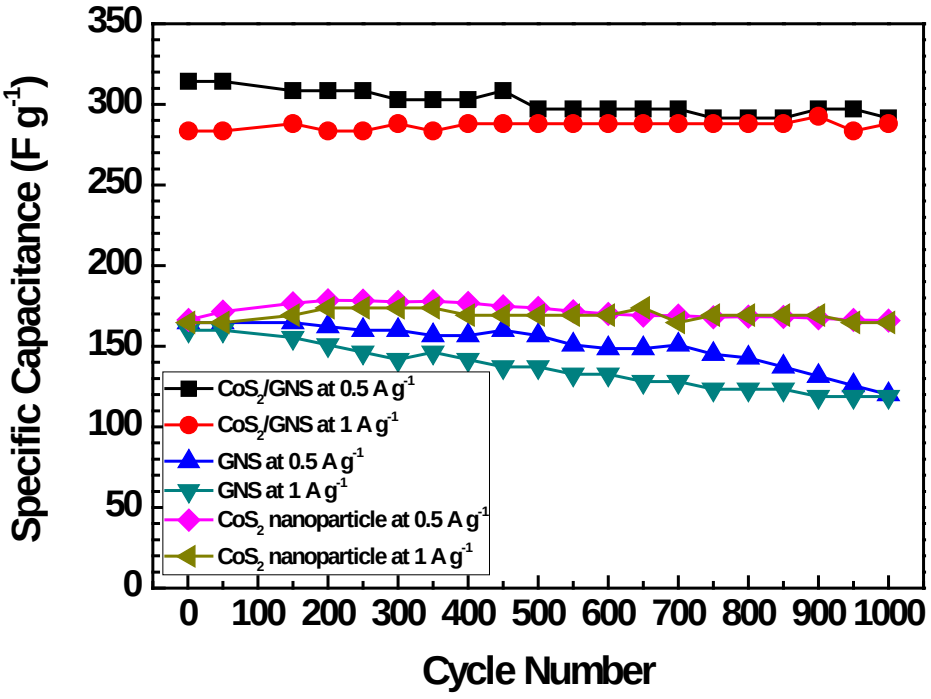

Fig. 9-8 Cycling performances of CoS_2/GNS, GNS and CoS_2 nanoparticles at 0.5 A g^{-1} and 1 A g^{-1} in 6 M KOH for 1000 cycles.

capacitance *vs*. cycle number at current rates of 0.5 A g^{-1} and 1 A g^{-1}. The values of specific capacitance (*C*, F g^{-1}) were calculated based on the discharge stages of the electrodes by applying the following equation:

$$C = \frac{It}{m\Delta V} \qquad \textbf{(Eq. 9-2)}$$

where *I* represents the constant current (A) applied to the charge/discharge processes, *t* is the consumed time (s) for the discharge process, and *m* is the weight (g) of the active material on the electrode, and ΔV is the potential window (V).

It should be noted that the CoS_2/GNS nanocomposite electrode achieved the highest specific capacitances of 314 F g^{-1} at 0.5 Ag^{-1} and 293 F g^{-1} at 1 A g^{-1} in 6 M KOH. These specific capacitances are very stable on cycling for 1000 cycles; outstanding for a practical supercapacitor. For the GNS electrode, the specific capacitance reached the highest values of 164 F g^{-1} at 0.5 A g^{-1} and 160 F g^{-1} at 1 A g^{-1}. However, these capacitances gradually decreased upon continuous cycling. The CoS_2 nanoparticle electrode exhibited maximum specific capacitances of 179 F g^{-1} at 0.5 A g^{-1} and 174 F g^{-1} at 1 A g^{-1}, and retained a better cycling stability than the bare GNS.

The enhancement of the specific capacitance of CoS_2/GNS over GNS and CoS_2 nanoparticles could be credited to various factors. These include the expansion of surface area caused by insertion of CoS_2 nanoparticles between graphene nanosheets; the CoS_2/GNS nanocomposite has a surface are of 179 m^2 g^{-1} whereas the surface area of bare GNS is only 93.7 m^2 g^{-1} (Chapter 5). The enlarged surface area can provide easy access and more space for electrolyte diffusion and further enforce electric storage on the CoS_2/GNS electrodes.[167] Another factor contributing to the enhanced specific capacitance of CoS_2/GNS over GNS and CoS_2 nanoparticles, is that graphene

nanosheets are extremely flexible and therefore generate high reversible capacitance for a durable cycle life. The disadvantage of the bare GNS electrode is that the surface area is quite limited when graphene nanosheets are stacked to multilayers in the dry state and this hinders the diffusion of ions from the electrolyte to the electrodes. A further factor contributing to the enhanced overall capacitance of CoS_2/GNS over GNS and CoS_2 nanoparticles could be the electrochemical active in 6 M KOH of the CoS_2 nanoparticles in the CoS_2/GNS nanocomposite.

Fig. 9-9 illustrates the charge/discharge profiles of CoS_2/GNS, bare GNS and CoS_2 nanoparticle electrodes in the organic electrolyte (1 M $LiClO_4$ in PC) at current rates of 0.5 A g^{-1} and 1 A g^{-1}, respectively. Similar to their capacitive characteristics in 6 M KOH, all the charge/discharge curves present a linear relationship with high reversibility in a voltage range of 1.5 V. The CoS_2/GNS nanocomposite electrode performed much better with longer charge/discharge processes than those of bare GNS and CoS_2 nanoparticle electrodes. The cycling performance of CoS_2/GNS, bare GNS and CoS_2 nanoparticles at different current rates are shown in **Fig. 9-10**. The specific capacitance of a single electrode (*C*, F g^{-1}) is twice the measured capacitance of the cell, and is derived from the following equation in a two-electrode cell configuration:

$$C = \frac{2It}{m\Delta V} \qquad \textbf{(Eq. 9-3)}$$

where *I* represents the constant current (A) applied to the charge/discharge processes, *t* is the consumed time (s) for the discharge process, and *m* is the mean weight (g) of the active material on the selected two electrodes, and ΔV is the potential window (V).

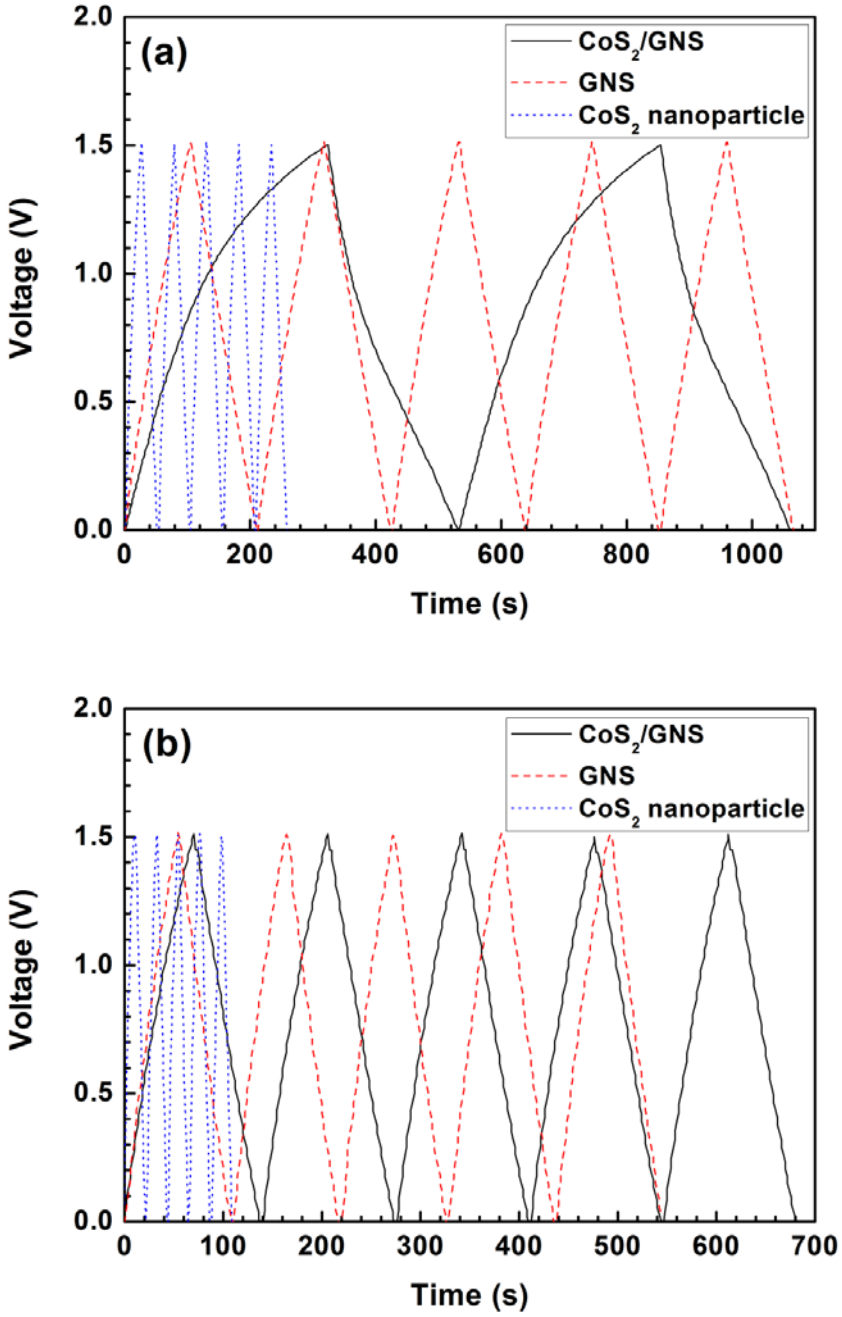

Fig. 9-9 Charge/discharge profiles of CoS_2/GNS, GNS and CoS_2 nanoparticles at (a) 0.5 A g^{-1} and (b) 1 A g^{-1} in 1 M $LiClO_4$ in PC.

In the organic electrolyte, the CoS_2/GNS electrode demonstrated much higher specific capacitances than the bare GNS and CoS_2 nanoparticle electrodes. The maximum specific capacitances of the CoS_2/GNS nanocomposite were 141 F g^{-1} at 0.5 A g^{-1} and

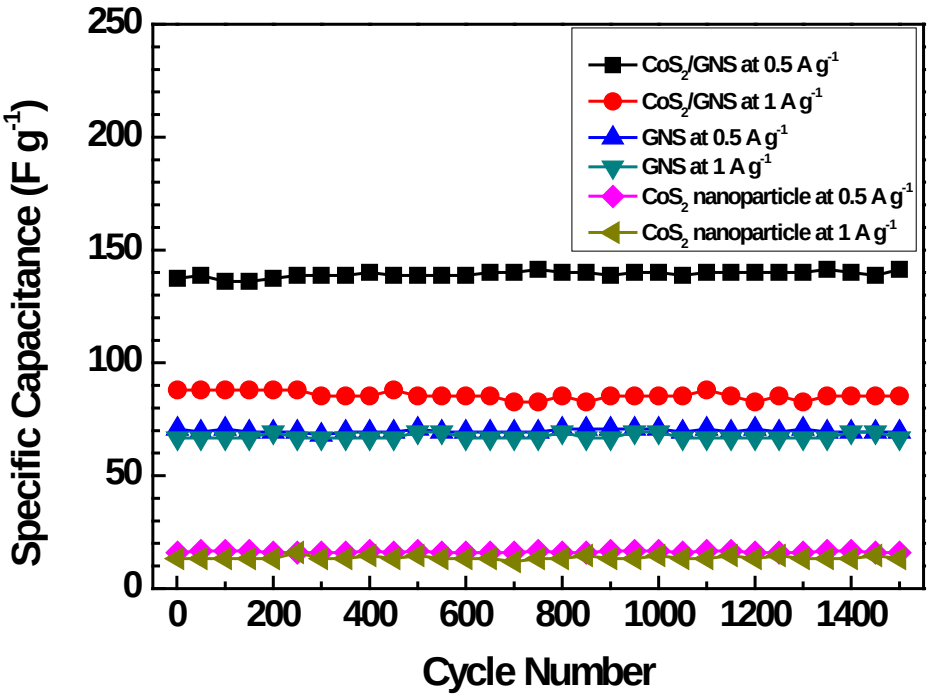

Fig. 9-10 Cycling performances of CoS_2/GNS, GNS and CoS_2 nanoparticles at 0.5 A g^{-1} and 1 A g^{-1}, respectively in 1 M $LiClO_4$ in PC for 1500 cycles.

88 F g^{-1} at 1 A g^{-1}, respectively. The bare GNS showed capacitances of only 71 F g^{-1} at 0.5 A g^{-1} and 69 F g^{-1} at 1 A g^{-1}. Notably, CoS_2 nanoparticles exhibited extremely low capacitances of 17 F g^{-1} at 0.5 A g^{-1} and 15 F g^{-1} at 1 A g^{-1}. The significant capacitive increase of the CoS_2/GNS nanocomposite over the bare GNS and CoS_2 nanoparticle electrodes in the organic electrolyte could also originate from the benefits of the expanded surface area of graphene nanosheets and the extra specific capacitance of the CoS_2 nanoparticles. The specific capacitance of CoS_2/GNS increased significantly when the current rate decreased from 1 A g^{-1} to 0.5 A g^{-1} in both aqueous and organic electrolytes. This is because the decreased current rate allows sufficient time for ions to interact with the huge accessible surface area of graphene nanosheets in the nanocomposite electrode and for the electrode to accumulate the capacitance gradually

over a longer time period. By contrast, the change of current rate from 1 A g^{-1} to 0.5 A g^{-1} leads to no increase in the capacitance of the bare GNS electrode. This could be ascribed to the stacking of individual graphene nanosheets in the bare GNS. Despite the longer charge and discharge time applying at 0.5 A g^{-1}, the accessible surface area for the electrochemical activity on the bare GNS electrode, is still quite limited. Consequently, the capacitance remains comparable to the cycling result obtained at the high current rate of 1 A g^{-1}. For CoS_2 nanoparticles, the aggregation of nanoparticles and large particle size are not favourable for ion diffusion and the interactions with electrolyte, leading to low capacitance. The cycling stabilities of CoS_2/GNS, bare GNS and CoS_2 nanoparticles in the organic electrolyte are better than those in the aqueous electrolyte. All three materials in the organic electrolyte exhibited almost no capacitance fading up to 1500 cycles. This could be due to the optimized test conditions, such as ultra low level of moisture and oxygen in sealed coin cells. However, the specific capacitances of these three materials in the organic electrolyte were lower than those in the aqueous 6 M KOH, due to reduced ionic conductivity in the organic electrolyte.

9.4 Conclusions

CoS_2/GNS nanocomposite was prepared by a solvothermal method, in which 5–15 nm CoS_2 nanoparticles were sandwiched between graphene nanosheets. The as-prepared nanocomposite showed significantly enhanced electrochemical specific capacitances, which reached to 314 F g^{-1} in the aqueous 6 M KOH electrolyte and 141 F g^{-1} in the organic electrolyte at a current rate of 0.5 A g^{-1}. The CoS_2/GNS nanocomposite also demonstrated excellent cycling stabilities in both aqueous and organic electrolytes. The overall electrochemical performance of the CoS_2/GNS nanocomposite has been

drastically improved, compared to that of bare GNS and CoS_2 nanoparticles. The embedded CoS_2 nanoparticles can effectively increase the accessible surface area of graphene nanosheets, facilitate ion diffusion and interactions with electrolyte, and make an additional electrochemical contribution towards the overall specific capacitance. The outstanding electrochemical properties of the CoS_2/GNS nanocomposite may lead to applications for high-performance supercapacitors.

Chapter Ten

General Conclusions

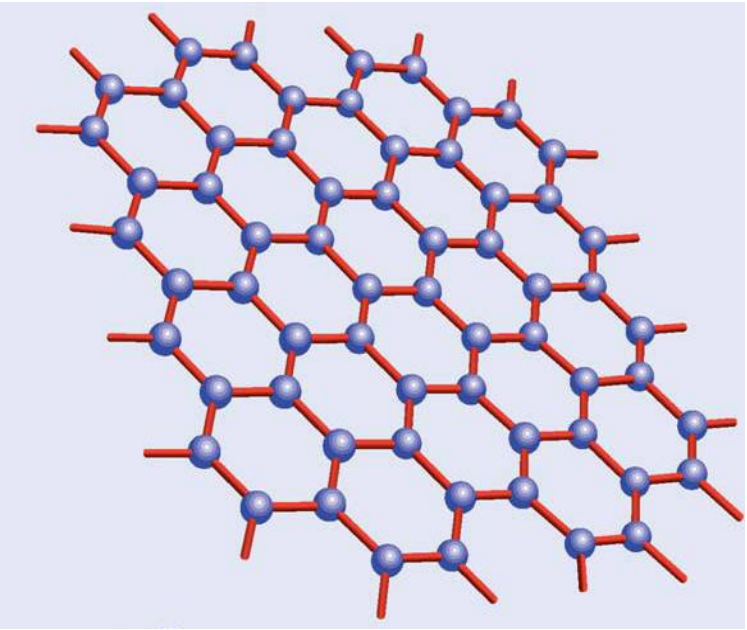

Chapter 10 — General Conclusions

In this thesis, typical graphene-based nanocomposite materials have been intensively studied for energy storage applications: Sn/GNS, Mn_3O_4/GNS, Co_3O_4/GNS, S/GNS, SnO_2/GNS and CoS_2/GNS. Their electrochemical performances in supercapacitors and/or lithium rechargeable batteries have been evaluated individually as detailed in Chapter 4 through to 9.

Sn/GNS with homogeneous distribution of Sn nanoparticles (2–5 nm) on the graphene nanosheet matrix was prepared by an in-situ reduction approach to achieve a 3D nano-architecture, which provides the Sn/GNS electrode with high reversible lithium storage capacity (795 mAh g^{-1} in the second cycle and 508 mAh g^{-1} in the 100th cycle). This indicates a much improved electrochemical performance compared to bare graphene electrode and bare Sn electrode.

Mn_3O_4/GNS was synthesized by mixing MnO_2 organosol and graphene suspension with a post-calcination treatment. The jammed Mn_3O_4 particles were ~10 nm in size, densely distributed on graphene nanosheets. The as-prepared materials exhibited a high specific capacitance of 256 F g^{-1}, which is almost double that of pure graphene nanosheets.

Co_3O_4/GNS, consisting of uniform Co_3O_4 nanoparticles (15–25 nm) distributed on separated graphene nanosheets, was also produced for energy storage applications. The as-prepared Co_3O_4/GNS nanocomposite material exhibited a high lithium storage capacity of 722 mAh g^{-1} in lithium-ion cells and a high supercapacitance of 478 F g^{-1} in supercapacitors, showing significant enhancement on lithium storage and supercapacitance over pure graphene and Co_3O_4 nanoparticles.

S/GNS nanocomposite material was obtained through use of a simple sulfur incorporating technique. The S/GNS nanocomposite material delivered initial lithium storage capacities of 1505, 1201, 950 mAh g^{-1} at 0.05, 1, and 2 C, respectively, and maintained quite good cyclability in lithium-sulfur batteries. The sandwich-type architecture of the S/GNS nanocomposite material was able to help overcome the major disadvantages of lithium-sulfur batteries so that a capacity very close to the theoretical capacity of sulfur could be achieved.

A facile solvothermal preparation method was developed to synthesize SnO_2/GNS nanocomposite with a uniform distribution of SnO_2 nanoparticles (around 5 nm). The as-prepared SnO_2/GNS nanocomposite yielded an improved lithium storage capacity of 830 mAh g^{-1} and enhanced cycling stability for 100 cycles compared to bare GNS and bare SnO_2 nanoparticles.

CoS_2/GNS nanocomposite was prepared by a solvothermal method, in which 5–15 nm CoS_2 nanoparticles were sandwiched between graphene nanosheets. The as-prepared nanocomposite showed high specific capacitances of 314 F g^{-1} in an aqueous 6 M KOH electrolyte and 141 F g^{-1} in an organic electrolyte at a current rate of 0.5 A g^{-1}, with excellent cycling stability in both electrolytes. The overall electrochemical performance of the CoS_2/GNS nanocomposite has been drastically improved, compared to that of bare GNS and CoS_2 nanoparticles.

It can be seen from the above investigations that by decorating graphene nanosheets with nanosized spacers, the formed graphene-based nanocomposites show significantly improved electrochemical properties in energy storage applications than pure graphene. The enhanced electrochemical performance could be owing to four aspects. Firstly, in all cases, graphene plays a crucial role as a highly conducing medium. The addition of

graphene in the composite materials can increase the electrode conductivity and benefit the charge transfer through electrolyte to electrode, therefore leading to much enhanced electrochemical behaviour. This function of graphene worked overwhelmingly well when sulfur was incorporated with graphene; the insulating active material was made alive and the electrochemical performance improved to the point where the achieved capacity was almost equivalent to the high theoretical capacity of sulfur. Secondly, the embedded nanocrystals effectively prevented stacking of graphene nanosheets as expected. This makes single or few layer graphene nanosheets available for access on both sides by active ions, and, increases the specific surface area of graphene to facilitate ion absorption/interactions in supercapacitors and accommodate the volume expansion arising from the lithium insertion and extraction in lithium batteries. Moreover, graphene is able to interfere in the aggregation of nanocrystals and keep them well distributed during materials preparation and also during the electrochemical activity. The separated nanomaterials can protect the electrode from failure during operations, allowing the electrode to achieve a vital cycle life. Last but not least, the nanomaterials themselves are electrochemically active and contribute additional capacitance or capacity towards the total electrochemical properties.

In summary, graphene-based nanocomposite materials have been shown to have many advances over the stacked, pure form of graphene and to have taken advantage of the unique 2D sp^2 bonded carbon atoms of graphene to credit electrochemical performance in future electronic applications. Years of effort have been put into the research and a lot of outcomes related to this topic have been published recently. Nonetheless, the study of nanocomposite materials in this thesis makes only a little step forward towards realization of graphene-based electronic devices. There are other critical issues remaining for consideration, such as compatible electrolytes and well-controlled

technical configurations. However, there is no doubt that graphene has great potential in future energy storage applications as a cheap but outstanding electrode material.

Appendix A List of Acronyms and Abbreviations

0-9

2D — two dimensional

3D — three dimensional

A

AAO — anodized aluminum oxide

AC — alternating current

AFM — Atomic Force Microscope

B

BET — Brunauer-Emmett-Teller

BJH — Barrett-Joyner-Halenda

C

CV — Cyclic Voltammetry

CVD — Chemical Vapor Deposition

D

DI — de-ionized

DME — 1,2-dimethoxyethane

DOX — 1,3-dioxolane

E

EDLCs — electrochemical double layer capacitors

EG — ethylene glycol

EIS — Electrochemical Impedance Spectroscopy

F

FE-SEM — Field-Emission Scanning Electron Microscope

G

GIC — graphite intercalation compound

GNS — graphene nanosheets

GONS — graphene oxide nanosheets

H

HOPG — highly oriented pyrolytic graphite

HRTEM — high-resolution Transmission Electron Microscope

I

IUPAC — International Union of Pure and Applied Chemistry

J

JCPDS — Joint Committee on Powder Diffraction Standards

L

LiTFSI — lithium bis(trifluoromethane sulfon)imide

M

MSs — metal sulfides

N

NMP — *N*-Methyl-2-pyrrolidinone

P

PC — propylene carbonate

PEG — poly(ethylene glycol)

PSS — poly(sodium-4-styrenesulfonate)

PTFE — polytetrafluoroethylene

PVdF — poly(vinylidene difluoride)

S

SAED — Selected Area Electron Diffraction

SCE — Saturated Calomel Electrode

SEI — Solid Electrolyte Interface

SEM — Scanning Electron Microscope

SSA — specific surface area

T

$TBABH_4$ — tetrabutylammonium borohydride

TEGDME — tetra(ethylene glycol) dimethyl ether

TEM — Transmission Electron Microscope

TGA — Thermogravimetric Analysis

TOAB — tetraoctylammonium bromide

U

UTS — University of Technology Sydney

X

XRD — X-ray Diffractometry

Appendix B List of Publications

[1] G.X. Wang, J. Yang, J. Park, X.L. Gou, **B. Wang**, H. Liu, J. Yao, Facile synthesis and characterization of graphene nanosheets, *J. Phys. Chem. C.* 112 (2008) 8192-8195.

[2] G.X. Wang, **B. Wang**, J. Park, J. Yang, X.P. Shen, J. Yao, Synthesis of enhanced hydrophilic and hydrophobic graphene oxide nanosheets by a solvothermal method, *Carbon* 47 (2009) 68-72.

[3] **B. Wang**, K. Konstantinov, D. Wexler, H. Liu, G.X. Wang, Synthesis of nanosized vanadium pentoxide/carbon composites by spray pyrolysis for electrochemical capacitor application, *Electrochim. Acta* 54 (2009) 1420-1425.

[4] G.X. Wang, X.P. Shen, **B. Wang**, J. Yao, J. Park, Synthesis and characterisation of hydrophilic and organophilic graphene nanosheets, *Carbon* 47 (2009) 1359-1364.

[5] G.X. Wang, X.P. Shen, J. Horvat, **B. Wang**, H. Liu, D. Wexler, J. Yao, Hydrothermal synthesis and optical, magnetic, and supercapacitance properties of nanoporous cobalt oxide nanorods, *J. Phys. Chem. C.* 113 (2009) 4357-4361.

[6] G.X. Wang, **B. Wang**, J. Park, Y. Wang, B. Sun, J. Yao, Highly efficient and large-scale synthesis of graphene by electrolytic exfoliation, *Carbon* 47 (2009) 3242-3246.

[7] J. Yao, X.P. Shen, **B. Wang**, H.K. Liu, G.X. Wang, In situ chemical synthesis of SnO_2-graphene nanocomposite as anode materials for lithium-ion batteries, *Electrochem. Commun.* 11 (2009) 1849-1852.

[8] G.X. Wang, **B. Wang**, X.L. Wang, J. Park, S.X. Dou, H. Ahn, K. Kim, Sn/graphene nanocomposite with 3D architecture for enhanced reversible lithium storage in lithium ion batteries, *J. Mater. Chem.* 19 (2009) 8378-8384.

[9] **B. Wang**, J. Park, C.Y. Wang, H. Ahn, G.X. Wang, Mn_3O_4 nanoparticles embedded into graphene nanosheets: preparation, characterization, and electrochemical properties for supercapacitors, *Electrochim. Acta* 55 (2010) 6812-6817.

[10] G.X. Wang, H. Liu, J. Horvat, **B. Wang**, S.Z. Qiao, J. Park, H. Ahn, Highly ordered mesoporous cobalt oxide nanostructure: synthesis, characterisation, magnetic properties, and applications for electrochemical energy devices, *Chem. Eur. J.* 16 (2010) 11020-11027.

[11] A.R. Ranjbartoreh, **B. Wang**, X.P. Shen, G.X. Wang, Advanced mechanical properties of graphene paper, *J. Appl. Phys.* 109 (2011) 014306.

[12] **B. Wang**, Y. Wang, J. Park, H. Ahn, G.X. Wang, In situ synthesis of Co_3O_4/graphene nanocomposite material for lithium ion batteries and supercapacitors with high capacity and supercapacitance, *J. Alloys Compd.* 509 (2011) 7778-7783.

[13] B. Sun, **B. Wang**, D.W. Su, L. Xiao, H. Ahn, G.X. Wang, Graphene nanosheets as cathode catalysts for lithium-air batteries with an enhanced electrochemical performance, *Carbon* 50 (2012) 727-733.

[14] K.F. Li, **B. Wang**, D.W. Su, J. Park, H. Ahn, G.X. Wang, Enhance electrochemical performance of lithium sulfur battery through a solution-based processing technique, *J. Power Sources* 202 (2012) 389-393.

[15] **B. Wang**, K.F. Li, D.W. Su, H. Ahn, G.X. Wang, Superior electrochemical performance of sulfur/graphene nanocomposite material for high capacity lithium sulfur batteries, *Chem. Asian. J.* 7 (2012) 1637-1643.

[16] **B. Wang**, D.W. Su, J. Park, H. Ahn, G.X. Wang, Graphene-supported SnO_2 nanoparticles prepared by a solvothermal approach for an enhanced electrochemical performance in lithium-ion batteries, *Nanoscale Res. Lett.* 7 (2012) 215.

[17] **B. Wang**, J. Park, D.W. Su, H. Ahn, G.X. Wang, Solvothermal synthesis of CoS_2/graphene nanocomposite material for high-performance supercapacitors, *J. Mater. Chem.* 22 (2012) 15750-15756.

[18] T.-F. Hung, **B. Wang**, C.-W. Tsai, M.-H. Tu, G.X. Wang, R.-S. Liu, D.P. Tsai, M.-Y. Lo, D.-S. Shy, X.-K. Xing, Sulfonation of graphene nanosheet-supported platinum via a simple thermal-treatment toward its oxygen reduction activity in acid medium, *Int. J. Hydrogen Energy* 37 (2012) 14205-14210.

[19] A.K. Mondal, **B. Wang**, D.W. Su, Y. Wang, X.G. Zhang, G.X. Wang, Preparation and enhanced electrochemical performance of MnO_2 nanosheets for supercapacitors, *J. Chin. Chem. Soc.* 59 (2012) 1275-1279.

References

[1] Q. Schiermeier, J. Tollefson, T. Scully, A. Witze, O. Morton, Electricity without Carbon, *Nature*, 454 (2008) 816-823.

[2] D. Lindley, The Energy Storage Problem, *Nature*, 463 (2010) 18-20.

[3] C.J. Brabec, N.S. Sariciftci, J.C. Hummelen, Plastic Solar Cells, *Adv. Funct. Mater.*, 11 (2001) 15-26.

[4] W.U. Huynh, J.J. Dittmer, A.P. Alivisatos, Hybrid Nanorod-Polymer Solar Cells, *Science*, 295 (2002) 2425-2427.

[5] B.C.H. Steele, A. Heinzel, Materials for Fuel-Cell Technologies, *Nature*, 414 (2001) 345-352.

[6] J.M. Tarascon, M. Armand, Issues and Challenges Facing Rechargeable Lithium Batteries, *Nature*, 414 (2001) 359-367.

[7] P. Poizot, S. Laruelle, S. Grugeon, L. Dupont, J.M. Tarascon, Nano-Sized Transition-Metaloxides as Negative-Electrode Materials for Lithium-Ion Batteries, *Nature*, 407 (2000) 496-499.

[8] R. Kotz, M. Carlen, Principles and Applications of Electrochemical Capacitors, *Electrochim. Acta*, 45 (2000) 2483-2498.

[9] A.S. Arico, P. Bruce, B. Scrosati, J.M. Tarascon, W. Van Schalkwijk, Nanostructured Materials for Advanced Energy Conversion and Storage Devices, *Nat. Mater.*, 4 (2005) 366-377.

[10] S. Stankovich, D.A. Dikin, G.H.B. Dommett, K.M. Kohlhaas, E.J. Zimney, E.A. Stach, R.D. Piner, S.T. Nguyen, R.S. Ruoff, Graphene-Based Composite Materials, *Nature*, 442 (2006) 282-286.

[11] A.H. Castro Neto, F. Guinea, N.M.R. Peres, K.S. Novoselov, A.K. Geim, The Electronic Properties of Graphene, *Rev. Mod. Phys.*, 81 (2009) 109-162.

[12] A.K. Geim, K.S. Novoselov, The Rise of Graphene, *Nat. Mater.*, 6 (2007) 183-191.

[13] G. Wang, H. Liu, J. Liu, S. Qiao, G.M. Lu, P. Munroe, H. Ahn, Mesoporous $LiFePO_4$/C Nanocomposite Cathode Materials for High Power Lithium Ion Batteries with Superior Performance, *Adv. Mater.*, 22 (2010) 4944-4948.

[14] K.S. Novoselov, A.K. Geim, S.V. Morozov, D. Jiang, Y. Zhang, S.V. Dubonos, I.V. Grigorieva, A.A. Firsov, Electric Field Effect in Atomically Thin Carbon Films, *Science*, 306 (2004) 666-669.

[15] A.C. Neto, F. Guinea, N.M.R. Peres, Drawing Conclusions from Graphene, *Phys. World*, 19 (2006) 33-37.

[16] K.S. Novoselov, A.K. Geim, S.V. Morozov, D. Jiang, M.I. Katsnelson, I.V. Grigorieva, S.V. Dubonos, A.A. Firsov, Two-Dimensional Gas of Massless Dirac Fermions in Graphene, *Nature*, 438 (2005) 197-200.

[17] Y.B. Zhang, Y.W. Tan, H.L. Stormer, P. Kim, Experimental Observation of the Quantum Hall Effect and Berry's Phase in Graphene, *Nature*, 438 (2005) 201-204.

[18] A. Altland, Low-Energy Theory of Disordered Graphene, *Phys. Rev. Lett.*, 97 (2006) 236802.

[19] J.C. Meyer, A.K. Geim, M.I. Katsnelson, K.S. Novoselov, T.J. Booth, S. Roth, The Structure of Suspended Graphene Sheets, *Nature*, 446 (2007) 60-63.

[20] F. Schedin, A.K. Geim, S.V. Morozov, E.W. Hill, P. Blake, M.I. Katsnelson, K.S. Novoselov, Detection of Individual Gas Molecules Adsorbed on Graphene, *Nat. Mater.*, 6 (2007) 652-655.

[21] H.B. Heersche, P. Jarillo-Herrero, J.B. Oostinga, L.M.K. Vandersypen, A.F. Morpurgo, Bipolar Supercurrent in Graphene, *Nature*, 446 (2007) 56-59.

[22] B. Lang, Leed Study of Deposition of Carbon on Platinum Crystal-Surfaces, *Surf. Sci.*, 53 (1975) 317-329.

[23] H. Shioyama, Cleavage of Graphite to Graphene, *J. Mater. Sci. Lett.*, 20 (2001) 499-500.

[24] V. Huc, N. Bendiab, N. Rosman, T. Ebbesen, C. Delacour, V. Bouchiat, Large and Flat Graphene Flakes Produced by Epoxy Bonding and Reverse Exfoliation of Highly Oriented Pyrolytic Graphite, *Nanotechnology*, 19 (2008) 455601.

[25] A. Shukla, R. Kumar, J. Mazher, A. Balan, Graphene Made Easy: High Quality, Large-Area Samples, *Solid State Commun.*, 149 (2009) 718-721.

[26] S. Stankovich, R.D. Piner, X. Chen, N. Wu, S.T. Nguyen, R.S. Ruoff, Stable Aqueous Dispersions of Graphitic Nanoplatelets Via the Reduction of Exfoliated Graphite Oxide in the Presence of Poly(Sodium 4-Styrenesulfonate), *J. Mater. Chem.*, 16 (2006) 155-158.

[27] S. Stankovich, D.A. Dikin, R.D. Piner, K.A. Kohlhaas, A. Kleinhammes, Y. Jia, Y. Wu, S.T. Nguyen, R.S. Ruoff, Synthesis of Graphene-Based Nanosheets Via Chemical Reduction of Exfoliated Graphite Oxide, *Carbon*, 45 (2007) 1558-1565.

[28] Y. Hernandez, V. Nicolosi, M. Lotya, F.M. Blighe, Z. Sun, S. De, I.T. McGovern, B. Holland, M. Byrne, Y.K. Gun'ko, J.J. Boland, P. Niraj, G. Duesberg, S. Krishnamurthy, R. Goodhue, J. Hutchison, V. Scardaci, A.C. Ferrari, J.N. Coleman, High-Yield Production of Graphene by Liquid-Phase Exfoliation of Graphite, *Nature Nanotech.*, 3 (2008) 563-568.

[29] M. Lotya, Y. Hernandez, P.J. King, R.J. Smith, V. Nicolosi, L.S. Karlsson, F.M. Blighe, S. De, Z. Wang, I.T. McGovern, G.S. Duesberg, J.N. Coleman, Liquid Phase Production of Graphene by Exfoliation of Graphite in Surfactant/Water Solutions, *J. Am. Chem. Soc.*, 131 (2009) 3611-3620.

[30] A. Charrier, A. Coati, T. Argunova, F. Thibaudau, Y. Garreau, R. Pinchaux, I. Forbeaux, J.M. Debever, M. Sauvage-Simkin, J.M. Themlin, Solid-State Decomposition of Silicon Carbide for Growing Ultra-Thin Heteroepitaxial Graphite Films, *J. Appl. Phys.*, 92 (2002) 2479-2484.

[31] C. Berger, Z. Song, T. Li, X. Li, A.Y. Ogbazghi, R. Feng, Z. Dai, A.N. Marchenkov, E.H. Conrad, P.N. First, W.A. de Heer, Ultrathin Epitaxial Graphite: 2d Electron Gas Properties and a Route toward Graphene-Based Nanoelectronics, *J. Phys. Chem. B*, 108 (2004) 19912-19916.

[32] C. Berger, Z. Song, X. Li, X. Wu, N. Brown, C. Naud, D. Mayou, T. Li, J. Hass, A.N. Marchenkov, E.H. Conrad, P.N. First, W.A. de Heer, Electronic Confinement and Coherence in Patterned Epitaxial Graphene, *Science*, 312 (2006) 1191-1196.

[33] D.A. Dikin, S. Stankovich, E.J. Zimney, R.D. Piner, G.H.B. Dommett, G. Evmenenko, S.T. Nguyen, R.S. Ruoff, Preparation and Characterization of Graphene Oxide Paper, *Nature*, 448 (2007) 457-460.

[34] G. Wang, J. Yang, J. Park, X. Gou, B. Wang, H. Liu, J. Yao, Facile Synthesis and Characterization of Graphene Nanosheets, *J. Phys. Chem. C*, 112 (2008) 8192-8195.

[35] G. Wang, X. Shen, J. Yao, J. Park, Graphene Nanosheets for Enhanced Lithium Storage in Lithium Ion Batteries, *Carbo*n, 47 (2009) 2049-2053.

[36] W.S. Hummers, R.E. Offeman, Preparation of Graphitic Oxide, *J. Am. Chem. Soc.*, 80 (1958) 1339-1339.

[37] G. Wang, B. Wang, J. Park, Y. Wang, B. Sun, J. Yao, Highly Efficient and Large-Scale Synthesis of Graphene by Electrolytic Exfoliation, *Carbon*, 47 (2009) 3242-3246.

[38] K.S. Kim, Y. Zhao, H. Jang, S.Y. Lee, J.M. Kim, K.S. Kim, J.H. Ahn, P. Kim, J.Y. Choi, B.H. Hong, Large-Scale Pattern Growth of Graphene Films for Stretchable Transparent Electrodes, *Nature*, 457 (2009) 706-710.

[39] A. Dato, V. Radmilovic, Z. Lee, J. Phillips, M. Frenklach, Substrate-Free Gas-Phase Synthesis of Graphene Sheets, *Nano Lett.*, 8 (2008) 2012-2016.

[40] M. Choucair, P. Thordarson, J.A. Stride, Gram-Scale Production of Graphene Based on Solvothermal Synthesis and Sonication, *Nature Nanotech.*, 4 (2009) 30-33.

[41] L.A. Ponomarenko, F. Schedin, M.I. Katsnelson, R. Yang, E.W. Hill, K.S. Novoselov, A.K. Geim, Chaotic Dirac Billiard in Graphene Quantum Dots, *Science*, 320 (2008) 356-358.

[42] F. Schwierz, Graphene Transistors, *Nature Nanotech.*, 5 (2010) 487-496.

[43] X.M. Sun, Z. Liu, K. Welsher, J.T. Robinson, A. Goodwin, S. Zaric, H.J. Dai, Nano-Graphene Oxide for Cellular Imaging and Drug Delivery, *Nano Res.*, 1 (2008) 203-212.

[44] M.D. Stoller, S. Park, Y. Zhu, J. An, R.S. Ruoff, Graphene-Based Ultracapacitors, *Nano Lett.*, 8 (2008) 3498-3502.

[45] J.-Z. Wang, L. Lu, M. Choucair, J.A. Stride, X. Xu, H.-K. Liu, Sulfur-Graphene Composite for Rechargeable Lithium Batteries, *J. Power Sources*, 196 (2011) 7030-7034.

[46] B. Wang, K. Li, D. Su, H. Ahn, G. Wang, Superior Electrochemical Performance of Sulfur/Graphene Nanocomposite Material for High-Capacity Lithium-Sulfur Batteries, *Chem. Asian J.*, 7 (2012) 1637-1643.

[47] Y. Li, J. Wang, X. Li, D. Geng, R. Li, X. Sun, Superior Energy Capacity of Graphene Nanosheets for a Nonaqueous Lithium-Oxygen Battery, *Chem. Commun.*, 47 (2011) 9438-9440.

[48] B. Sun, B. Wang, D. Su, L. Xiao, H. Ahn, G. Wang, Graphene Nanosheets as Cathode Catalysts for Lithium-Air Batteries with an Enhanced Electrochemical Performance, *Carbon*, 50 (2012) 727-733.

[49] Y. Si, E.T. Samulski, Exfoliated Graphene Separated by Platinum Nanoparticles, *Chem. Mater.*, 20 (2008) 6792-6797.

[50] B.E. Conway, Electrochemical Supercapacitors, Scientific Fundamentals and Technological Applications, Kluwer Acadamic/Plenum, New York, 1999.

[51] H.I. Becker, Low Voltage Electrolytic Capacitor, US Patent 2800616, United States, 1957.

[52] R.A. Rightmire, Electrical Energy Storage Apparatus, US Patent 3288641, United States, 1966.

[53] P. Simon, Y. Gogotsi, Materials for Electrochemical Capacitors, *Nat. Mater.*, 7 (2008) 845-854.

[54] Office of Basic Energy Science, US Department of Energy, Basic Research Needs for Electrical Energy Storage, Washington DC, 2007.

[55] V. Gupta, T. Kusahara, H. Toyama, S. Gupta, N. Miura, Potentiostatically Deposited Nanostructured α-$Co(OH)_2$: A High Performance Electrode Material for Redox-Capacitors, *Electrochem. Commun.*, 9 (2007) 2315-2319.

[56] D.D. Zhao, S.J. Bao, W.H. Zhou, H.L. Li, Preparation of Hexagonal Nanoporous Nickel Hydroxide Film and Its Application for Electrochemical Capacitor, *Electrochem. Commun.*, 9 (2007) 869-874.

[57] D. Choi, G.E. Blomgren, P.N. Kumta, Fast and Reversible Surface Redox Reaction in Nanocrystalline Vanadium Nitride Supercapacitors, *Adv. Mater.*, 18 (2006) 1178-1182.

[58] X. Zhou, H. Chen, D. Shu, C. He, J. Nan, Study on the Electrochemical Behavior of Vanadium Nitride as a Promising Supercapacitor Material, *J. Phys. Chem. Solids*, 70 (2009) 495-500.

[59] F. Tao, Y.-Q. Zhao, G.-Q. Zhang, H.-L. Li, Electrochemical Characterization on Cobalt Sulfide for Electrochemical Supercapacitors, *Electrochem. Commun.*, 9 (2007) 1282-1287.

[60] S.-J. Bao, C.M. Li, C.-X. Guo, Y. Qiao, Biomolecule-Assisted Synthesis of Cobalt Sulfide Nanowires for Application in Supercapacitors, *J. Power Sources*, 180 (2008) 676-681.

[61] C.Z. Yuan, B. Gao, L.H. Su, L. Chen, X.G. Zhang, Electrochemically Induced Phase Transformation and Charge-Storage Mechanism of Amorphous CoS_x Nanoparticles Prepared by Interface-Hydrothermal Method, *J. Electrochem. Soc.*, 156 (2009) A199-A203.

[62] Z. Yang, C.-Y. Chen, H.-T. Chang, Supercapacitors Incorporating Hollow Cobalt Sulfide Hexagonal Nanosheets, *J. Power Sources*, 196 (2011) 7874-7877.

[63] H. Shi, Activated Carbons and Double Layer Capacitance, *Electrochim. Acta*, 41 (1996) 1633-1639.

[64] D.Y. Qu, H. Shi, Studies of Activated Carbons Used in Double-Layer Capacitors, *J. Power Sources*, 74 (1998) 99-107.

[65] J. Gamby, P.L. Taberna, P. Simon, J.F. Fauvarque, M. Chesneau, Studies and Characterisations of Various Activated Carbons Used for Carbon/Carbon Supercapacitors, *J. Power Sources*, 101 (2001) 109-116.

[66] K. Jurewicz, C. Vix-Guterl, E. Frackowiak, S. Saadallah, A. Reda, J. Parmentier, J. Patarin, F. Beguin, Capacitance Properties of Ordered Porous Carbon Materials Prepared by a Templating Procedure, *J. Phys. Chem. Solids*, 65 (2004) 287-293.

[67] J.A. Fernandez, T. Morishita, M. Toyoda, M. Inagaki, F. Stoeckli, T.A. Centeno, Performance of Mesoporous Carbons Derived from Poly(Vinyl Alcohol) in Electrochemical Capacitors, *J. Power Sources*, 175 (2008) 675-679.

[68] A.B. Fuertes, F. Pico, J.M. Rojo, Influence of Pore Structure on Electric Double-Layer Capacitance of Template Mesoporous Carbons, *J. Power Sources*, 133 (2004) 329-336.

[69] A.B. Fuertes, G. Lota, T.A. Centeno, E. Frackowiak, Templated Mesoporous Carbons for Supercapacitor Application, *Electrochim. Acta*, 50 (2005) 2799-2805.

[70] H.S. Zhou, S.M. Zhu, M. Hibino, I. Honma, Electrochemical Capacitance of Self-Ordered Mesoporous Carbon, *J. Power Sources*, 122 (2003) 219-223.

[71] K. Xia, Q. Gao, J. Jiang, J. Hu, Hierarchical Porous Carbons with Controlled Micropores and Mesopores for Supercapacitor Electrode Materials, *Carbon*, 46 (2008) 1718-1726.

[72] T.S.K. P., Electrochemical Supercapacitors as Versatile Energy Stores, *Platinum Metals Rev.*, 38 (1994) 46-56.

[73] V. Subramanian, H.W. Zhu, R. Vajtai, P.M. Ajayan, B.Q. Wei, Hydrothermal Synthesis and Pseudocapacitance Properties of MnO_2 Nanostructures, *J. Phys. Chem. B*, 109 (2005) 20207-20214.

[74] S.L. Xiong, C.Z. Yuan, M.F. Zhang, B.J. Xi, Y.T. Qian, Controllable Synthesis of Mesoporous Co_3O_4 Nanostructures with Tunable Morphology for Application in Supercapacitors, *Chem. Eur. J.*, 15 (2009) 5320-5326.

[75] C.Z. Yuan, X.G. Zhang, L.H. Su, B. Gao, L.F. Shen, Facile Synthesis and Self-Assembly of Hierarchical Porous NiO Nano/Micro Spherical Superstructures for High Performance Supercapacitors, *J. Mater. Chem.*, 19 (2009) 5772-5777.

[76] A. Rudge, J. Davey, I. Raistrick, S. Gottesfeld, J.P. Ferraris, Conducting Polymers as Active Materials in Electrochemical Capacitors, *J. Power Sources*, 47 (1994) 89-107.

[77] K. Naoi, S. Suematsu, A. Manago, Electrochemistry of Poly(1,5-Diaminoanthraquinone) and Its Application in Electrochemical Capacitor Materials, *J. Electrochem. Soc.*, 147 (2000) 420-426.

[78] A. Laforgue, P. Simon, J.F. Fauvarque, Chemical Synthesis and Characterization of Fluorinated Polyphenylthiophenes: Application to Energy Storage, *Synth. Met.*, 123 (2001) 311-319.

[79] F. Fusalba, P. Gouerec, D. Villers, D. Belanger, Electrochemical Characterization of Polyaniline in Nonaqueous Electrolyte and Its Evaluation as Electrode Material for Electrochemical Supercapacitors, *J. Electrochem. Soc.*, 148 (2001) A1-A6.

[80] L.Z. Fan, J. Maier, High-Performance Polypyrrole Electrode Materials for Redox Supercapacitors, *Electrochem. Commun.*, 8 (2006) 937-940.

[81] Y. Wang, Z. Shi, Y. Huang, Y. Ma, C. Wang, M. Chen, Y. Chen, Supercapacitor Devices Based on Graphene Materials, *J. Phys. Chem. C*, 113 (2009) 13103-13107.

[82] X. Du, P. Guo, H. Song, X. Chen, Graphene Nanosheets as Electrode Material for Electric Double-Layer Capacitors, *Electrochim. Acta*, 55 (2010) 4812-4819.

[83] C. Liu, Z. Yu, D. Neff, A. Zhamu, B.Z. Jang, Graphene-Based Supercapacitor with an Ultrahigh Energy Density, *Nano Lett.*, 10 (2010) 4863-4868.

[84] Y. Zhu, S. Murali, M.D. Stoller, K.J. Ganesh, W. Cai, P.J. Ferreira, A. Pirkle, R.M. Wallace, K.A. Cychosz, M. Thommes, D. Su, E.A. Stach, R.S. Ruoff, Carbon-Based Supercapacitors Produced by Activation of Graphene, *Science*, 332 (2011) 1537-1541.

[85] H.M. Jeong, J.W. Lee, W.H. Shin, Y.J. Choi, H.J. Shin, J.K. Kang, J.W. Choi, Nitrogen-Doped Graphene for High-Performance Ultracapacitors and the Importance of Nitrogen-Doped Sites at Basal Planes, *Nano Lett.*, 11 (2011) 2472-2477.

[86] H. Wang, H.S. Casalongue, Y. Liang, H. Dai, $Ni(OH)_2$ Nanoplates Grown on Graphene as Advanced Electrochemical Pseudocapacitor Materials, *J. Am. Chem. Soc.*, 132 (2010) 7472-7477.

[87] S. Chen, J. Zhu, X. Wang, One-Step Synthesis of Graphene–Cobalt Hydroxide Nanocomposites and Their Electrochemical Properties, *J. Phys. Chem. C*, 114 (2010) 11829-11834.

[88] Z.-S. Wu, D.-W. Wang, W. Ren, J. Zhao, G. Zhou, F. Li, H.-M. Cheng, Anchoring Hydrous RuO_2 on Graphene Sheets for High-Performance Electrochemical Capacitors, *Adv. Funct. Mater.*, 20 (2010) 3595-3602.

[89] F.H. Li, J.F. Song, H.F. Yang, S.Y. Gan, Q.X. Zhang, D.X. Han, A. Ivaska, L. Niu, One-Step Synthesis of Graphene/SnO_2 Nanocomposites and Its Application in Electrochemical Supercapacitors, *Nanotechnology*, 20 (2009) 455602.

[90] J. Yan, T. Wei, W. Qiao, B. Shao, Q. Zhao, L. Zhang, Z. Fan, Rapid Microwave-Assisted Synthesis of Graphene Nanosheet/Co_3O_4 Composite for Supercapacitors, *Electrochim. Acta*, 55 (2010) 6973-6978.

[91] S. Chen, J. Zhu, X. Wu, Q. Han, X. Wang, Graphene Oxide–MnO$_2$ Nanocomposites for Supercapacitors, *ACS Nano*, 4 (2010) 2822-2830.

[92] J. Yan, Z. Fan, T. Wei, W. Qian, M. Zhang, F. Wei, Fast and Reversible Surface Redox Reaction of Graphene-MnO_2 Composites as Supercapacitor Electrodes, *Carbon*, 48 (2010) 3825-3833.

[93] Y. Chen, X. Zhang, D. Zhang, P. Yu, Y. Ma, High Performance Supercapacitors Based on Reduced Graphene Oxide in Aqueous and Ionic Liquid Electrolytes, *Carbon*, 49 (2011) 573-580.

[94] Z. Fan, J. Yan, T. Wei, L. Zhi, G. Ning, T. Li, F. Wei, Asymmetric Supercapacitors Based on Graphene/MnO_2 and Activated Carbon Nanofiber Electrodes with High Power and Energy Density, *Adv. Funct. Mater.*, 21 (2011) 2366-2375.

[95] H. Huang, X. Wang, Graphene Nanoplate-MnO_2 Composites for Supercapacitors: A Controllable Oxidation Approach, *Nanoscale*, 3 (2011) 3185-3191.

[96] H. Lee, J. Kang, M.S. Cho, J.-B. Choi, Y. Lee, MnO_2/Graphene Composite Electrodes for Supercapacitors: The Effect of Graphene Intercalation on Capacitance, *J. Mater. Chem.*, 21 (2011) 18215-18219.

[97] G. Yu, L. Hu, N. Liu, H. Wang, M. Vosgueritchian, Y. Yang, Y. Cui, Z. Bao, Enhancing the Supercapacitor Performance of Graphene/MnO_2 Nanostructured Electrodes by Conductive Wrapping, *Nano Lett.*, 11 (2011) 4438-4442.

[98] J. Zhang, J. Jiang, X.S. Zhao, Synthesis and Capacitive Properties of Manganese Oxide Nanosheets Dispersed on Functionalized Graphene Sheets, *J. Phys. Chem. C*, 115 (2011) 6448-6454.

[99] P.G. Bruce, B. Scrosati, J.M. Tarascon, Nanomaterials for Rechargeable Lithium Batteries, *Angew. Chem. Int. Ed.*, 47 (2008) 2930-2946.

[100] P. Balaya, A.J. Bhattacharyya, J. Jamnik, Y.F. Zhukovskii, E.A. Kotomin, J. Maier, Nano-Ionics in the Context of Lithium Batteries, *J. Power Sources*, 159 (2006) 171-178.

[101] N. Meethong, H.-Y.S. Huang, W.C. Carter, Y.-M. Chiang, Size-Dependent Lithium Miscibility Gap in Nanoscale $Li_{1-x}FePO_4$, *Electrochem. Solid-State Lett.*, 10 (2007) A134-A138.

[102] B. W. van Schalkwijk, B. Scrosati (Ed.), Advances in Lithium-Ion Batteries, Kluwer Academic/Plenum, New York, 2002.

[103] G.-A. Nazri, G. Pistoia (Ed.), Lithium Batteries Science and Technology, Kluwer Academic/Plenum, Boston, 2004.

[104] E. Peled, The Electrochemical Behavior of Alkali and Alkaline Earth Metals in Nonaqueous Battery Systems – the Solid Electrolyte Interphase Model, *J. Electrochem. Soc.*, 126 (1979) 2047-2051.

[105] R. Fong, U. von Sacken, J.R. Dahn, Studies of Lithium Intercalation into Carbons Using Nonaqueous Electrochemical Cells, *J. Electrochem. Soc.*, 137 (1990) 2009-2013.

[106] R. Kanno, Y. Kawamoto, Y. Takeda, S. Ohashi, N. Imanishi, O. Yamamoto, Carbon Fiber as a Negative Electrode in Lithium Secondary Cells, *J. Electrochem. Soc.*, 139 (1992) 3397-3404.

[107] P. Poizot, S. Laruelle, S. Grugeon, L. Dupont, J.M. Tarascon, Nano-Sized Transition-Metal Oxides as Negative-Electrode Materials for Lithium-Ion Batteries, *Nature*, 407 (2000) 496-499.

[108] C.Q. Zhang, J.P. Tu, X.H. Huang, Y.F. Yuan, X.T. Chen, F. Mao, Preparation and Electrochemical Performances of Cubic Shape Cu_2O as Anode Material for Lithium Ion Batteries, *J. Alloys Compd.*, 441 (2007) 52-56.

[109] B. Varghese, M.V. Reddy, Z. Yanwu, C.S. Lit, T.C. Hoong, G.V. Subba Rao, B.V.R. Chowdari, A.T.S. Wee, C.T. Lim, C.-H. Sow, Fabrication of NiO Nanowall Electrodes for High Performance Lithium Ion Battery, *Chem. Mater.*, 20 (2008) 3360-3367.

[110] J. Chen, L. Xu, W. Li, X. Gou, α-Fe_2O_3 Nanotubes in Gas Sensor and Lithium-Ion Battery Applications, *Adv. Mater.*, 17 (2005) 582-586.

[111] P. Balaya, H. Li, L. Kienle, J. Maier, Fully Reversible Homogeneous and Heterogeneous Li Storage in RuO_2 with High Capacity, *Adv. Funct. Mater.*, 13 (2003) 621-625.

[112] V. Pralong, D.C.S. Souza, K.T. Leung, L.F. Nazar, Reversible Lithium Uptake by CoP_3 at Low Potential: Role of the Anion, *Electrochem. Commun.*, 4 (2002) 516-520.

[113] F. Badway, N. Pereira, F. Cosandey, G.G. Amatucci, Carbon-Metal Fluoride Nanocomposites, *J. Electrochem. Soc.*, 150 (2003) A1209-A1218.

[114] H. Li, G. Richter, J. Maier, Reversible Formation and Decomposition of LiF Clusters Using Transition Metal Fluorides as Precursors and Their Application in Rechargeable Li Batteries, *Adv. Mater.*, 15 (2003) 736-739.

[115] N. Pereira, L. Dupont, J.M. Tarascon, L.C. Klein, G.G. Amatucci, Electrochemistry of Cu_3N with Lithium, *J. Electrochem. Soc.*, 150 (2003) A1273-A1280.

[116] D.C.C. Silva, O. Crosnier, G. Ouvrard, J. Greedan, A. Safa-Sefat, L.F. Nazar, Reversible Lithium Uptake by FeP_2, *Electrochem. Solid-State Lett.*, 6 (2003) A162-A165.

[117] M. Bervas, F. Badway, L.C. Klein, G.G. Amatucci, Bismuth Fluoride Nanocomposite as a Positive Electrode Material for Rechargeable Lithium Batteries, *Electrochem. Solid-State Lett.*, 8 (2005) A179-A183.

[118] A.K. Padhi, K.S. Nanjundaswamy, C. Masquelier, S. Okada, J.B. Goodenough, Effect of Structure on the Fe^{3+}/Fe^{2+} Redox Couple in Iron Phosphates, *J. Electrochem. Soc.*, 144 (1997) 1609-1613.

[119] V. Srinivasan, J. Newman, Existence of Path-Dependence in the $LiFePO_4$ Electrode, *Electrochem. Solid-State Lett.*, 9 (2006) A110-A114.

[120] A. Yamada, S.C. Chung, K. Hinokuma, Optimized $LiFePO_4$ for Lithium Battery Cathodes, *J. Electrochem. Soc.*, 148 (2001) A224-A229.

[121] H. Huang, S.C. Yin, L.F. Nazar, Approaching Theoretical Capacity of $LiFePO_4$ at Room Temperature at High Rates, *Electrochem. Solid State Lett.*, 4 (2001) A170-A172.

[122] K. Sato, M. Noguchi, A. Demachi, N. Oki, M. Endo, A Mechanism of Lithium Storage in Disordered Carbons, *Science*, 264 (1994) 556-558.

[123] J.R. Dahn, T. Zheng, Y.H. Liu, J.S. Xue, Mechanisms for Lithium Insertion in Carbonaceous Materials, *Science*, 270 (1995) 590-593.

[124] T. Zheng, J.S. Xue, J.R. Dahn, Lithium Insertion in Hydrogen-Containing Carbonaceous Materials, *Chem. Mater.*, 8 (1996) 389-393.

[125] G. Wang, B. Wang, X. Wang, J. Park, S. Dou, H. Ahn, K. Kim, Sn/Graphene Nanocomposite with 3d Architecture for Enhanced Reversible Lithium Storage in Lithium Ion Batteries, *J. Mater. Chem.*, 19 (2009) 8378-8384.

[126] S.M. Paek, E. Yoo, I. Honma, Enhanced Cyclic Performance and Lithium Storage Capacity of SnO_2/Graphene Nanoporous Electrodes with Three-Dimensionally Delaminated Flexible Structure, *Nano Lett.*, 9 (2009) 72-75.

[127] J. Yao, X. Shen, B. Wang, H. Liu, G. Wang, In Situ Chemical Synthesis of SnO_2-Graphene Nanocomposite as Anode Materials for Lithium-Ion Batteries, *Electrochem. Commun.*, 11 (2009) 1849-1852.

[128] B. Li, H. Cao, J. Shao, M. Qu, J.H. Warner, Superparamagnetic Fe_3O_4 Nanocrystals@Graphene Composites for Energy Storage Devices, *J. Mater. Chem.*, 21 (2011) 5069-5075.

[129] C. Xu, X. Wang, L. Yang, Y. Wu, Fabrication of a Graphene–Cuprous Oxide Composite, *J. Solid State Chem.*, 182 (2009) 2486-2490.

[130] D. Wang, D. Choi, J. Li, Z. Yang, Z. Nie, R. Kou, D. Hu, C. Wang, L.V. Saraf, J. Zhang, I.A. Aksay, J. Liu, Self-Assembled TiO_2–Graphene Hybrid Nanostructures for Enhanced Li-Ion Insertion, *ACS Nano*, 3 (2009) 907-914.

[131] http://www.rothamsted.ac.uk/pbcs/bioimaging/Equipment_EMs_TEMs.php

[132] http://www.asylumresearch.com/

[133] http://www.micromeritics.com/product-showcase/TriStar-II-3020.aspx

[134] Y. Idota, T. Kubota, A. Matsufuji, Y. Maekawa, T. Miyasaka, Tin-Based Amorphous Oxide: A High-Capacity Lithium-Ion-Storage Material, *Science*, 276 (1997) 1395-1397.

[135] F. Tuinstra, J.L. Koenig, Raman Spectrum of Graphite, *J. Chem. Phys.*, 53 (1970) 1126-1130.

[136] A.C. Ferrari, J. Robertson, Interpretation of Raman Spectra of Disordered and Amorphous Carbon, *Phys.Rev. B*, 61 (2000) 14095-14107.

[137] N.I. Kovtyukhova, P.J. Ollivier, B.R. Martin, T.E. Mallouk, S.A. Chizhik, E.V. Buzaneva, A.D. Gorchinskiy, Layer-by-Layer Assembly of Ultrathin Composite Films from Micron-Sized Graphite Oxide Sheets and Polycations, *Chem. Mater.*, 11 (1999) 771-778.

[138] S. Park, K.S. Lee, G. Bozoklu, W. Cai, S.T. Nguyen, R.S. Ruoff, Graphene Oxide Papers Modified by Divalent Ions – Enhancing Mechanical Properties Via Chemical Cross-Linking, *ACS Nano*, 2 (2008) 572-578.

[139] G. Williams, B. Seger, P.V. Kamat, TiO_2-Graphene Nanocomposites. UV-Assisted Photocatalytic Reduction of Graphene Oxide, *ACS Nano*, 2 (2008) 1487-1491.

[140] I.A. Courtney, J.R. Dahn, Electrochemical and in Situ X-Ray Diffraction Studies of the Reaction of Lithium with Tin Oxide Composites, *J. Electrochem. Soc.*, 144 (1997) 2045-2052.

[141] R. Demir-Cakan, Y.S. Hu, M. Antonietti, J. Maier, M.M. Titirici, Facile One-Pot Synthesis of Mesoporous SnO_2 Microspheres Via Nanoparticles Assembly and Lithium Storage Properties, *Chem. Mater.*, 20 (2008) 1227-1229.

[142] J. Hassoun, G. Derrien, S. Panero, B. Scrosati, A Nanostructured Sn-C Composite Lithium Battery Electrode with Unique Stability and High Electrochemical Performance, *Adv. Mater.*, 20 (2008) 3169-3175.

[143] W.-M. Zhang, J.-S. Hu, Y.-G. Guo, S.-F. Zheng, L.-S. Zhong, W.-G. Song, L.-J. Wan, Tin-Nanoparticles Encapsulated in Elastic Hollow Carbon Spheres for High-Performance Anode Material in Lithium-Ion Batteries, *Adv. Mater.*, 20 (2008) 1160-1165.

[144] T. Yamashita, A. Vannice, N_2O Decomposition over Manganese Oxides, *J. Catal.*, 161 (1996) 254-262.

[145] M. Johns, P. Landon, T. Alderson, G.J. Hutchings, Decreased Methane Formation from the Hydrogenation of Carbon Monoxide Using Zeolite/Cobalt-Manganese Oxide Composite Catalysts, *Chem. Commun.*, (2001) 2454-2455.

[146] H. Einaga, S. Futamura, Catalytic Oxidation of Benzene with Ozone over Alumina-Supported Manganese Oxides, *J. Catal.*, 227 (2004) 304-312.

[147] N. Sakai, Y. Ebina, K. Takada, T. Sasaki, Electrochromic Films Composed of MnO_2 Nanosheets with Controlled Optical Density and High Coloration Efficiency, *J. Electrochem. Soc.*, 152 (2005) E384-E389.

[148] C.-C. Hu, Y.-T. Wu, K.-H. Chang, Low-Temperature Hydrothermal Synthesis of Mn_3O_4 and MnOOH Single Crystals: Determinant Influence of Oxidants, *Chem. Mater.*, 20 (2008) 2890-2894.

[149] S. Jana, S. Pande, A.K. Sinha, T. Pal, Synthesis of Superparamagnetic β-MnO_2 Organosol: A Photocatalyst for the Oxidative Phenol Coupling Reaction, *Inorg. Chem.*, 47 (2008) 5558-5560.

[150] D. Hulicova-Jurcakova, M. Kodama, S. Shiraishi, H. Hatori, Z.H. Zhu, G.Q. Lu, Nitrogen-Enriched Nonporous Carbon Electrodes with Extraordinary Supercapacitance, *Adv. Funct. Mater.*, 19 (2009) 1800-1809.

[151] F. Beguin, K. Szostak, G. Lota, E. Frackowiak, A Self-Supporting Electrode for Supercapacitors Prepared by One-Step Pyrolysis of Carbon Nanotube/Polyacrylonitrile Blends, *Adv. Mater.*, 17 (2005) 2380-2384.

[152] E. Raymundo-Pinero, F. Leroux, F. Beguin, A High-Performance Carbon for Supercapacitors Obtained by Carbonization of a Seaweed Biopolymer, *Adv. Mater.*, 18 (2006) 1877-1882.

[153] D. Hulicova, J. Yamashita, Y. Soneda, H. Hatori, M. Kodama, Supercapacitors Prepared from Melamine-Based Carbon, *Chem. Mater.*, 17 (2005) 1241-1247.

[154] D. Hulicova, M. Kodama, H. Hatori, Electrochemical Performance of Nitrogen-Enriched Carbons in Aqueous and Non-Aqueous Supercapacitors, *Chem. Mater.*, 18 (2006) 2318-2326.

[155] X.W. Lou, D. Deng, J.Y. Lee, J. Feng, L.A. Archer, Self-Supported Formatnion of Needlelike Co_3O_4 Nanotubes and Their Application as Lithium-Ion Battery Electrodes, *Adv. Mater.*, 20 (2008) 258-262.

[156] S. Xiong, C. Yuan, M. Zhang, B. Xi, Y. Qian, Controllable Synthesis of Mesoporous Co_3O_4 Nanostructures with Tunable Morphology for Application in Supercapacitors, *Chem. Eur. J.*, 15 (2009) 5320-5326.

[157] J. Ma, S. Zhang, W. Liu, Y. Zhao, Facile Preparation of Co_3O_4 Nanocrystals Via a Solvothermal Process Directly from Common Co_2O_3 Powder, *J. Alloys Compd.*, 490 (2010) 647-651.

[158] G. Wang, X. Shen, J. Horvat, B. Wang, H. Liu, D. Wexler, J. Yao, Hydrothermal Synthesis and Optical, Magnetic, and Supercapacitance Properties of Nanoporous Cobalt Oxide Nanorods, *J. Phys. Chem. C*, 113 (2009) 4357-4361.

[159] L. Yang, W. Guan, B. Bai, Q. Xu, Y. Xiang, Synthesis of Yeast-Assisted Co_3O_4 Hollow Microspheres – a Novel Biotemplating Technique, *J. Alloys Compd.*, 504 (2010) L10-L13.

[160] G. Wang, X. Shen, J. Yao, D. Wexler, J.-H. Ahn, Hydrothermal Synthesis of Carbon Nanotube/Cobalt Oxide Core-Shell One-Dimensional Nanocomposite and Application as an Anode Material for Lithium-Ion Batteries, *Electrochem. Commun.*, 11 (2009) 546-549.

[161] Y. Shan, L. Gao, Formation and Characterization of Multi-Walled Carbon Nanotubes/Co_3O_4 Nanocomposites for Supercapacitors, *Mater. Chem. Phys.*, 103 (2007) 206-210.

[162] Z.-S. Wu, W. Ren, L. Wen, L. Gao, J. Zhao, Z. Chen, G. Zhou, F. Li, H.-M. Cheng, Graphene Anchored with Co_3O_4 Nanoparticles as Anode of Lithium Ion Batteries with Enhanced Reversible Capacity and Cyclic Performance, *ACS Nano*, 4 (2010) 3187-3194.

[163] D. Li, M.B. Mueller, S. Gilje, R.B. Kaner, G.G. Wallace, Processable Aqueous Dispersions of Graphene Nanosheets, *Nature Nanotech.*, 3 (2008) 101-105.

[164] V.G. Hadjiev, M.N. Iliev, I.V. Vergilov, The Raman Spectra of Co_3O_4, *J. Phys. C: Solid State Phys.*, 21 (1988) L199-L201.

[165] Z.-S. Wu, W. Ren, L. Gao, B. Liu, C. Jiang, H.-M. Cheng, Synthesis of High-Quality Graphene with a Pre-Determined Number of Layers, *Carbon*, 47 (2009) 493-499.

[166] C. Jiang, E. Hosono, H. Zhou, Nanomaterials for Lithium Ion Batteries, *Nano Today*, 1 (2006) 28-33.

[167] B. Wang, J. Park, C. Wang, H. Ahn, G. Wang, Mn_3O_4 Nanoparticles Embedded into Graphene Nanosheets: Preparation, Characterization, and Electrochemical Properties for Supercapacitors, *Electrochim. Acta*, 55 (2010) 6812-6817.

[168] F. Pico, J. Ibanez, M.A. Lillo-Rodenas, A. Linares-Solano, R.M. Rojas, J.M. Amarilla, J.M. Rojo, Understanding $RuO_2 \cdot xH_2O$/Carbon Nanofibre Composites as Supercapacitor Electrodes, *J. Power Sources*, 176 (2008) 417-425.

[169] E. Frackowiak, G. Lota, J. Machnikowski, C. Vix-Guterl, F. Beguin, Optimisation of Supercapacitors Using Carbons with Controlled Nanotexture and Nitrogen Content, *Electrochim. Acta*, 51 (2006) 2209-2214.

[170] R.D. Rauh, K.M. Abraham, G.F. Pearson, J.K. Surprenant, S.B. Brummer, Lithium-Dissolved Sulfur Battery with an Organic Electrolyte, *J. Electrochem. Soc.*, 126 (1979) 523-527.

[171] S.E. Cheon, K.S. Ko, J.H. Cho, S.W. Kim, E.Y. Chin, H.T. Kim, Rechargeable Lithium Sulfur Battery – I. Structural Change of Sulfur Cathode During Discharge and Charge, *J. Electrochem. Soc.*, 150 (2003) A796-A799.

[172] J.R. Akridge, Y.V. Mikhaylik, N. White, Li/S Fundamental Chemistry and Application to High-Performance Rechargeable Batteries, *Solid State Ionics*, 175 (2004) 243-245.

[173] J.L. Wang, J. Yang, J.Y. Xie, N.X. Xu, Y. Li, Sulfur-Carbon Nano-Composite as Cathode for Rechargeable Lithium Battery Based on Gel Electrolyte, *Electrochem. Commun.*, 4 (2002) 499-502.

[174] W. Zheng, Y.W. Liu, X.G. Hu, C.F. Zhang, Novel Nanosized Adsorbing Sulfur Composite Cathode Materials for the Advanced Secondary Lithium Batteries, *Electrochim. Acta*, 51 (2006) 1330-1335.

[175] J. Wang, S.Y. Chew, Z.W. Zhao, S. Ashraf, D. Wexler, J. Chen, S.H. Ng, S.L. Chou, H.K. Liu, Sulfur-Mesoporous Carbon Composites in Conjunction with a Novel Ionic Liquid Electrolyte for Lithium Rechargeable Batteries, *Carbon*, 46 (2008) 229-235.

[176] C. Lai, X.P. Gao, B. Zhang, T.Y. Yan, Z. Zhou, Synthesis and Electrochemical Performance of Sulfur/Highly Porous Carbon Composites, *J. Phys. Chem. C*, 113 (2009) 4712-4716.

[177] J. Wang, J. Yang, J. Xie, N. Xu, A Novel Conductive Polymer-Sulfur Composite Cathode Material for Rechargeable Lithium Batteries, *Adv. Mater.*, 14 (2002) 963-965.

[178] J. Wang, L. Liu, Z. Ling, J. Yang, C. Wan, C. Jiang, Polymer Lithium Cells with Sulfur Composites as Cathode Materials, *Electrochim. Acta*, 48 (2003) 1861-1867.

[179] J. Wang, J. Yang, C. Wan, K. Du, J. Xie, N. Xu, Sulfur Composite Cathode Materials for Rechargeable Lithium Batteries, *Adv. Funct. Mater.*, 13 (2003) 487-492.

[180] X. He, W. Pu, J. Ren, L. Wang, J. Wang, C. Jiang, C. Wan, Charge/Discharge Characteristics of Sulfur Composite Cathode Materials in Rechargeable Lithium Batteries, *Electrochim. Acta*, 52 (2007) 7372-7376.

[181] B.M.L. Rao, J.A. Shropshire, Effect of Sulfur Impurities on Li/TiS_2 Cells, *J. Electrochem. Soc.*, 128 (1981) 942-945.

[182] X. Ji, L.F. Nazar, Advances in Li-S Batteries, *J. Mater. Chem.*, 20 (2010) 9821-9826.

[183] B. Jin, J.-U. Kim, H.-B. Gu, Electrochemical Properties of Lithium-Sulfur Batteries, *J. Power Sources*, 117 (2003) 148-152.

[184] L.X. Yuan, J.K. Feng, X.P. Ai, Y.L. Cao, S.L. Chen, H.X. Yang, Improved Dischargeability and Reversibility of Sulfur Cathode in a Novel Ionic Liquid Electrolyte, *Electrochem. Commun.*, 8 (2006) 610-614.

[185] D. Marmorstein, T.H. Yu, K.A. Striebel, F.R. McLarnon, J. Hou, E.J. Cairns, Electrochemical Performance of Lithium/Sulfur Cells with Three Different Polymer Electrolytes, *J. Power Sources*, 89 (2000) 219-226.

[186] B.H. Jeon, J.H. Yeon, K.M. Kim, I.J. Chung, Preparation and Electrochemical Properties of Lithium-Sulfur Polymer Batteries, *J. Power Sources*, 109 (2002) 89-97.

[187] J.-W. Choi, J.-K. Kim, G. Cheruvally, J.-H. Ahn, H.-J. Ahn, K.-W. Kim, Rechargeable Lithium/Sulfur Battery with Suitable Mixed Liquid Electrolytes, *Electrochim. Acta*, 52 (2007) 2075-2082.

[188] A. Hayashi, T. Ohtomo, F. Mizuno, K. Tadanaga, M. Tatsumisago, All-Solid-State Li/S Batteries with Highly Conductive Glass–Ceramic Electrolytes, *Electrochem. Commun.*, 5 (2003) 701-705.

[189] X. Zhu, Z. Wen, Z. Gu, Z. Lin, Electrochemical Characterization and Performance Improvement of Lithium/Sulfur Polymer Batteries, *J. Power Sources*, 139 (2005) 269-273.

[190] S.S. Jeong, Y.T. Lim, Y.J. Choi, G.B. Cho, K.W. Kim, H.J. Ahn, K.K. Cho, Electrochemical Properties of Lithium Sulfur Cells Using PEO Polymer Electrolytes Prepared under Three Different Mixing Conditions, *J. Power Sources*, 174 (2007) 745-750.

[191] J. Hassoun, B. Scrosati, Moving to a Solid-State Configuration: A Valid Approach to Making Lithium-Sulfur Batteries Viable for Practical Applications, *Adv. Mater.*, 22 (2010) 5198-5201.

[192] X. Ji, K.T. Lee, L.F. Nazar, A Highly Ordered Nanostructured Carbon-Sulphur Cathode for Lithium-Sulphur Batteries, *Nat. Mater.*, 8 (2009) 500-506.

[193] H. Wang, Y. Yang, Y. Liang, J.T. Robinson, Y. Li, A. Jackson, Y. Cui, H. Dai, Graphene-Wrapped Sulfur Particles as a Rechargeable Lithium-Sulfur Battery Cathode Material with High Capacity and Cycling Stability, *Nano Lett.*, 11 (2011) 2644-2647.

[194] X. Ji, S. Evers, R. Black, L.F. Nazar, Stabilizing Lithium-Sulphur Cathodes Using Polysulphide Reservoirs, *Nat. Commun.*, 2 (2011) 325.

[195] N. Jayaprakash, J. Shen, S.S. Moganty, A. Corona, L.A. Archer, Porous Hollow Carbon@Sulfur Composites for High-Power Lithium–Sulfur Batteries, *Angew. Chem. Int. Ed.*, 50 (2011) 5904-5908.

[196] J. Hassoun, J. Kim, D.-J. Lee, H.-G. Jung, S.-M. Lee, Y.-K. Sun, B. Scrosati, A Contribution to the Progress of High Energy Batteries: A Metal-Free, Lithium-Ion, Silicon-Sulfur Battery, *J. Power Sources*, 202 (2012) 308-313.

[197] D.R. Chang, S.H. Lee, S.W. Kim, H.T. Kim, Binary Electrolyte Based on Tetra(Ethylene Glycol) Dimethyl Ether and 1,3-Dioxolane for Lithium-Sulfur Battery, *J. Power Sources*, 112 (2002) 452-460.

[198] A.T. Ward, Raman Spectroscopy of Sulfur, Sulfur-Selenium, and Sulfur-Arsenic Mixtures, *J. Phys. Chem.*, 72 (1968) 4133-4139.

[199] M.J. Allen, V.C. Tung, R.B. Kaner, Honeycomb Carbon: A Review of Graphene, *Chem. Rev.*, 110 (2009) 132-145.

[200] J. Giraudet, M. Dubois, J. Inacio, A. Hamwi, Electrochemical Insertion of Lithium Ions into Disordered Carbons Derived from Reduced Graphite Fluoride, *Carbon*, 41 (2003) 453-463.

[201] P. Guo, H. Song, X. Chen, Electrochemical Performance of Graphene Nanosheets as Anode Material for Lithium-Ion Batteries, *Electrochem. Commun.*, 11 (2009) 1320-1324.

[202] K.E. Aifantis, S.A. Hackney, Mechanical Stability for Nanostructured Sn- and Si-Based Anodes, *J. Power Sources*, 196 (2011) 2122-2127.

[203] K.E. Aifantis, T. Huang, S.A. Hackney, T. Sarakonsri, A. Yu, Capacity Fade in Sn-C Nanopowder Anodes Due to Fracture, *J. Power Sources*, 197 (2012) 246-252.

[204] S.E. Cheon, S.S. Choi, J.S. Han, Y.S. Choi, B.H. Jung, H.S. Lim, Capacity Fading Mechanisms on Cycling a High-Capacity Secondary Sulfur Cathode, *J. Electrochem. Soc.*, 151 (2004) A2067-A2073.

[205] M.-S. Park, G.-X. Wang, Y.-M. Kang, D. Wexler, S.-X. Dou, H.-K. Liu, Preparation and Electrochemical Properties of SnO_2 Nanowires for Application in Lithium-Ion Batteries, *Angew. Chem. Int. Ed.*, 46 (2007) 750-753.

[206] Y. Wang, J.Y. Lee, H.C. Zeng, Polycrystalline SnO_2 Nanotubes Prepared Via Infiltration Casting of Nanocrystallites and Their Electrochemical Application, *Chem. Mater.*, 17 (2005) 3899-3903.

[207] F. Wang, G. Yao, M. Xu, M. Zhao, Z. Sun, X. Song, Large-Scale Synthesis of Macroporous SnO_2 with/without Carbon and Their Application as Anode Materials for Lithium-Ion Batteries, *J. Alloys Compd.*, 509 (2011) 5969-5973.

[208] Y. Li, X. Lv, J. Lu, J. Li, Preparation of SnO_2-Nanocrystal/Graphene-Nanosheets Composites and Their Lithium Storage Ability, *J. Phys. Chem. C*, 114 (2010) 21770-21774.

[209] S.-M. Paek, E. Yoo, I. Honma, Enhanced Cyclic Performance and Lithium Storage Capacity of SnO_2/Graphene Nanoporous Electrodes with Three-Dimensionally Delaminated Flexible Structure, *Nano Lett.*, 9 (2008) 72-75.

[210] P. Lian, X. Zhu, S. Liang, Z. Li, W. Yang, H. Wang, High Reversible Capacity of SnO_2/Graphene Nanocomposite as an Anode Material for Lithium-Ion Batteries, *Electrochim. Acta*, 56 (2011) 4532-4539.

[211] S. Ding, D. Luan, F.Y.C. Boey, J.S. Chen, X.W. Lou, SnO_2 Nanosheets Grown on Graphene Sheets with Enhanced Lithium Storage Properties, *Chem. Commun.*, 47 (2011) 7155-7157.

[212] X. Huang, X. Zhou, L. Zhou, K. Qian, Y. Wang, Z. Liu, C. Yu, A Facile One-Step Solvothermal Synthesis of SnO_2/Graphene Nanocomposite and Its Application as an Anode Material for Lithium-Ion Batteries, *Chem. Phys. Chem.*, 12 (2011) 278-281.

[213] S.H. Sun, G.W. Meng, G.X. Zhang, T. Gao, B.Y. Geng, L.D. Zhang, J. Zuo, Raman Scattering Study of Rutile SnO_2 Nanobelts Synthesized by Thermal Evaporation of Sn Powders, *Chem. Phys. Lett.*, 376 (2003) 103-107.

[214] R. Demir-Cakan, Y.-S. Hu, M. Antonietti, J. Maier, M.-M. Titirici, Facile One-Pot Synthesis of Mesoporous SnO_2 Microspheres Via Nanoparticles Assembly and Lithium Storage Properties, *Chem. Mater.*, 20 (2008) 1227-1229.

[215] M. Jayalakshmi, M. Mohan Rao, B.M. Choudary, Identifying Nano SnS as a New Electrode Material for Electrochemical Capacitors in Aqueous Solutions, *Electrochem. Commun.*, 6 (2004) 1119-1122.

[216] K. Chang, W. Chen, *L*-Cysteine-Assisted Synthesis of Layered MoS_2/Graphene Composites with Excellent Electrochemical Performances for Lithium Ion Batteries, *ACS Nano*, 5 (2011) 4720-4728.

[217] K. Chang, W. Chen, In Situ Synthesis of MoS_2/Graphene Nanosheet Composites with Extraordinarily High Electrochemical Performance for Lithium Ion Batteries, *Chem. Commun.*, 47 (2011) 4252-4254.

[218] K. Chang, W. Chen, Single-Layer MoS_2/Graphene Dispersed in Amorphous Carbon: Towards High Electrochemical Performances in Rechargeable Lithium Ion Batteries, *J. Mater. Chem.*, 21 (2011) 17175-17184.

[219] C. Yuan, L. Hou, L. Yang, C. Fan, D. Li, J. Li, L. Shen, F. Zhang, X. Zhang, Interface-Hydrothermal Synthesis of Sn_3S_4/Graphene Sheet Composites and Their Application in Electrochemical Capacitors, *Mater. Lett.*, 65 (2011) 374-377.

[220] C.-T. Hsieh, W.-Y. Chen, Y.-S. Cheng, Influence of Oxidation Level on Capacitance of Electrochemical Capacitors Fabricated with Carbon Nanotube/Carbon Paper Composites, *Electrochim. Acta*, 55 (2010) 5294-5300.

[221] C.-T. Hsieh, S.-M. Hsu, J.-Y. Lin, H. Teng, Electrochemical Capacitors Based on Graphene Oxide Sheets Using Different Aqueous Electrolytes, *J. Phys. Chem. C*, 115 (2011) 12367-12374.